The Dissertation Committee for Jamie Ryan Gardner certifies that this is the approved version of the following dissertation:

Neutral atom imaging using a pulsed electromagnetic lens

Committee:

Mark Raizen, Supervisor

John Keto

Alex Demkov

Greg Sitz

S.V. Sreenivasan

Neutral atom imaging using a pulsed electromagnetic lens

by

Jamie Ryan Gardner, BS, MS

Dissertation

Presented to the Faculty of the Graduate School of
The University of Texas at Austin
in Partial Fulfillment
of the Requirements
for the degree of
Doctor of Philosophy

The University of Texas at Austin
December, 2016

To Robin, who taught me empathy and discipline;
to my parents, who taught me integrity and who made my world a safe place;
and to Olive the dog, who did the opposite.

Acknowledgements

I must first thank Mark Raizen, whose steady leadership and generous support guided this project through many obstacles. Several problems we encountered, like those with the supersonic valve, seemed preternaturally resistant to logical analysis. Others felt like fundamental flaws in the experimental design. At some points over the past five years, I am reasonably sure that Mark was the only person in the world who believed that our lens would produce images even a fraction as good as those which fill these pages. He has an uncanny ability to see to the core of a problem, and there were many humbling occasions on which this talent quickly outweighed several days' worth of dedicated troubleshooting. More important than offering fast solutions, Mark is always ready to sit down and think through a problem. When the path forward seems irredeemably blocked, meeting with Mark reliably helps to clarify the issue, outline a plan of attack, and lift our spirits. In addition to his scientific leadership, Mark's kindness and compassion set him apart. I have never felt pressured to prioritize this project over my personal well-being, and Mark has demonstrated countless times that his primary goal is not publications or grants but the success of his students.

Erik Anciaux joined the project at the end of my second year, and it would be difficult to overstate my debt to him as both a colleague and a friend. Through long periods of slow, discouraging progress, Erik's work ethic remained relentlessly focused. His attitude was buoyant enough to float my own, even when we were both convinced that the entire project was falling apart. Erik has a remarkable capacity to say: "nothing works, and we are very likely moving in the wrong direction; let's get to it." This ability to put one foot in front of the other—even when everything is broken—is something I admire and continuously try to emulate. Lest it be supposed that Erik's work ethic balances an unremarkable natural talent, I should also mention that he is an extremely gifted physicist. Erik's mastery of theoretical concepts and his knack for the minutiae of experimental atom optics make him uniquely qualified to tackle the many puzzles we face. He is personally responsible for breakthroughs like developing the Vespel-Swagelok connection and discovering the source of the double-peak phenomenon, among others. It is not the least bit hyperbolic to say that without Erik this project would not have succeeded. In addition to his scientific

contributions, I am indebted to Erik for his friendship, which made the lab a fun place to work. Our prototype lens was assembled in the chaos of high-volume political debates, often shouted over both the hum of the chopper (D-sharp, I believe) and a classic rock Pandora station (only on Fridays). It is a testament to our friendship that working together in an often-stressful environment never undermined our respect for one another.

Rodrigo Castillo-Garza was the life-force of this endeavor for its first several years. He nurtured it from a cocktail-napkin scheme all the way through to the first demonstrations of hexapole focusing and beyond. We joined the lab in the same semester, he as a post-doc and I as a graduate student. The plan at that time was to lithographically fabricate microlenses in a magnetized crystalline sample. We completed several clean-room training sessions before the problems with this design became too glaring to ignore. It was Rodrigo who tirelessly combed the literature for better ideas, who simulated dozens—if not hundreds—of wire geometries in COMSOL, and who finally laid out what seemed at the time like an impossibly long-term plan for building the world's best neutral atom lens. Rodrigo's vision and dedication embody one of the best examples I have seen of leadership-by-example. Like Mark, he also consistently treated students under his direction with kindness and respect. I can recall many cups of coffee over which he offered sympathy, encouragement, and understanding when they were badly needed.

It would be hard to do justice to all of the wonderful Raizen Lab members with whom I shared friendship, fruitful discussions, Crown and Anchor "meetings," lab lunches, and trips to the Salt Lick. On the focusing project, we have benefited from the contributions of Sagi Zisman and Aaron Swander as graduate students, Tharon Morrison and Whitney Seifert as undergraduates, and Beck Goodloe as a high school student. Yi Xu has recently joined us and shows great promise. Adam Libson was the senior Raizen Lab member when I arrived, and he was an endless source of information—both physics-related and otherwise. His work with the valve and the supersonic slower made him an expert in almost every aspect of our nascent project. Kirsten Viering was also full of wisdom, particularly as regarded setting up our laser system. David Medellin is one of those people whose appetite for digging into the details of a problem seems almost insatiable. I can remember many occasions on which he happily set aside his own work to participate in a discussion about ours. Bruce Klappauf was working on the isotope separation project during the

early years of our project, but like David he spent many hours gathered with us at a whiteboard, discussing the finer points of magnetic focusing. Simon Kheifets, Jianyong Mo, and Akarsh Simha did inspiring work on the Brownian motion project. Simon was a good friend in the lab, on the rugby pitch, and downtown; Jianyong and Akarsh were two more people with apparently-inexhaustible patience for mulling over other people's physics dilemmas. Tom Mazur was working with Bruce on the isotope separation project, and therefore had many useful insights to offer us. Tom is a talented scientist and a friendly, thoughtful guy with whom to share an office. When Tom left, it was my good fortune that Georgios Stratis—another capable physicist and philosophically-minded thinker—took his desk, which was next to mine. This is not common knowledge, but Georgios and I will one day be remembered not as physicists but as the authors of a daring tract applying the tools of physical mathematics to macroeconomics. Igal Bucay joined the lab in the same semester as Georgios, and has been a similarly excellent office mate. Kevin Melin is now the senior member on the slower experiment, having joined the project as an undergraduate around the time I arrived in Austin. Kevin, with wizard-like skill, showed us how to modify our IGBT driver box in order to mitigate the noisy self-triggering problems that were plaguing our lens. Just as impressively, he always has a book recommendation. The rest of the magnetic slower crew over the years has included Isaac Chavez (of Salt Lick challenge fame), Alina Blinova (who hosted many memorable gatherings at her house), Karl Burkhardt (who navigated a master's degree in physics despite a chemistry background), David Riegler, Lukas Gradl, and Yu Lu (whose recent qualifier inspired the recurring discussion of phase space density in this document). They are doing excellent work, and it will be exciting to hear about their upcoming results. Several people who recently joined the lab are clearly excellent recruits. These include post-docs Pavel Nagornykh, Harry Ha, and Ahmed Helal, as well as graduate students Jordan Zesch, Alex Leviyev, Melina Armer, and Logan Hilberry. Many undergraduates have also made excellent contributions in the lab over the years, including Daniel Ellsworth (with whom it has often been a privilege to drink whiskey, shoot guns, and ride motorcycles; though not at the same time), Daniel Raimi-Zlatic (whose victory rate in our chess matches I was extremely proud to reduce; to 99.5%.), David Dunsky, Will Yager, Camilo Perez, Jimmy Kennington, Willie Watson, Alec Eickbusch, and Will Plusnick.

Many other people have been crucial both to my own success and to the progress

of our research. Olga Vera has a profound understanding of the myriad administrative channels associated with shipping, purchasing, and lab management; she imparts this wisdom with patience and good humor. Jack Clifford in the student shop—in addition to his ability to machine almost anything and to teach people like me not to mill our fingers off—is always ready with a kind word and a sincere smile. Allan Schroeder and his team in the main shop built many important components in our beamline, including the hulking chopper chamber and the intricate brass aperture slide. Their work has never been anything but excellent. Ed Narevicius and Uzi Even, along with Ed's students, helped me get the Even-Lavie valve working when I traveled with it to Israel. We never figured out exactly what fixed it, but I suspect that the mere presence of its creator had a salubrious effect. Rob Clark was a post-doc in the lab when I visited UT in March of 2011. It was following our brief conversation that I spoke with Mark and, later, chose to join the Raizen group. Though Rob was gone by the time I returned, he set this whole episode in motion; for that, I am grateful.

Finally, I thank my family for their unconditional love and support. I could write this entire document in crayon, and—though I might not graduate—they would still be proud of me. If I have worked harder and more sincerely over the past few months than ever before, it is in an effort to create something worthy of their esteem.

Neutral atom imaging using a pulsed electromagnetic lens

Publication No. _____

Jamie Ryan Gardner, Ph.D.
The University of Texas at Austin, 2016

Supervisor: Mark G. Raizen

This dissertation describes the design, construction, and characterization of a new type of aberration-corrected, neutral-atom lens. Atom beam control plays a crucial role in many different fields, ranging from fundamental physics research and materials science to applied nanotechnology. Despite this, atom-optical elements like lenses and mirrors remain relatively underdeveloped compared to their counterparts in other optics fields. Though aberration correction is addressed quite comprehensively in photon and electron lenses, no credible research efforts have yet produced the same technology for neutral atoms.

We report on progress towards a neutral atom imaging device that will be useful in a range of applications, including nanofabrication and surface microscopy. Our novel technique for improving refractive power and correcting chromatic aberration in atom lenses is based on a fundamental paradigm shift from continuous, two-dimensional focusing to a pulsed, three-dimensional approach. Simulations of this system suggest that it will pave the way towards the long-sought goal of true atom imaging on the nanoscale. We construct a prototype lens and show that all of the technological requirements for the proposed system are easily satisfied. Using metastable neon from a supersonic source, we characterize this prototype for three different focal lengths and a diverse range of apertures. Despite some manufacturing imperfections, we observe lower distortion and higher resolution than has been shown in any previous hexapole lens. Comparison with simulations corroborates the underlying theory and encourages further refinement of the process.

Contents

List of Figures

Chapter One: Introduction

Neutral particle beams have featured prominently in physics research since the work of Stern and colleagues in the 1920s and of Rabi in the 1930s [1, 2]. Nearly a century later, they are still the basis for studies of quantum chemistry, Bose-Einstein condensation, and even particle physics [3, 4, 5]. Particle beams—including metastable atoms—are also useful in microscopy, where their short wavelength can confer an advantage over photon-based methods [6, 7, 8]. Finally, atomic and molecular sources are the starting point for many more applied processes, including atom lithography and direct deposition assembly [8, 9, 10, 11, 12, 13, 14]. Each of these broad goals—fundamental physics research, tool development, and fabrication—has much to gain from improvements in the techniques we use to control neutral atoms. One system of particular interest is the atom lens, which serves to collimate, focus, or otherwise manage the behavior of a propagating beam. The effectiveness of an atom lens—especially in the context of metastable microscopy or atomic nanofabrication—depends in large part on its capacity to produce high-resolution images and spots. Accordingly, improving lens resolution has been a long-standing goal in atom optics. Despite many clever techniques, efforts to reach the nanoscale have met with such stubborn obstacles that nanofabrication by atom imaging is currently regarded in some circles as a lost cause. Taking advantage of state-of-the-art high-speed electronics, we have developed a novel approach to this problem that simultaneously addresses both chromatic and spherical aberrations at minimal expense to flux. We have constructed and characterized a proof-of-principle apparatus to test our theory. Despite the flaws one might expect in a first-generation prototype, this lens has already outperformed all previous hexapole imaging devices. These results emphatically validate our model and illuminate the path to nanoscale imaging.

1.1 Atom lens basics

The analogy between particle beams and light was clear as early as 1911, when Dunoyer observed the ray-straight trajectories of sodium atoms in vacuum [16]. Stern and colleagues in the 1920s soon extended this connection to include analogs of reflec-

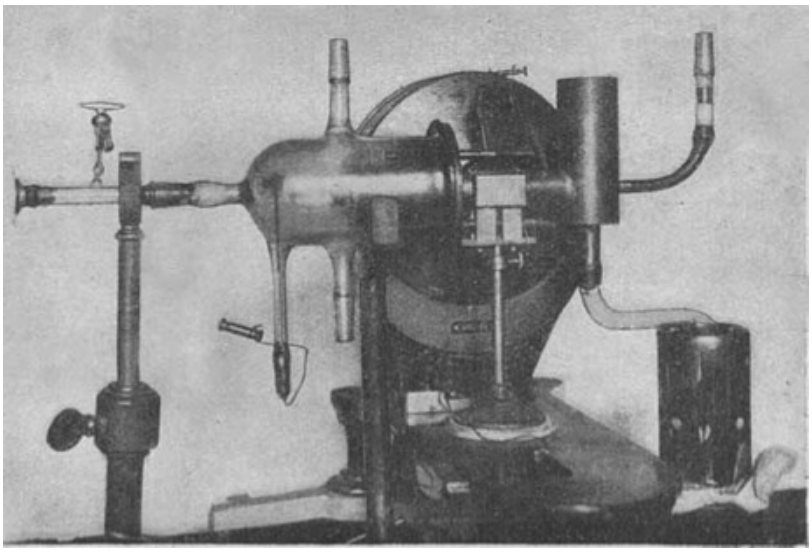

Figure 1.1: A photograph of the vacuum chamber used by Stern and Gerlach to conduct their famous experiments [1, 15].

tion, refraction, and diffraction (Figure 1.1) [1, 17, 18]. Beam focusing dates back at least to the work of Friedburg and Paul, who proposed not only a mirror-like magnetic element, but also a macro-scale electromagnetic hexapole lens [19, 20]. Since these first experiments, a wide range of beam control methods have advanced diverse goals with varying degrees of success. For the purposes of this work, we are interested in atomic analogs to the refractive optical lens, which changes the divergence of a photon beam in order to collimate, focus, or otherwise shape it. Such an element can focus a highly collimated beam into a single, diffraction-limited spot. In addition, a true lens can be used with a transmission mask to project a complex image, as in lithography. In both cases, the goal is to achieve high spatial resolution with maximum flux.

For atom lenses in general, the radial force on particles in a collimated beam should be proportional to their distance from the axis ($F \propto \rho$). This directs all atoms towards a single focal point (Chapter 6). Deviations from this ideal that arise due to the lens potential are referred to as spherical aberrations. Inaccuracies due to variation in the atoms' velocities are called chromatic aberrations. Minimizing both kinds of aberration is the principal goal of atom lens design. Two secondary goals are maximizing flux and minimizing diffraction. Both of these ends are furthered in lenses with large apertures (D) and short focal lengths (f). F-number refers to the ratio f/D. Because of the improved flux they offer when exposing an image, lenses

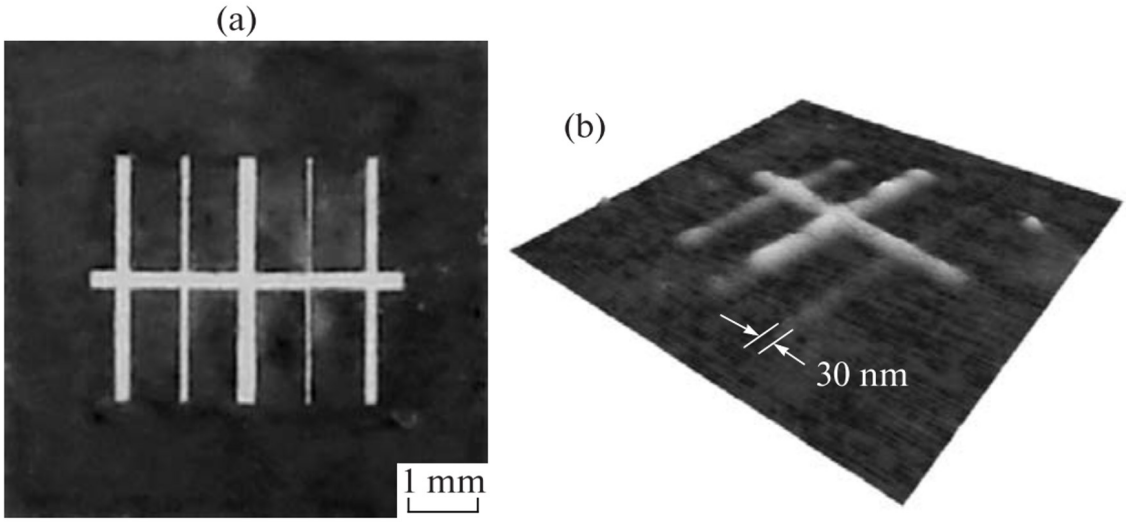

Figure 1.2: An example of results from a recent pinhole lens experiment [21]. A transmission mask (a) forms an object plane for indium atoms that pass through a 20 nm pinhole, forming the image shown in (b) on a silicon substrate. Despite this excellent resolution, pinhole imaging is not a viable option for large-scale nanostructure manufacturing.

with small f-numbers are referred to as fast. A related property is refractive power, which is quantified as 1/f and refers, broadly speaking, to a lens's ability to effect large changes in magnification. It is important to emphasize that some metrics—focal length and chromatic aberration in particular—depend not only on the lens but also on the beam being focused. The best systems for nanoscale atom imaging are powerful, fast, and aberration-free.

1.2 Passive lenses

Some of the simplest atom lenses—pinholes and Fresnel plates—are based on the propagation behavior of particle beams, and involve no direct forces at all. Pinhole lenses were behind the first "camera obscura" photographs, and they are similarly effective in the atomic realm [21, 22, 23]. Classically, a pinhole image is modeled by simply tracing rays through an infinitesimal aperture, yielding a focused image at any distance. In practice, a pinhole lens has a focal range: at long distances diffraction dominates, and in the near-field the pinhole's finite diameter becomes problematic.

It turns out that an ideal pinhole lens has a diameter filling approximately 75% of the first Fresnel zone [22]. This method has been used quite successfully, for example to deposit indium atoms on a silicon substrate with 30 nm resolution (Figure 1.2) [23]. The demagnification factor for pinhole lenses is excellent, reaching easily into the thousands. This allows for the use of micron-scale masks, which are easy to manufacture. Furthermore, a single mask can be used simultaneously with many pinholes, producing an array of images. Despite what one might expect, the nominal speed of pinhole lenses is also reasonable—around f/100—due to their focal lengths on the order of a few micrometers. Unfortunately, pinhole lenses have some obvious drawbacks. For one thing, a lens capable of 30 nm resolution must itself be around 20 nm wide. The flux of an atom beam through an aperture of this size is generally quite low. Depending on the atom source, pinhole clogging and van der Waals forces may also hinder performance. These obstacles make further scale reductions in pinhole systems quite unlikely.

While pinholes lenses are inhibited by diffraction, a complimentary technique—Fresnel zone plate imaging—is based on exploiting it [24, 25, 26]. This approach involves arranging diffraction gratings radially around the axis of the beam. Each diffraction zone diverts atoms towards a common focal point, with resolution improving in proportion to the number and quality of zones. The zero-order beam must be blocked in order to observe the focused first order spot. Additionally, some flux is lost to higher-order diffraction. Because of these losses, the maximum expected efficiency from a zone plate is generally below 10% [26]. While geometric speeds are in the neighborhood of f/1000, beam occlusion and higher-order losses result in effective speeds closer to f/10000. State-of-the-art microfabrication has recently facilitated the construction of Fresnel lenses with up to 2700 zones and grating features on the order of 50 nm (Figure 1.3). Despite these technological advances, zone plates have just barely reached the sub-micrometer regime, and future developments are unlikely to bring them to the true nanoscale. Pinhole lenses and Fresnel plates are unique in their ability to focus any particle, regardless of its electronic configuration. This is especially useful for particles that respond only weakly to electromagnetic fields, such as noble gases in the ground state. However, the flux through these passive lenses is unavoidably small; indeed, their operation is based almost entirely on blocking significant portions of the incident beam. Several higher-efficiency methods instead use electromagnetic forces to create lenses with larger apertures.

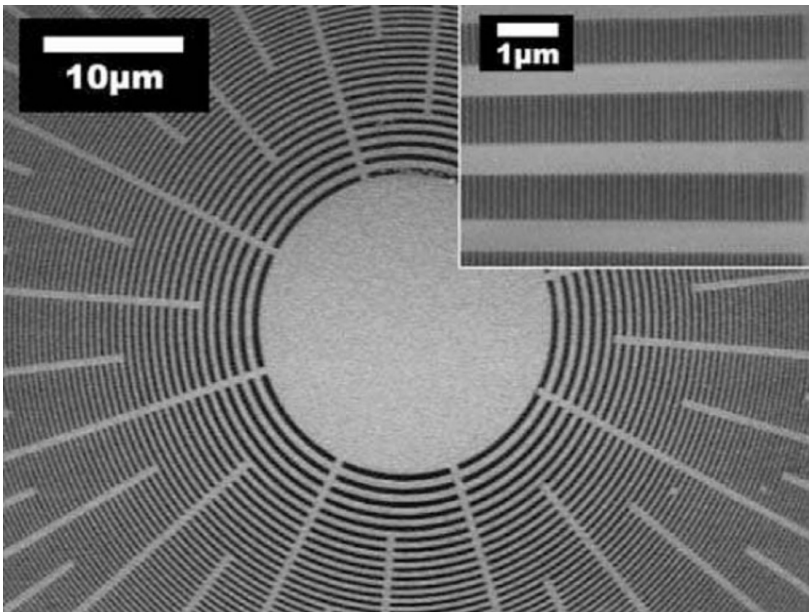

Figure 1.3: SEM images of a typical Fresnel zone plate. This example is made from lithographically etched silicon-nitride [25]. Despite extreme manufacturing requirements—features are on the scale of 100 nm—this device and others like it struggle mightily to produce spots smaller than 1 μm. This SEM micrograph also shows what a large fraction of the incident beam is blocked by the zone plate, leading to low efficiency.

1.3 Standing light wave lenses

Standing light waves, which interact with atoms via the Autler-Townes (AC Stark) effect, can be produced with a simple optical cavity and are amenable to a variety of shaping and tuning techniques [11, 13, 29, 28]. The essential concept of a standing wave lens hinges on the attraction of atoms to high- or low-intensity regions of the near-resonant electromagnetic field. Small period standing waves—which form arrays of "microlenses"—have been used to shape beams of Na, Cs, Cr, and Fe, among others, often with excellent resolution [27]. However, such approaches are limited to relatively simple geometric patterns and do not constitute a general imaging technique (Figure 1.4). Larger standing waves can act as universal lenses, and such systems have focused supersonic He* (v = 1760 $\pm$ 80 m/s) with resolutions around 4 μm and lens speeds of f/11000 [28]. Unfortunately, the sinusoidal potential that characterizes most standing waves is not ideal for focusing. Specifically, the force on an atom is only

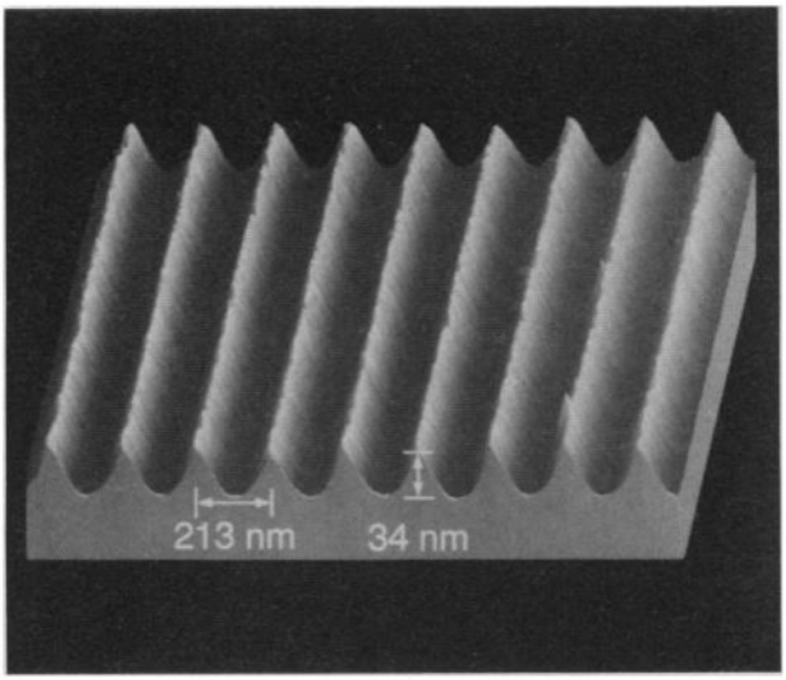

Figure 1.4: Nanoscale rows of chromium deposited using standing light wave lensing. In addition to severe spherical aberration issues, this technique is largely limited to either tiny apertures or simple patterns [27, 28].

proportional to its position ($F \propto \rho$) near the center of a node/antinode, which results in either a background of unfocused atoms or a small effective lens aperture. Clever proposals for low-aberration standing wave lenses with sub-nanometer resolution—for example, based on coaxial $TEM_{01}*$ "doughnut" modes—have circulated for many years, but experimental tests have yet to fulfill their promise [30, 29].

1.4 Static multipole focusing

Static dipole forces—electric or magnetic—offer yet another mechanism for influencing atomic motion. As with standing light waves, a lens based on these forces relies on the attraction of atoms to high- or low-field regions of space via the Zeeman or Stark effects. While quadrupole fields have been used [32, 33], the hexapole field is particularly appropriate, since it satisfies the $F \propto \rho$ condition over a large region and thus acts like a true lens. Electrodes, permanent magnets, and current-carrying wires have all been employed to create focusing fields [20, 33, 34]. In a particularly

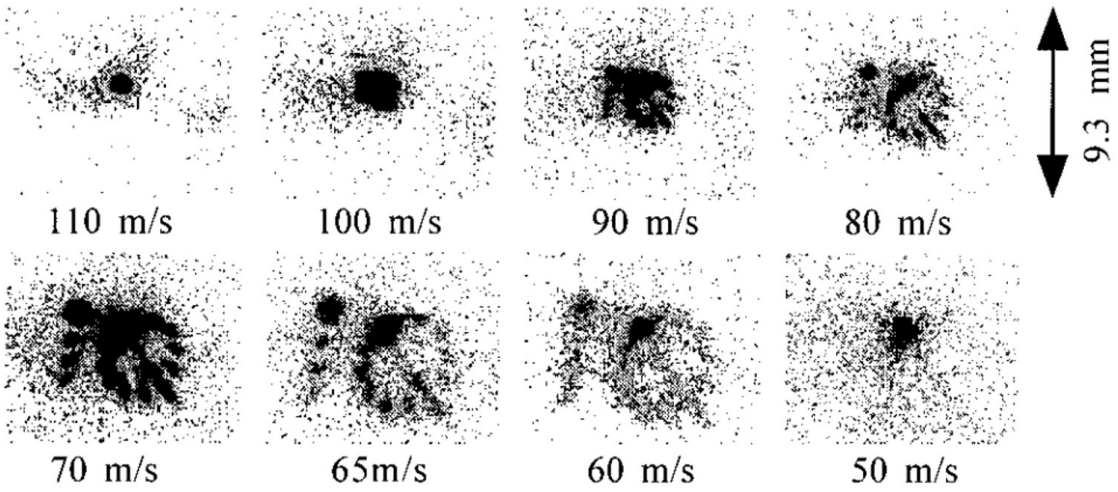

Figure 1.5: True atom imaging from a permanent magnet hexapole [31]. Prior to the work presented in this dissertation, the above image represented one of the best examples of hexapole magnetic focusing. The image sequence shows a beam coming into focus as the longitudinal velocity varies between 110 and 50 m/s. The focused image, around 70 m/s, has features on the scale of 1 mm.

successful example, a permanent magnet hexapole was used to image a complex mask using slowed Cs atoms (v = 0−200 ± 5 m/s) [31]. Though the magnification in this case was of order unity, in principle it could have been improved. Image sizes were on the scale of 0.5 cm, with detail around 1 mm (Figure 1.5). The same system was used to achieve focal lengths as small as 2.5 cm, yielding a minimum observed focal spot on the order of 300 μm. The nominal speed of this system is around f/80, but it must be noted that using a significantly slowed input beam somewhat limits the generality of this result. High-remanance rare earth magnets have improved the power of permanent magnet hexapoles, but focal lengths for fast beams have remained on the order of 10−100 cm [9, 10, 11]. Current-carrying wires can offer stronger field gradients by at least an order of magnitude, but they also produce fringing fields that limit resolution. In addition to refractive power, another serious problem with permanent hexapoles is chromatic aberration. This arises when faster atoms, which require a larger focusing impulse, instead receive a smaller one due to spending less time in the field as they pass through it. The resulting quadratic dependence of focal length on velocity limits the spot size achievable by a steady-state lens.

Table 1.1: Characteristics of various neutral atom imaging systems. Aberration performance is estimated as a grade on the A-F scale. We ignore technology that is not capable of true imaging. From this direct comparison, it is fairly clear that the only real competition for our pulsed, tapered, electromagnetic hexapole is the pinhole. For applications in which the flux through a 20 nm aperture is sufficient and the short, fixed focal length is not a problem, the pinhole is an excellent choice. For any other situation, our system dominates the field.

Lens type ↓	Resolution	Optimal speed	Aberrations
Pinhole	30 nm	f/100	A-
Fresnel plate	1 μm	f/10000	B
Large period standing wave	4 μm	f/10000	B-
Permanent magnet hexapole	300 μm	f/10	C
This project (expected)	10 nm	f/100	A

1.5 Pulsed, tapered, electromagnetic hexapole

We present a pulsed electromagnetic hexapole lens as a solution to many of the problems described above. Modern power-semiconductor technology in the form of the insulated gate bipolar transistor (IGBT) has recently provided a means for switching large currents ($\geq$ 1000 A) on microsecond timescales. This allows for pulsed, high-current wires to exert a brief, strong focusing field on a beam, taking advantage of the high refractive power of electromagnets without subjecting the atoms to fringing fields as they enter and leave the lens. The pulsed configuration also converts focal length into a linear function of velocity, since the time spent in the focusing field is fixed for all particles. Further chromatic aberration correction can be achieved by tapering the lens, thereby applying a stronger force to the faster atoms near the front of the beam. While the pulsed lens can only accommodate similarly pulsed beams, supersonic valves are a perfectly suited source for atom optics experiments. Since these high-brightness beams are already pulsed (often at a very high repetition rate), relatively little flux is lost relative to the CW case. In addition to addressing the problems of refractive power and chromatic aberration, the pulsed electromagnet is tuneable, allowing the user to zoom or focus the lens by simply changing the wire current. This is in contrast to many other methods, where a fixed focal length creates a rather limited set of adjustable properties. After simulating this system for a wide range of input beams, we have constructed a working prototype. Preliminary tests

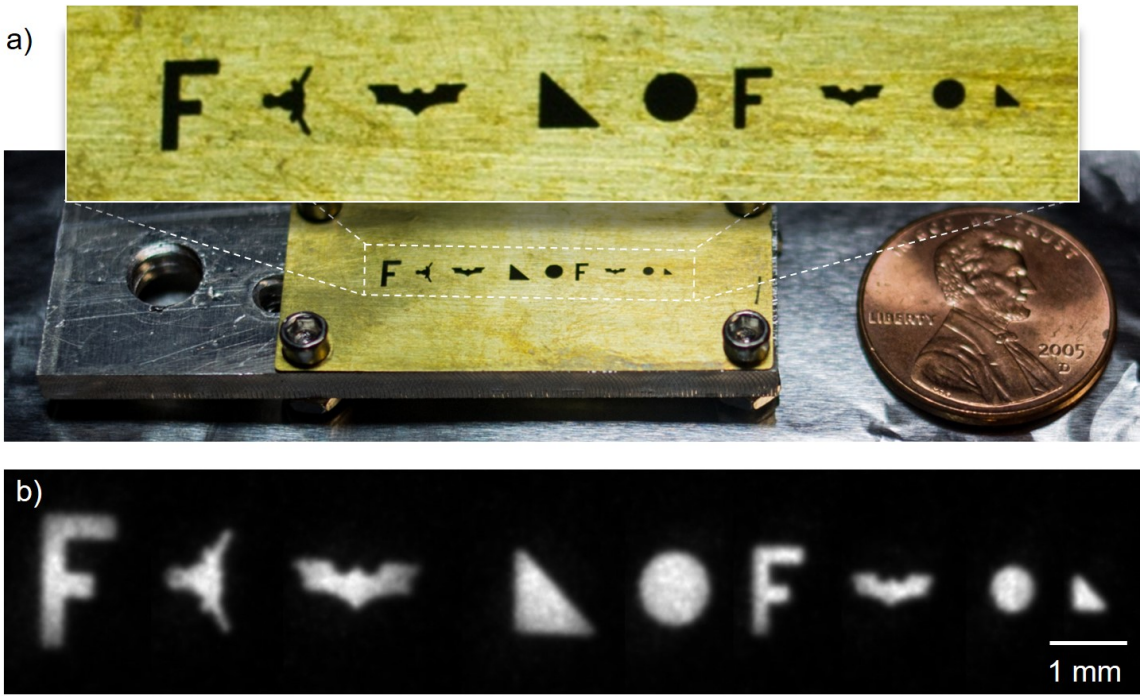

Figure 1.6: A preview of the images we produce using a first-generation prototype of the pulsed electromagnetic hexapole. Our image quality and resolution (along with our choice of shapes, in our opinion) are significantly improved over results from previous hexapole lenses (e.g., Figure 1.5).

using metastable neon (Ne^*) demonstrate true imaging of complex patterns on a size scale smaller than any previous hexapole results (Figure 1.6). We characterize this system at a range of focal lengths and obtain results that compare favorably with theory and simulations. This agreement justifies further exploration of the lens at higher power, where we expect speeds of f/100 and resolution on the order of 10 nm.

1.6 Document summary

This dissertation comprises nine chapters. Chapter 2 describes the theoretical aspects of supersonic atom beams, upon which all of our experimental work depends. In Chapter 3, we examine laser cooling and pumping, both of which feature prominently in our beam preparation process. Chapter 4 offers the mathematical framework we use to understand the behavior of atoms in a magnetic field. In Chapter 5, we apply

this framework to the simple case of a permanent magnet atom mirror. This chapter was published as a paper in 2013 and is not directly relevant to the hexapole focusing described in Chapters 6-9. It does, however, offer a tidy "warm-up" before the more complex discussions that follow. Chapter 6 provides a mathematical description of the pulsed, tapered, electromagnetic hexapole lens, along with results from numerical simulations of the system's performance. In Chapter 7, we describe the experimental details of the beamline used to test a prototype of this lens. Chapter 8 lays out the principal results from several different characterization methods and explains an aberration-correction technique that helped improve these results. Chapter 9 summarizes the current state of the atom focusing project and outlines some long-term goals. Naturally, the reader is urged to skip nothing and to savor each page of this document. In the highly regrettable event that time constraints necessitate triage, Chapters 6 and 8, supplemented with the figures in Chapter 7, should offer a clear picture of the work we wish to present.

Chapter Two: Supersonic beams

The starting point of this experiment, a pulsed, supersonic Even-Lavie valve, yields an extremely intense and directional beam of neon. Compared to their effusive counterparts, supersonic beams are significantly brighter and colder, but they also have higher mean velocities. It is worth spending a few pages to investigate the formation and behavior of these sources, which are increasingly crucial tools in atomic and molecular physics.

2.0.1 Effusive beams

The first molecular beams were formed by Dunoyer in 1911 by heating a cell to produce sodium vapor, which was allowed to escape through a small aperture [16]. Dunoyer observed that the beam thus-formed followed straight lines and did not "go around obstacles, as would so-called gas jets, which form swirls so as to leave no empty space[1]." This description goes straight to the heart of effusive beam formation, whose essential feature is that gas particles pass into vacuum with no disturbance to their velocity statistics.

A more rigorous statement of this condition is that the mean free path, Λ, of the gas in the reservoir is large compared to the dimensions of the aperture. The mean free path for a member of a Maxwellian ensemble is given by

$$\Lambda = \frac{1}{n\sigma\sqrt{2}} = \frac{k_B T}{P\sigma\sqrt{2}}, \tag{2.1}$$

where $n = N/V$ is the number density of the gas, σ is the the effective cross sectional area of a gas particle, T is the gas temperature, and P is the pressure [35]. Atoms in the reservoir are contained by its walls. An effusive beam is formed by removing a section of the reservoir wall in such a way that particles simply pass through the resulting aperture without experiencing any unexpected collisions. This lack of collisions is a way of saying that information does not propagate from the hole to the

[1] "Cette expérience prouve d'abord que la matière en mouvement qui va former le dépôt H ne contourne pas les obstacles, comme le ferait ce qu'on a l'habitude d'appeler un jet de gaz qui formerait des remous derrière eux de manière à ne pas laisser d'espace vide. De plus il est facile de reconnaître que la propagation de cette matière se fait en ligne droite."

atoms in the effusive beam: for all the atoms "know," they are still inside the reservoir. The beam's velocity statistics are therefore the same as those of the reservoir gas, with the restriction that the forward velocity must be suitable for escape. The isotropic Maxwellian speed distribution can be written:

$$f(v) = \frac{4}{\sqrt{\pi}} \left(\frac{m}{2k_B T} \right)^{3/2} v^2 \exp\left(-\frac{mv^2}{2k_B T} \right), \tag{2.2}$$

where v is the speed and m is the molecular weight. It is noteworthy that the peak of this distribution—that is, the most probable speed—occurs at

$$v_W = \sqrt{\frac{2k_B T}{m}}. \tag{2.3}$$

In other words, the most probable kinetic energy in the beam is equal to $k_B T$. The angular distribution depends on the thickness of the reservoir walls, but can approach 2π steradians.

Because high brightness is often desirable, many early atom beam experiments attempted maximize beam flux by increasing reservoir pressure. Unfortunately, this had the effect of reducing the mean free path, paradoxically causing gas to accumulate around the aperture and effectively clogging the flow [36].

2.0.2 Adiabatic expansion

The problem of low brightness in effusive beams was eventually solved by better control over the gas expansion process [37]. The accumulation of gas around a clogged aperture is clearly mitigated if the particles leave the reservoir at a high average velocity, making room for new particles to follow. Supersonic nozzles accomplish exactly this by converting a large fraction of the gas's initial enthalpy into translational energy. This is doubly advantageous for many applications, as it both increases particle flux and narrows the temperature of the resulting beam. For more detail on the following discussion, see [35].

We begin by considering an ideal gas passing through a channel of dimensions much larger than the mean free path. This condition allows us to treat the gas as a compressible fluid rather than a statistical ensemble of discrete entities. We assume the gas fills the channel completely and does not exchange heat with its surroundings. Each volume element of the gas is effectively bounded by the surrounding particles.

This is in contrast to the previous (free expansion) case, in which the behavior of particles in the aperture was purely ballistic. A useful form for the equation of state is:

$$P = nk_BT. \tag{2.4}$$

The first law of thermodynamics can be expressed in terms of heat q and internal energy e per unit mass:

$$dq = de + Pd(1/\rho), \tag{2.5}$$

where ρ is density and $1/\rho$ is effectively the volume of a unit mass. The specific enthalpy h is similarly written as a sum of internal and mechanical energy per unit mass:

$$h = e + \frac{P}{\rho}. \tag{2.6}$$

For an adiabatic process ($dq = 0$),

$$c_P \frac{d\rho}{\rho} = c_V \frac{dP}{P}, \tag{2.7}$$

where

$$c_P = \left(\frac{\partial h}{\partial T}\right)_P \tag{2.8}$$

and

$$c_V = \left(\frac{\partial e}{\partial T}\right)_V \tag{2.9}$$

are the constant-pressure and constant-volume specific heats, respectively. It is useful to define

$$\gamma = \frac{c_P}{c_V}. \tag{2.10}$$

Integrating equation 2.7, we obtain the well known relation:

$$\frac{P_2}{P_1} = \left(\frac{T_2}{T_1}\right)^{\gamma/(\gamma-1)}, \tag{2.11}$$

which is a concise expression of the idea that an adiabatic expansion into a low pressure region ($P_2 < P_1$) results in a lower temperature ($T_2 < T_1$). Intuitively, it is useful to connect the collisional gas in a nozzle to the more canonical "receding piston" of undergraduate homework fame. For a gas with a short mean free path, the boundaries of any centrally located volume element are formed by the neighboring gas

particles. If the entire cloud is expanding—specifically in the longitudinal direction—these boundaries act as receding walls, cooling the center of the cloud.

We have argued that a collisional beam expanding through a nozzle will cool down, but we have not yet shown how this thermal energy is converted into forward velocity. Defining the sound speed in a gas as

$$c = \sqrt{\gamma \frac{P}{\rho}}, \tag{2.12}$$

we obtain:

$$\frac{dP}{\rho} = c^2 \frac{d\rho}{\rho}. \tag{2.13}$$

In one dimension, the continuity equation from fluid dynamics can be written:

$$\frac{dv}{v} + \frac{d\rho}{\rho} + \frac{dA}{A} = 0, \tag{2.14}$$

where v is the flow speed and A is the cross sectional area of the channel. Similarly, the momentum equation takes the form:

$$vdv = -\frac{dP}{\rho}. \tag{2.15}$$

Combining equations 2.13, 2.14, and 2.15 yields:

$$\frac{dA}{A} + \frac{dv}{v}\left(1 - M^2\right) = 0., \tag{2.16}$$

where we have define the Mach number as $M = v/c$. For $M < 1$, it is clear from equation 2.16 that the flow rate decreases with increasing area. This is in keeping with our intuitive understanding of normal fluid flow. However, a strange regime exists when $M \geq 1$. For this case, flow rate increases with increasing cross section, provided there is a position along the channel for which M crosses 1. It turns out that this transition into the supersonic regime consistently occurs at the choke point, where the nozzle area is minimal and $dA = 0$. A so-called Laval nozzle, which is designed to create these conditions, narrows to a minimum cross section before gradually widening again. The resulting beam is quite fast and cold compared to the gas in the reservoir. An imperfect analogy for this situation is traffic flow. When road work constricts a highway, traffic slows accordingly. If the blockage is bad enough, bumper-to-bumper traffic ensues. As the blocked lanes reopen, cars rapidly accelerate—often to a much

higher speed than they could maintain upstream. Unfortunately this analogy cannot be pursued too far, not least because it is hard to imagine a regime in which cars act like a "normal" fluid, speeding up when flow is restricted. Returning one last time to classical fluid dynamics, we have the energy equation in one dimension:

$$vdv = -dh. \tag{2.17}$$

Integrating, we obtain:

$$\frac{v_2^2 - v_1^2}{2} = h_1 - h_2. \tag{2.18}$$

This is an explicit statement of the idea that the beam is formed by converting the enthalpy of the original gas into translational kinetic energy. Using the definition of c_P and taking $v_1 \approx 0$, this becomes

$$v_2^2 = 2c_P T_2 \left(\frac{T_1}{T_2} - 1\right). \tag{2.19}$$

The final Mach number is therefore:

$$M_F = \sqrt{\frac{2}{\gamma - 1}\left(\frac{T_1}{T_2} - 1\right)} = \sqrt{\frac{2}{\gamma - 1}\left(\left(\frac{P_1}{P_2}\right)^{(\gamma-1)/\gamma} - 1\right)}. \tag{2.20}$$

To the extent that the final pressure P_2 can be made arbitrarily small, the final Mach number is effectively unbounded. Recalling that the sound speed c in the outgoing beam is proportional to $\sqrt{T}$, we see that this large Mach number ($M = v/c$) reflects the notion that thermal energy in the original gas has been converted into translational energy. An enormous Mach number—despite evoking images of science fiction and warp drives—simply reflects the fact that the most probable velocity in the beam is much larger than $\sqrt{2k_B T_\parallel/m}$ (Here we have labeled the longitudinal temperature, which arises from the longitudinal velocity spread in the co-moving frame, as $T_\parallel$. Similarly, the transverse velocity spread gives rise to $T_\perp$.). Coming full circle, we note that the beam velocity in the limiting case of $T_2 = P_2 = 0$ is very nearly the median speed of the reservoir gas:

$$v_{max} = v_W \sqrt{\frac{\gamma}{\gamma - 1}} = \sqrt{\frac{2k_B T_\parallel}{m}\left(\frac{\gamma}{\gamma - 1}\right)}. \tag{2.21}$$

In the somewhat more realistic case of a finite final temperature, we can model the three-dimensional velocity distribution as an anisotropic Maxwellian in $\boldsymbol{v} \equiv \boldsymbol{v}_\perp + \boldsymbol{v}_\parallel$:

$$f(v_\perp, v_\parallel) = \frac{m}{2\pi k_B T_\perp}\left(\frac{m}{2\pi k_B T_\parallel}\right)^{1/2} \exp\left(-\frac{m v_\perp^2}{2k_B T_\perp} - \frac{m(v_\parallel - v_2)^2}{2k_B T_\parallel}\right). \tag{2.22}$$

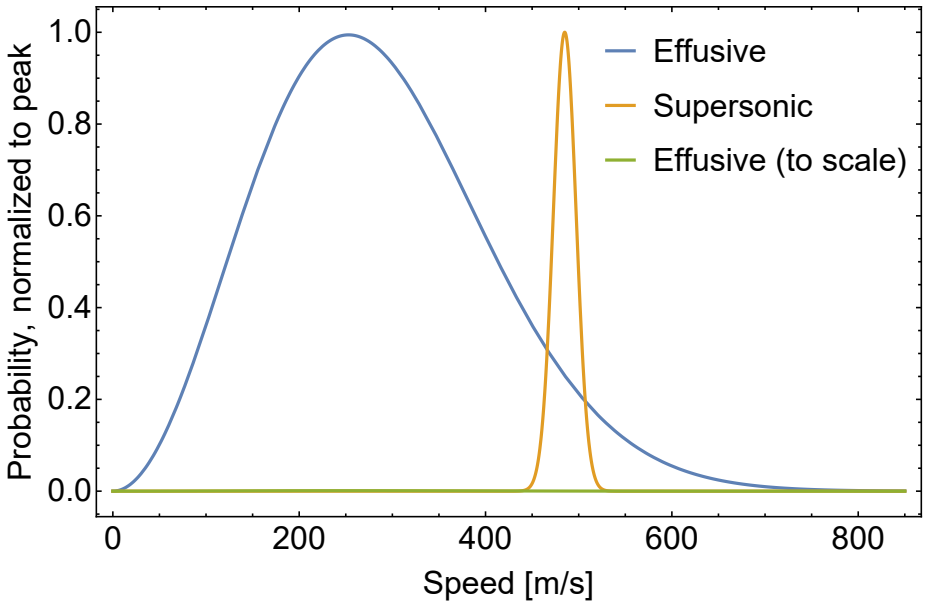

Figure 2.1: Velocity distributions for effusive and supersonic beams of neon from a 77 K source. It is common to emphasize the relative narrowness of the supersonic beam, but a far more important characteristic is the 1000-fold improvement in brightness.

Note the slightly awkward flavor difference between $\boldsymbol{v}$—the vector velocity of an individual atom—and v_2, which is the final speed of the compressible fluid after the adiabatic expansion. It may be more pleasing to the Statistical Mechanics Deities if we redefine v_2 as the average velocity in the longitudinal direction. Because the perpendicular temperature mostly manifests as a reduction in flux, we can focus exclusively on the parallel distribution, obtaining a Gaussian:

$$f(v_\parallel) \propto \exp\left(-\frac{m(v_\parallel - v_2)^2}{2k_B T_\parallel}\right). \tag{2.23}$$

Figure 2.1 compares the velocity distributions of effusive and supersonic beams. In many ways, the most important contrast is not the narrower distribution, but rather the enormous difference in brightness. While effusive beams top out around 10^{20} atoms/(sr $\cdot$ s $\cdot$ cm^2), supersonic beams are regularly three orders of magnitude brighter [35]. The use of shaped Laval nozzles to produce cold, intense atom beams has become quite common. While the three dimensional case involves significantly more complex dynamics, the main lessons of this section remain valid. The Even-Lavie valve—a state-of-the-art application of the physics described here—is discussed in Chapter 7.

2.1 Phase space

This is a convenient time to introduce the concepts of phase space density and the phase space diagram. In classical physics, we think of phase space density ρ as the probability that a particle occupies a region spanned by ($\delta\boldsymbol{r}$, $\delta(m\dot{\boldsymbol{r}})$) around a given location in phase space $(\boldsymbol{r}, m\dot{\boldsymbol{r}})$. Put another way, ρ is the number N of particles occupying a "unit" of 6-dimensional (3 space, 3 momentum) volume. The atomic physics analog is quite similar, with the added bonus of being dimensionless. For an atomic ensemble with isotropic thermal DeBroglie wavelenghth $\lambda_{th} \equiv \hbar/(mv_W) = \hbar/\sqrt{2k_BTm}$, the phase space density is:

$$\rho = \frac{\lambda_{th}^3 N}{V} = \frac{\hbar^3 N}{(mv_W)^3 V}, \tag{2.24}$$

where V is the occupied spatial volume and v_W is as defined in Equation 2.3. This definition amounts to the selection of $\hbar^3$ as the elementary unit of volume. We can adapt this to non-isotropic beams by allowing the phase space extent in each dimension to contribute separately:

$$\rho = \frac{N\hbar^3}{(\delta x\, \delta y\, \delta z\, \delta\dot{x}\, \delta\dot{y}\, \delta\dot{z})m^3}. \tag{2.25}$$

Phase space diagrams provide a visual aid in the discussion of ρ. Figure 2.2 shows one such diagram comparing the output of a supersonic nozzle to that of an effusive beam. Even if the number of particles in the two regions were the same, ρ in the supersonic case would be much higher. We estimate the phase space density for our beam after the skimmer to be on the order of 10^{-11}. For comparison, a thermal beam from an oven yields $\rho \approx 10^{-16}$ [38].

An important concept to keep in mind is that—in most cases—phase space density is conserved. While it may *seem* possible to brighten a beam—for example, by applying some sequence of focusing fields—almost any concentration of the beam in one dimension is balanced by an expansion in another. The classic example is a lens, which transforms a collimated, wide beam into a divergent, focused one. The rigorous proof of this conservation law relies on a version of Liouville's theorem, an excellent discussion of which can be found in [39]. Most specifically relevant to us is the following statement: no force that can be described within the framework of Hamiltonian mechanics—more explicitly, no "cooling [scheme] that rely[s] on resonance transitions

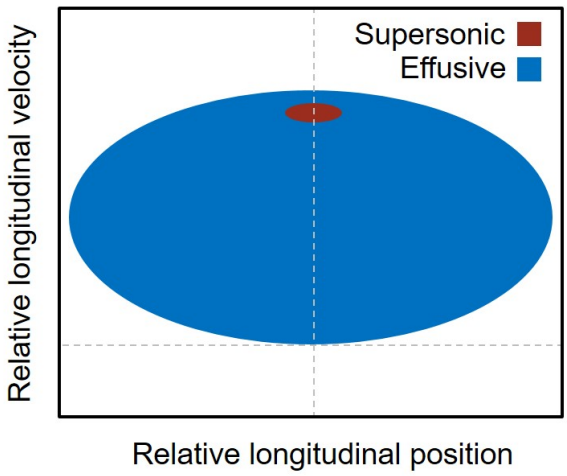

Figure 2.2: Phase space diagram sketches for effusive and supersonic beams. This introduces a useful way to visualize phase space volume. The effusive beam occupies a large volume in both position and momentum space. The supersonic beam has a higher average velocity, but its phase space volume is dramatically smaller. Since the number of particles occupying the supersonic beam region is—if anything—larger than for the effusive beam, the phase space density for a supersonic beam is significantly larger.

or time-dependent potentials"—can result in a brighter beam. The basic classical calculation on which this statement rests extends quite robustly into the quantum realm [40]. Many ingenious schemes for achieving miraculously high phase space density have been dashed on the rocks of this theorem. One way to escape its clutches—as in the case of optical cooling—is by applying a non-conservative force that depends on both position and velocity. Because such a force cannot be described in the Hamiltonian formalism, it is exempt from the Liouville theorem. In the next several chapters, we will often return to the concept of phase space transformations.

Chapter Three: Cooling and pumping

Despite the improved brightness of nozzle beams over simple effusive atom sources, further intensification is immensely helpful. Laser cooling offers one of very few approaches to true brightening of an atom ensemble. Because we eventually want only one magnetic species, optical pumping is also quite helpful. The discussion in this chapter loosely follows that of Metcalf in [39].

3.1 Selection rules and scattering rates

From perturbation theory, we can describe the incoherent transition rate γ between two atomic states $|e\rangle$ and $|g\rangle$ as depending on the matrix element μ_{eg} in the Hamiltonian that connects them:

$$\gamma \propto |\langle e|H'|g\rangle|^2 \equiv |\mu_{eg}|^2. \tag{3.1}$$

For the electromagnetic field, the relevant portion of the Hamiltonian takes the form of a dipole moment:

$$H' = e\,\hat{\boldsymbol{\varepsilon}} \cdot \boldsymbol{r}, \tag{3.2}$$

where $\hat{\boldsymbol{\varepsilon}}$ is the unit polarization vector of the light. Since our atomic states are most easily expressed in terms of spherical harmonics, we rewrite H' in this form as well, using:

$$\hat{\boldsymbol{\varepsilon}} \cdot \boldsymbol{r} = \sqrt{\frac{4\pi}{3}} r Y_{1q}(\theta, \phi), \tag{3.3}$$

where q indicates linear ($q = 0$) or circular ($q = \pm 1$) polarization. Separating the radial and angular components of the atomic electron wavefunction, we obtain:

$$\mu_{eg} = e\langle n'l'|r|nl\rangle\langle l'm'|\sqrt{\frac{4\pi}{3}} r Y_{1q}|lm\rangle. \tag{3.4}$$

This matrix element yields the well known selection rules,

$$m' = m + q \tag{3.5}$$

$$l' = l \pm 1, \tag{3.6}$$

Table 3.1: Selected properties of the $3^3P_2 - 3^3D_3$ transition in $^{20}Ne^*$ [39].

Quantity	Value
Wavelength [nm]	640.402
Energy [eV]	1.936
Lifetime [ns]	18.79
Linewidth ($\gamma/2\pi$) [MHz]	8.47
Saturation intensity [mW/cm^2]	4.22
Doppler limit (v_d) [cm/s]	29.07
Doppler limit (T_d) [μK]	203.29
Recoil limit (v_r) [cm/s]	3.116
Recoil limit (T_r) [μK]	2.335

which become especially useful for optical pumping.

Shifting gears away from the detailed atomic states, we can write γ as

$$\gamma = \frac{\omega^3 |\mu_{eg}|^2}{3\pi\epsilon_0 \hbar c^3}, \tag{3.7}$$

where ω is the light frequency. Taking into account all elements of the density matrix, we write down a set of master equations—the Optical Bloch Equations. Defining the saturation intensity as

$$I_0 = \frac{\pi h c \gamma}{3\lambda^3} \tag{3.8}$$

and solving the master equations for equilibrium, we calculate the total scattering rate:

$$\gamma_p = \frac{(I/I_0)(\gamma/2)}{1 + I/I_0 + [2(\delta)/\gamma]^2}. \tag{3.9}$$

Here $\delta = \omega - \omega_a$ is the detuning from atomic resonance and I is the light intensity. This rate will be the starting point for our optical cooling calculation.

3.2 Structure of metastable neon

It is useful to briefly outline the relevant optical and electronic properties of metastable neon (Ne^*). The electron bombardment process serves to remove a (2p) electron from the ground state atom, placing it instead in the n=3 shell. The resulting electron configuration is $(1s)^2(2s)^2(2p)^5(3s)$. The lowest energy triplet states are 3^3P_0, 3^3P_1, and 3^3P_2, where we use standard Russel-Saunders notation of the form $n^{2S_{total}+1}L_J$.

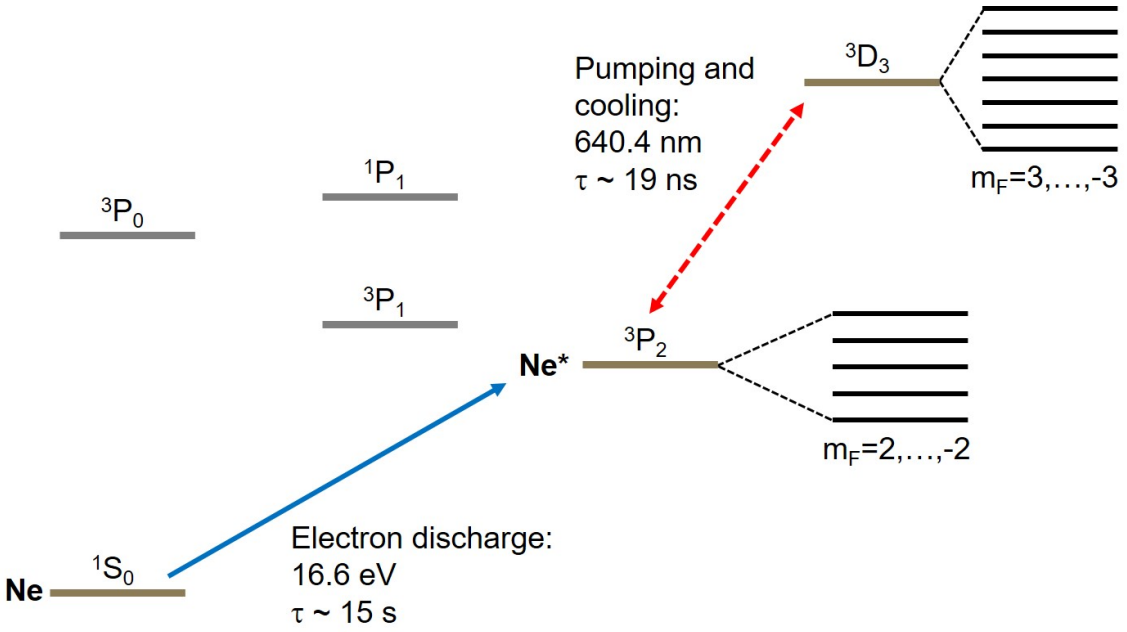

Figure 3.1: An energy level diagram showing the important features of Ne*. Due to selection rules that prevent relaxation, the metastable $^3P_2$ state has a nearly eternal lifetime of 14.73 s. These selection rules go out the window as soon as the symmetries upon which they depend are broken. This defenestration results in a fast relaxation event, which is the phenomenon we exploit for detection, metastable microscopy, and neutral atom lithography.

The J=0 and J=2 states are metastable, and there exists a closed cycling transition between the metastable 3^3P_2 state and the nearby 3^3D_3 state (Figure 3.1). Some properties of this transition are outlined in Table 3.1. The 3^3P_2 state and the 3^3D_3 state have 5 and 7 sublevels, respectively, corresponding to the $2J + 1$ eigenvalues of J_z. The angular momentum characteristics of these sublevels will be discussed in Chapter 4.

3.3 Laser cooling

The goal of any cooling process is to remove kinetic energy from an ensemble. Laser cooling accomplishes this by selectively interacting with high-speed particles, leaving others undisturbed. This process is depicted schematically for one dimensional cooling in Figure 3.2. The narrow linewidth of atomic transitions is extremely helpful in this

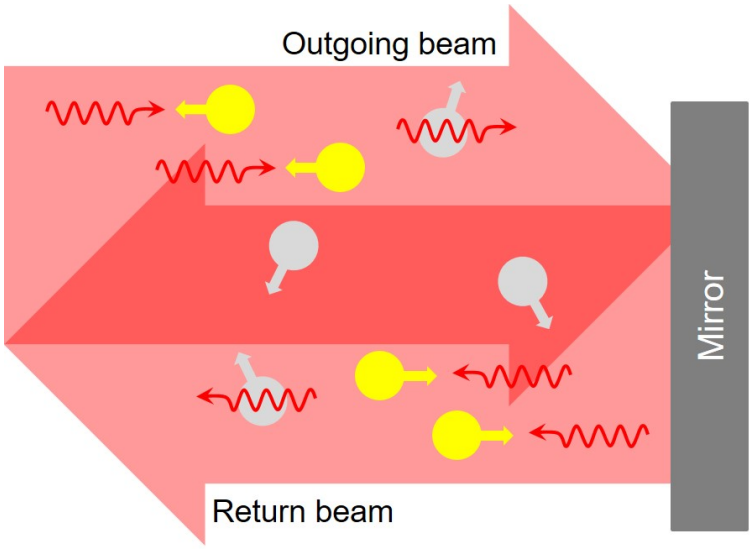

Figure 3.2: A schematic depiction of optical molasses in one dimension. The laser light is red-detuned from resonance by approximately one linewidth. This suppresses its interaction with stationary atoms. However, when an atom's relative speed blue-shifts the laser light back into resonance, the scattering rate increases dramatically. The scattered photons deliver a momentum kick to the moving atoms that, on average, slows them down. The net result from two counter-propagating laser beams is to cool the atomic ensemble.

respect, as it allows for the targeting of specific velocity classes.

A single laser beam interacting with a quasi-two-level atom scatters light with the rate given in Equation 3.9. We adapt this to the case of atoms in motion by adding a Doppler shift to the detuning:

$$\gamma_P = \frac{(I/I_0)(\gamma/2)}{1 + I/I_0 + [2(\delta + \omega_D)/\gamma]^2}. \tag{3.10}$$

Here $\omega_D = -\boldsymbol{k} \cdot \boldsymbol{v}$ is the shift due to projection of the atom's velocity, $\boldsymbol{v}$, onto the laser wave vector, $\mathbf{k}$. It is intuitively clear that a red-shifted laser will selectively scatter atoms whose velocity contributes a blue-shift, such that $\delta \approx -\omega_D$. Since each scattering event involves (on average) a momentum kick of $\hbar\boldsymbol{k}$, the net effect of a red-shifted laser is to slow down the atoms moving towards it. Two counter-propagating beams, each red-shifted by around a linewidth, will therefore produce a force curve of the form:

$$\mathbf{F}(\mathbf{v}) = \frac{\hbar \mathbf{k} \gamma}{2} \left(\frac{I/I_0}{1 + I/I_0 + [2(\delta - |\omega_D|)/\gamma]^2} + \frac{I/I_0}{1 + I/I_0 + [2(\delta + |\omega_D|)/\gamma]^2} \right). \tag{3.11}$$

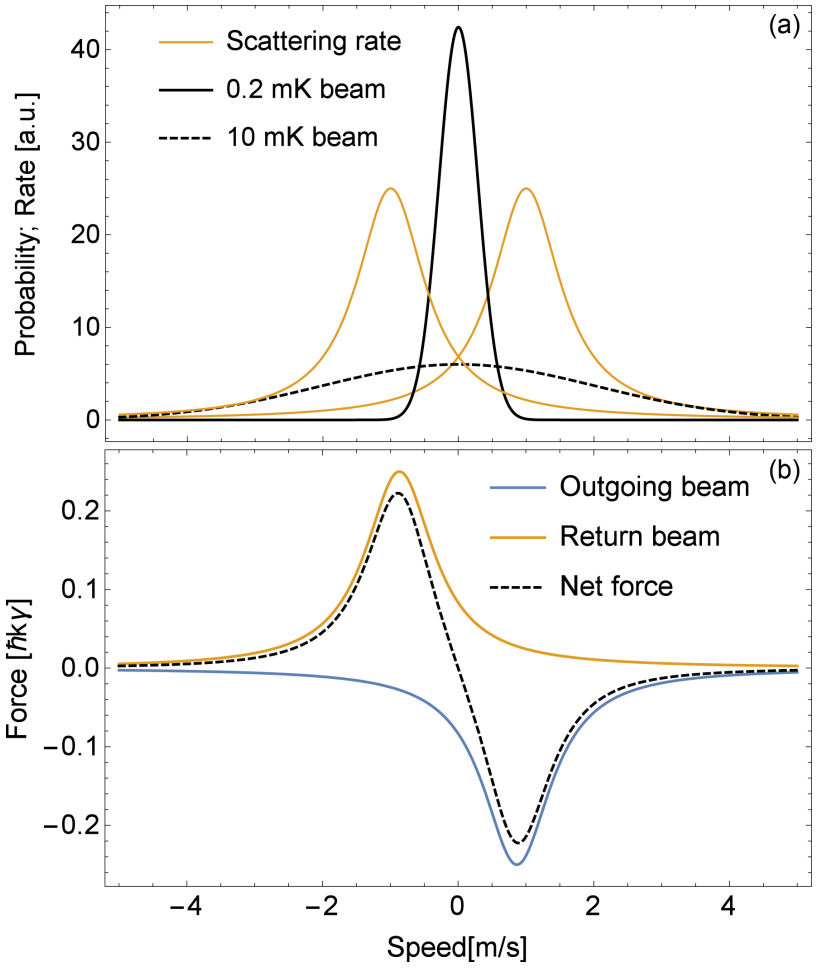

Figure 3.3: Two plots depicting the operation of an optical molasses in one dimension. In (a), the scattering rate from both cooling beams is overlaid with the initial and final velocity distribution for a cooled Ne* ensemble. This figure gives an intuitively reasonable picture of the relationship between the Doppler limit (200 μK) and the peak scattering rates for detuning on the order of γ. In (b), the net force curve is constructed as a sum of forces from the two individual beams. For atoms within 1 m/s of rest, the beams exert a dissipative drag force.

This force is plotted in Figure 3.3, from which it is clear that atoms near the center of the velocity distribution experience a force that is linearly proportional to $-v$. This is exactly what we require from a "drag force." Explicitly, $F \approx -\beta v$, with

$$\beta = \frac{8\hbar k^2 \delta I/I_0}{\gamma(1 + I/I_0 + (2\delta/\gamma)^2)^2}. \tag{3.12}$$

Without taking additional steps to circumvent it, the Doppler limit defines the ap-

proximate minimum temperature that can be reached with optical cooling. In Ne*, this is on the order of 200 μK.

3.3.1 Chirped longitudinal brightening

For fast atomic beams, implementing a full "moving molasses" in the longitudinal direction requires independently Doppler shifting the co- and counter-propagating laser beams into the rest frame of the atoms. This is more involved than transverse cooling, in which a single mirror suffices to provide a return beam. A simplified approach uses a single counter-propagating beam with a time-dependent Doppler shift:

$$\mathbf{F}(t) = \frac{\hbar \mathbf{k} \gamma}{2} \left(\frac{I/I_0}{1 + I/I_0 + \left[2\left(\delta(t) + \omega_D\right)/\gamma\right]^2} \right). \tag{3.13}$$

If the initial detuning is selected to correspond to the beam's fastest moving atoms, these will be slowed until they merge with the rest of the beam. The laser detuning can then be shifted into resonance with the new fastest atoms, effectively scooping the whole beam into the lowest velocity class. This process is depicted schematically in Figure 3.4. The practical details of this technique are described in Chapter 7.

3.4 Optical pumping

The success of this project depends on our ability to pump the atoms in our beam into a single low-field-seeking (LFS) state. Taking into account the selection rule in Equation 3.5, we use circularly polarized light to pump all atoms in the beam into the $m_J = 2$ state. This process is depicted in Figure 3.5. It is important to keep in mind the splitting that takes place between the various magnetic states. While a background field is essential for maintaining a quantization axis, it can also shift certain transitions out of resonance. This splitting will be described in more detail in Chapter 4. Some of the more practical aspects of optical pumping are laid out in Chapter 7.

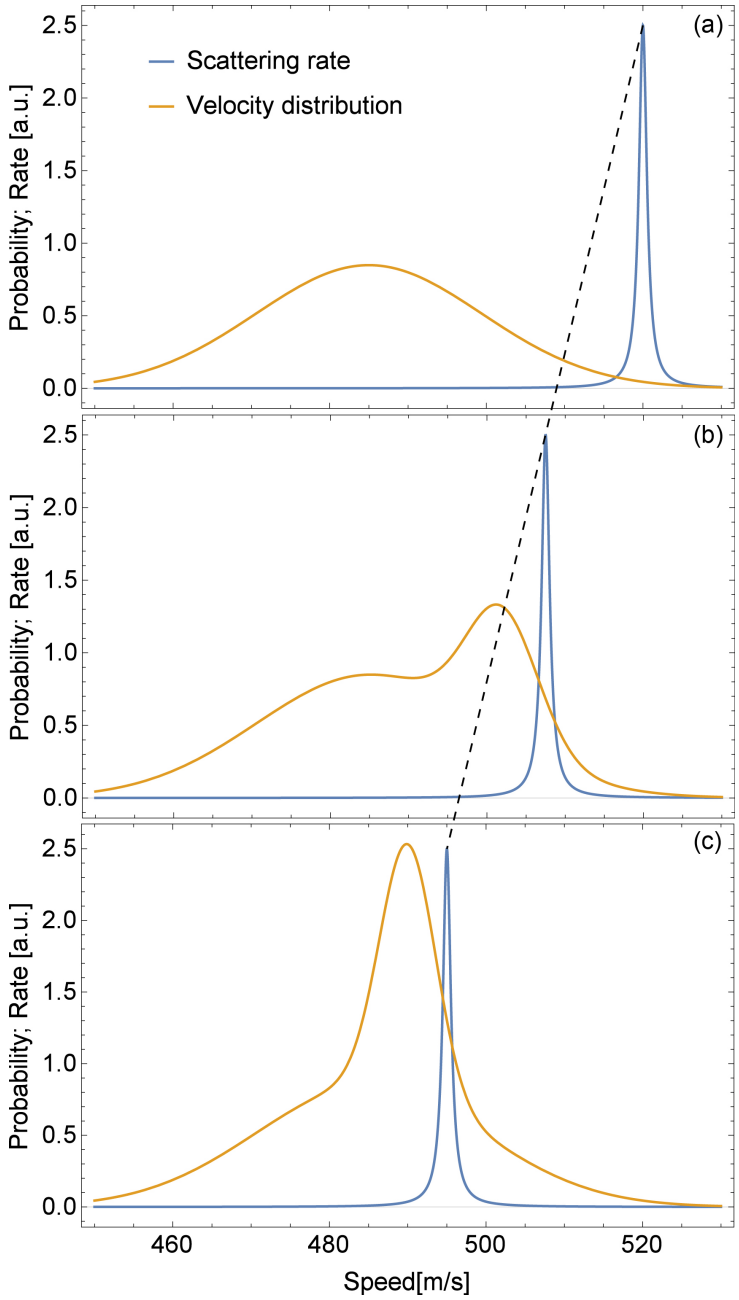

Figure 3.4: Chirped longitudinal brightening. (a) Initial detuning is selected to produce resonance with the beam's fastest atoms. (b) As these atoms slow, we shift the laser frequency into resonance with those moving more slowly. (c) Eventually, the beam scoops a large fraction of the beam into a narrower velocity distribution. This chirp can continue as long as necessary, resulting in a significantly slowed final beam [31]. The dotted line represents the smooth sweep of the scattering spectrum over time.

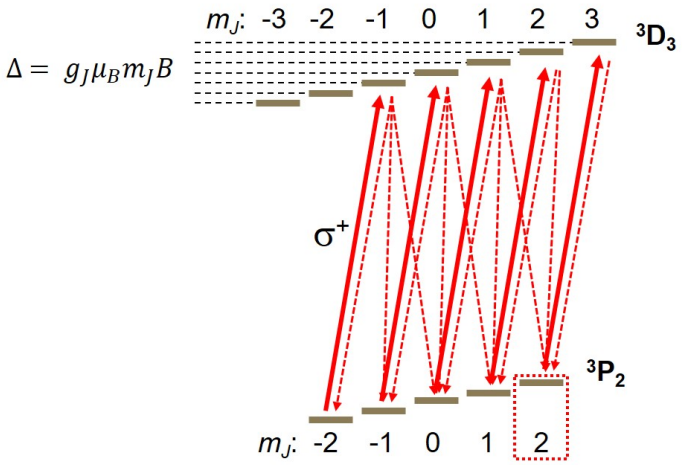

Figure 3.5: An energy level diagram showing the magnetic sublevels for the $^3P_2$ and $^3D_3$ states of the cycling transition for Ne*. Circularly polarized light yields a unitary change in quantum number m_J. While spontaneous decay can link any adjacent states, the net effect of many consecutive transitions is to collect all atoms in the $m_J = 2$ sublevel. The Zeeman splitting due to an external magnetic field—Δ; greatly exaggerated here—slightly changes the resonance condition between various states. When applying a quantization field, is important to keep it small enough that the transitions remain within a linewidth of the pumping laser.

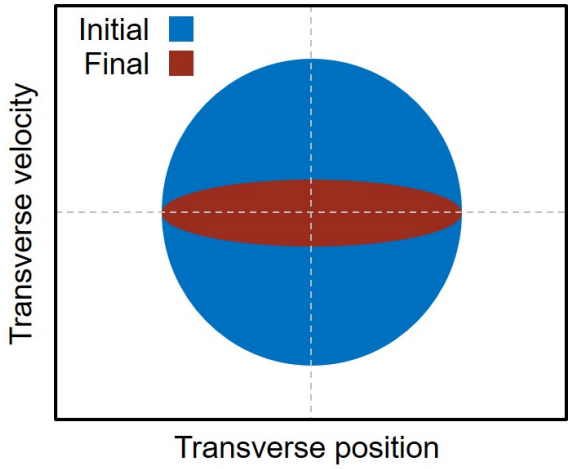

Figure 3.6: Phase space diagram of transverse laser cooling in 1D. The counter-propagating, red-detuned cooling beams slow down fast atoms and leave the others alone. This results in a substantially narrowed velocity spread without any change in spatial extent. The velocity-dependent force exerted by the optical molasses is non-conservative, which allows it to skirt the restrictions of Liouville's theorem.

3.5 Phase space

As advertised, we now return to the concept of phase space density to see how the material in this chapter fits. Optical cooling, by virtue of exerting a dissipative, velocity-dependent force, is exempt from the restriction placed by Liouville's theorem on phase space density. It is the only technique used in this dissertation that actually brightens the beam, rather than simply changing the phase space distribution. As the cooled atoms go from a high- to a low-entropy state, it is helpful to observe that the low-entropy laser beams used for cooling undergo a commensurate entropy increase [41]. Figure 3.6 sketches the phase space volumes occupied by the beam before and after transverse cooling. The main feature to note is that the final volume is significantly smaller, which implies a density increase. It is also significant that transverse cooling exerts no focusing force: the beam's spatial extent remains unchanged. This is an important distinction between an optical molasses and related techniques, such as the magneto-optical trap. Figure 3.7 shows a similar diagram for the chirped longitudinal cooling. In addition to a higher phase space density, the final beam in this case has a distinctly lower average velocity.

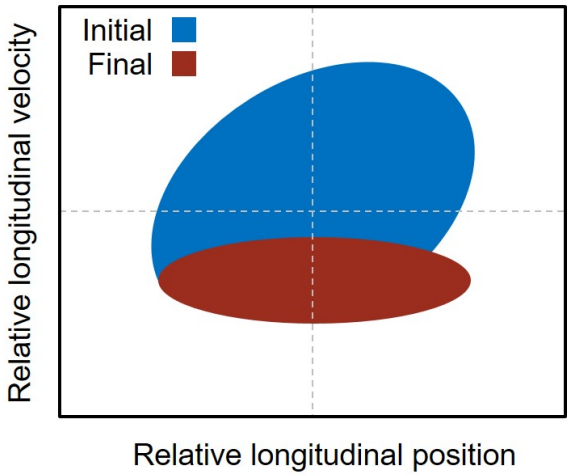

Figure 3.7: Phase space diagram for chirped longitudinal cooling. Fast atoms are sequentially swept into the slowest velocity class. This still results in beam brightening, though the density change is not as pronounced as for a true optical molasses. Depending on how far the chirp is carried, the median velocity afterwards may be slower than that of the initial beam.

Chapter Four: Atoms in a magnetic field

The focusing scheme described in this work depends crucially on the interactions of atoms with magnetic fields. We introduce this concept with a classical picture, then proceed with a more realistic description. After considering the quantization of angular momentum and adiabatic following, we discover that the quantum mechanical perspective is actually simpler than its classical counterpart.

4.1 Classical picture

The force on a dipole is most intuitive in the context of a cartoon "ball and stick" model. If we momentarily suspend the laws of physics, we can imagine a magnetic dipole to consist of two magnetic monopoles (charge $\pm m$) rigidly connected and separated by a vector $\boldsymbol{d}$. Adding a magnetic field $\boldsymbol{B}(\boldsymbol{r})$, the total force on the dipole is simply

$$\boldsymbol{F} = m\boldsymbol{B}(\boldsymbol{r_1}) - m\boldsymbol{B}(\boldsymbol{r_2}), \tag{4.1}$$

where $\boldsymbol{r_1}$ and $\boldsymbol{r_2}$ are the locations of the positive and negative magnetic charges, respectively. Clearly, the force is zero if $\boldsymbol{B}(r)$ is constant, since any force on one charge is perfectly balanced by the opposite force on its counterpart. An inhomogeneous field, however, does not satisfy this condition. For small $\boldsymbol{d}$, we can approximate each component of $\boldsymbol{B}(r_1) - \boldsymbol{B}(r_2)$ as $\boldsymbol{\nabla} B_i \cdot \boldsymbol{d}$, where B_i is ith component of the field at the dipole's center. Defining $\boldsymbol{\mu} \equiv m\boldsymbol{d}$, we have

$$\boldsymbol{F} = (\boldsymbol{\mu} \cdot \boldsymbol{\nabla})\boldsymbol{B}. \tag{4.2}$$

It is useful to note that in one dimension this simplifies to

$$F = \pm\mu \frac{dB}{dr}, \tag{4.3}$$

where the only role of the orientation is to determine the sign of the force.

A slightly more rigorous starting point—and one that does not depend on unphysical objects—is the potential energy of an infinitesimal current loop in a magnetic

field. Taking $\boldsymbol{\mu} = I\boldsymbol{dA}$, where I is the current and $\boldsymbol{dA}$ is the loop area, we have potential energy:

$$U = -\boldsymbol{\mu} \cdot \boldsymbol{B}. \tag{4.4}$$

This yields

$$\boldsymbol{F} = \boldsymbol{\nabla}(\boldsymbol{\mu} \cdot \boldsymbol{B}), \tag{4.5}$$

which is identical to Equation 4.2, provided that $\boldsymbol{\nabla} \times \boldsymbol{B} = 0$. Equations 4.4 and 4.5 have exact parallels in the quantum picture.

4.2 Quantized angular momentum and adiabatic following

In a classical system, one expects $\boldsymbol{\mu}$ and $\boldsymbol{B}$ to be randomly oriented with respect to one another. This results in a continuous range of forces. A crucial discovery in the early years of quantum mechanics—made by Stern and Gerlach in 1922—was that the orientation of an atom's magnetic moment is instead quantized with respect to the field. Figure 4.1 reproduces a postcard showing this result, in which a collimated beam of silver atoms is split into two distinct parts by an inhomogeneous magnetic field. The implications of this discovery were far-reaching, but for our purposes they are rather simple: given an atom in a field, $\boldsymbol{\mu} \cdot \hat{\boldsymbol{B}}$ takes only discrete, fixed values. Since it is possible—using optical pumping or other methods—to artificially select the magnetic state of an atom, it is also possible to determine with excellent precision the force exerted by a magnetic field. More rigorously, we begin with the interaction Hamiltonian for the atom in the field:

$$H_{\text{int}} = -\boldsymbol{\mu} \cdot \boldsymbol{B}. \tag{4.6}$$

The semi-classical force is then

$$\boldsymbol{F} = \boldsymbol{\nabla}\langle \boldsymbol{\mu} \cdot \boldsymbol{B} \rangle = \langle \mu \rangle \boldsymbol{\nabla} B, \tag{4.7}$$

where B is the magnitude of the magnetic field and the fixed orientation of $\boldsymbol{\mu}$ is absorbed into the expectation value $\langle \mu \rangle$. Atoms whose magnetic moment is anti-aligned with the field such that $\langle \mu \rangle < 0$ are repelled by strong fields. These atoms

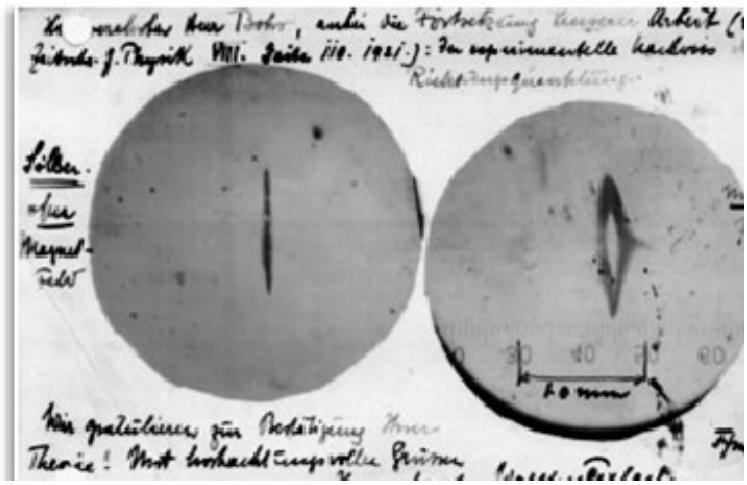

Figure 4.1: A postcard sent to Neils Bohr by Stern and Gerlach in 1922 [15]. The images show quantized magnetic deflection of silver atoms. On the left, we see the cross section of an undeflected beam. On the right, the same beam is split horizontally by an inhomogeneous magnetic field. The oval shape arises because the field gradient is not strong enough at the top and bottom of the beam to separate the atoms. Note that if an aperture were used to admit only the center of the beam, it would split cleanly into two spots. Presumably, the text at the bottom of the card says: "The Cubs are definitely going to win the World Series this year; they are overdue."

are described as low-field-seeking (LFS), and their behavior is the basis for the project described in this dissertation.

Perhaps even more surprising than the quantization of angular momentum is the principle of adiabatic following. Having chosen an angular momentum eigenstate—even one that is energetically unfavorable—an atom remains in this state indefinitely, provided the Hamiltonian is not disturbed too quickly. On the face of it this is quite absurd, since it means a high-energy LFS state will re-orient itself with a slowly rotating field to maintain its awkward, energetically unfavorable configuration. Further examination reveals that there is no mechanism for the atom to relax. The torque exerted by the field causes the total angular momentum vector to precess around the quantization axis, but it leaves the projection along the field direction fixed. If this field direction changes only imperceptibly over the period of one precession, the atom continuously re-orients itself and remains in the same instantaneous energy eigenstate. If the field direction exceeds this speed limit, spin flips may occur.

Explicitly, the condition for adiabatic following is that the precession rate of the

total angular momentum—known as the Larmor frequency—must be much larger than the rate of change of the field direction:

$$\frac{\mu B}{\hbar} \gg \left| \frac{d}{dt} \left(\frac{\boldsymbol{B}}{B} \right) \right|. \tag{4.8}$$

Note that for small fields, adiabatic following becomes difficult to guarantee. We will return to this potential pitfall in Chapter 7. For the large fields inside our hexapole, the condition for adiabatic following is easily satisfied.

4.3 Angular momentum in atoms

From Equation 4.7, we know that the main task remaining to us is to calculate the atomic magnetic moment. This arises from the combined orbital and spin angular momenta of its constituent particles. In order to keep things simple and relevant, we will focus this discussion on metastable neon. As described in Chapter 3, Ne^* is characterized by the electron configuration $(1s)^2(2s)^2(2p)^5(3s)$, which features two unpaired electrons. The p electron contributes an orbital angular momentum corresponding to $L = 1$, where L is the quantum number associated with the operator $\boldsymbol{L}^2$ according to the eigenvalue equation

$$\boldsymbol{L}^2|L\rangle = \hbar^2 L(L+1)|L\rangle. \tag{4.9}$$

The two electron spins ($s_i = 1/2$) contribute a total spin of either $S = 1$ (triplet) or $S = 0$ (singlet), where $\hbar^2 S(S+1)$ is the eigenvalue of the operator $\boldsymbol{S}^2$. For an unperturbed atom, spin-orbit coupling mixes eigenstates of $\boldsymbol{L}$ and $\boldsymbol{S}$, meaning that the projections of these momenta onto a quantization axis are not conserved. Put a different way, the quantum numbers m_L and m_S, associated with operators $\boldsymbol{L}_Z$ and $\boldsymbol{S}_Z$, are not good quantum numbers. This is a problem if we wish to calculate the magnetic moment of the atom. Fortunately, the projection of the total angular momentum, $\boldsymbol{J} = \boldsymbol{L} + \boldsymbol{S}$, is conserved. It obeys the following eigenvalue equations:

$$\boldsymbol{J}^2|J, m_J\rangle = \hbar^2 J(J+1)|J, m_J\rangle, \tag{4.10}$$

and

$$J_z|J, m_J\rangle = \hbar m_J|J, m_J\rangle. \tag{4.11}$$

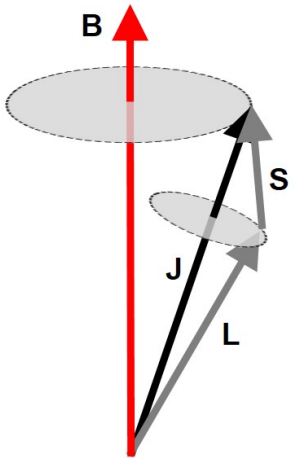

Figure 4.2: A diagram showing the angular momentum structure of an atom in the Zeeman regime. Because $\boldsymbol{S}$ and $\boldsymbol{L}$ are mixed by spin-orbit coupling, their projections along $\boldsymbol{B}$ are not conserved. Fortunately, $\boldsymbol{J} = \boldsymbol{L} + \boldsymbol{S}$ does precess around $\boldsymbol{B}$, so its z-component is fixed and m_J is a good quantum number.

The total angular momentum quantum number, J, can take integer values between $|L - S|$ and $L + S$. For a given J, there are $2J + 1$ sublevels corresponding to $m_J \in [-J, -J + 1, ...J - 1, J]$. These m_J states are degenerate in the absence of an external field, but they separate when a field is applied.

4.4 Zeeman and Paschen-Back effects

The Hamiltonian describing a magnetic atom in a field is nearly identical to the classical energy of an infinitesimal loop. The only difference between Equations 4.4 and 4.6 is that in the latter case, $\boldsymbol{\mu}$ is an operator denoting the atomic magnetic moment. Explicitly:

$$\boldsymbol{\mu} = -\frac{\mu_B}{\hbar}\left(g_L \boldsymbol{L} + g_S \boldsymbol{S}\right), \tag{4.12}$$

where $g_L = 1$ and $g_S \approx 2$ are the respective g-factors for orbital and spin angular momentum and μ_B is the Bohr magneton. The introduction of an external field constitutes a form of measurement, causing the atom to adopt an eigenstate of the full Hamiltonian. In this case, that means we can take z as the quantization axis and write $\boldsymbol{B}$ as $B\hat{\boldsymbol{z}}$. The problem of calculating the energy shift of a magnetic atom

therefore becomes that of determining the expectation value of $\langle \hat{\boldsymbol{z}} \cdot \boldsymbol{\mu} \rangle$:

$$\langle H_{\text{int}} \rangle = \left\langle \frac{\mu_B B}{\hbar} \hat{\boldsymbol{z}} \cdot (g_L \boldsymbol{L} + g_S \boldsymbol{S}) \right\rangle. \tag{4.13}$$

Energy level splitting due to the presence of a small external field is referred to as the Zeeman effect. In this regime, the spin-orbit coupling discussion above remains valid. J and m_J are good quantum numbers, while m_L and m_S are not. Heuristically, this means that the spin and orbital angular momenta both precess around $\boldsymbol{J}$, instead of maintaining a fixed projection along $\hat{\boldsymbol{z}}$ (Figure 4.2). Introducing a field causes $\boldsymbol{J}$ to precess around $\hat{\boldsymbol{z}}$, but J_z remains fixed. In order to calculate $\langle \hat{\boldsymbol{z}} \cdot \boldsymbol{\mu} \rangle$, we assume that the precession of $\boldsymbol{L}$ and $\boldsymbol{S}$ averages out, yielding:

$$\bar{\boldsymbol{L}} = \frac{\boldsymbol{L} \cdot \boldsymbol{J}}{\boldsymbol{J}^2} \boldsymbol{J} \tag{4.14}$$

and

$$\bar{\boldsymbol{S}} = \frac{\boldsymbol{S} \cdot \boldsymbol{J}}{\boldsymbol{J}^2} \boldsymbol{J}. \tag{4.15}$$

The useful identities:

$$\boldsymbol{S} \cdot \boldsymbol{J} = \frac{\boldsymbol{J}^2 + \boldsymbol{S}^2 - \boldsymbol{L}^2}{2} \tag{4.16}$$

and

$$\boldsymbol{L} \cdot \boldsymbol{J} = \frac{\boldsymbol{J}^2 + \boldsymbol{L}^2 - \boldsymbol{S}^2}{2} \tag{4.17}$$

allow us to write

$$H_{\text{int}} \approx \frac{\mu_B B}{\hbar} \hat{\boldsymbol{z}} \cdot \boldsymbol{J} \left(g_L \frac{\boldsymbol{J}^2 + \boldsymbol{S}^2 - \boldsymbol{L}^2}{2\boldsymbol{J}^2} + g_S \frac{\boldsymbol{J}^2 + \boldsymbol{L}^2 - \boldsymbol{S}^2}{2\boldsymbol{J}^2} \right) \tag{4.18}$$

Taking the expectation value, we obtain

$$\begin{aligned} \langle H_{\text{int}} \rangle \approx \ & \mu_B B m_J \left(g_L \frac{J(J+1) - S(S+1) + L(L+1)}{2J(J+1)} \right. \\ & \left. + g_S \frac{J(J+1) + S(S+1) - L(L+1)}{2J(J+1)} \right) \\ & \equiv \mu_B m_J g_J B, \end{aligned} \tag{4.19}$$

where g_J is referred to as the Landé g-factor. Equation 4.19 is shockingly simple, considering how many moving parts we just took into account. Figure 4.3 shows the Zeeman splitting of the five $^3P_2$ states as a function of an external magnetic field.

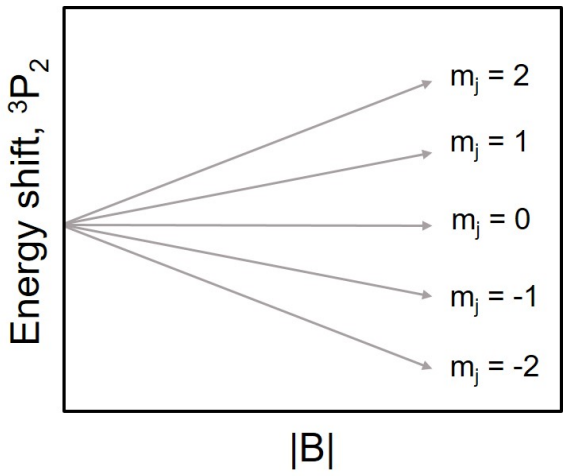

Figure 4.3: Magnetic splitting of the magnetic sublevels as a function of B for a $^3P_2$ atom in the Zeeman regime.

For large fields, the coupling of $\boldsymbol{L}$ and $\boldsymbol{S}$ to $\boldsymbol{B}$ is strong enough that m_L and m_S become good quantum numbers. In this regime, the state splitting is referred to as the Paschen-Back effect (Figure 4.4). Calculating $\langle H_{\text{int}} \rangle$ in this situation is actually quite simple:

$$\langle H_{\text{int}} \rangle \approx \mu_B B \left(m_L + 2m_S \right). \tag{4.20}$$

Less simple is mapping the various energy levels as they transition between the Zeeman and the Paschen-Back regimes, since in many cases this involves energy eigenstates with varying slopes. Fortunately, maximal states like $m_J = \pm J$ involve the largest possible projections of $\boldsymbol{S}$ and $\boldsymbol{L}$, and the slope of $\langle H_{\text{int}} \rangle$ as a function of B is the same in both regimes. We will therefore move along, leaving the task of diagonalizing the entire intermediate-field Hamiltonian to any poor saps trying to build a magnetic lens for $m_J = 1$ Ne* atoms.

Returning to the concrete details of our magnetic focusing experiment, we use optical pumping to form a polarized beam of 3^3P_2 Ne* in the $m_J = 2$ LFS state. The Landé g-factor for these atoms is approximately 3/2, yielding a force of

$$F_{\text{beam}} = -3\mu_B \boldsymbol{\nabla} B. \tag{4.21}$$

Thanks to adiabatic following, we can effectively treat this as a classical force for the remainder of our calculations.

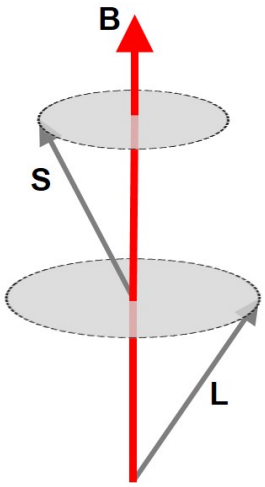

Figure 4.4: Angular momentum diagram in the Paschen-Back regime. For strong fields, spin-orbit coupling is overpowered and $\boldsymbol{S}$ and $\boldsymbol{L}$ precess directly around $\boldsymbol{B}$. This dramatically simplifies the calculation of $\langle H_{\text{int}} \rangle$, but does not change the result for maximal states.

Chapter Five: Magnetic mirror

We now have all the theoretical tools we need to begin discussing magneto-optical elements for atom beams. The primary objective—an aberration-corrected electromagnetic lens—is discussed in Chapters 7-9. Along the path to this goal, however, we built and characterized a magnetic mirror for fast atoms. Though the current incarnation of the focusing project does not use this mirror, it performed well enough to warrant a publication in its own right. Most of the material in this Chapter appeared as a Note in the Journal of Chemical Physics in September, 2013[1]. Because the space restrictions in the current context are rather less stringent, certain parts of the discussion have been permitted to expand.

5.1 Introduction

Neutral atom beams have broad applicability to atomic and molecular science, particularly in the study of nanofabrication [11, 42, 9, 43], cold chemistry [44, 5], and atom-surface interactions [45, 46, 47]. For beams of paramagnetic atoms, an inhomogeneous magnetic field can be used for redirection and spin separation [48]. This technique dates back to the Stern-Gerlach experiment and continues to be employed in several recent demonstrations of magnetic lenses and mirrors [1, 49, 50, 51, 52, 53, 10, 33, 54]. Because many experiments involve high velocity beams with a narrow energy distribution [5, 55, 56, 57, 58], manipulation techniques for these particular cases merit further development. In this Chapter, we report the use of a planar Halbach array [59] to either deflect or to specularly reflect a high-velocity, nearly monoenergetic beam of neutral atoms in a spin-sensitive manner. We report our experimental results for metastable neon (Ne^*) and metastable helium (He^*) atom beams generated with a pulsed supersonic nozzle.

[1] J. Gardner, R. Castillo-Garza, and M. G. Raizen, "Manipulation of supersonic atomic beams with static magnetic fields," *Journal of Chemical Physics*, vol. 139, p. 096103, 2013. J. Gardner's contributions to this work included large portions of the experimental design, data analysis, and manuscript writing.

5.2 Halbach array

It is useful to begin by describing the qualities we are looking for in a mirror. As in photo-optics, an atom reflection consists of a scattering event in which the angle of incidence and the angle of departure are the same. In other words, the momentum parallel to the surface is conserved, while that perpendicular to the surface is perfectly reversed. Two metrics for success require attention: efficiency and specularity. Efficiency refers to the fraction of atoms that the mirror successfully reflects. In direct scattering reflections—i.e., from a crystalline surface—efficiency can be rather low [60]. In reflections based on conservative, longer-range electromagnetic forces, however, the gentler interaction allows efficiency to approach 100%. Specular reflection contrasts with diffuse reflection, in which atoms rebound at unpredictable angles from the mirror surface. On a microscopic level, this arises because the atomic scattering events take place with respect to a local "surface normal" that does not match the macroscopic mirror plane. In layman's terms: diffuse reflection occurs because the reflecting surface is bumpy. A good atom mirror reflects all incoming atoms with the same incident angle into exactly the same departure angle, conserving critical beam properties like temperature and collimation. For a true specular reflection, atoms in a beam must encounter force only in the direction of the macroscopic surface-normal vector. As discussed in Chapter 4, the interaction energy between an atom and a magnetic field (B) is $m_J g_J \mu_B B$. In an inhomogeneous field, low-field seeking (LFS) atoms experience a force parallel to $\boldsymbol{\nabla} B$, away from a field maximum. Taking the desired performance metrics into account, we therefore set out to create a magnetic structure with a strong field gradient pointing predominantly in a single direction.

A Halbach array offers precisely such an object (Figures 5.1, 5.2). The array constructed for this experiment consists of 100 commercial Neodymium-Iron-Boron magnets (1 x 1/8 x 1/8, Grade N42, remanence 1.3 T, magnetized perpendicular to the long axis) assembled side-by-side such that each element's magnetization rotates counterclockwise by 90° with respect to its left-hand neighbor. Constructive superposition yields a strong ($B_{max} \approx 1$ T), exponentially decaying ($\nabla B \approx 300$ T/m) magnetic field of rotating direction but constant magnitude along the top of the array. We have verified that atoms from the supersonic nozzle remain in the adiabatic regime while following this changing field direction. Hall probe measurements of the assembled array agree well with a finite-element model of the field. The mir-

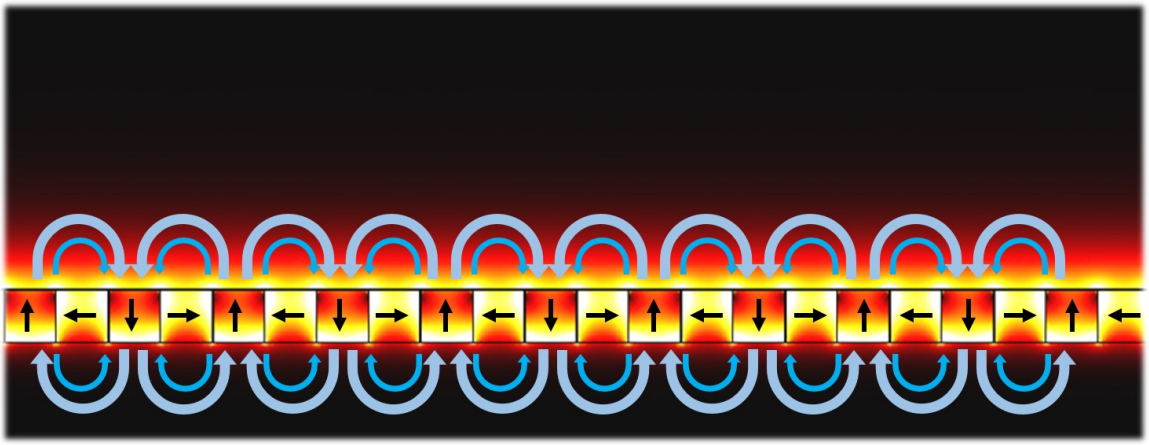

Figure 5.1: A diagram of a Halbach array. Blue arrows represent magnetic field lines. The outer arrows are from the vertical elements of the array, while the deeper-blue inner arrows represent the field lines from the sideways-pointing elements. On the top of the Halbach array, these arrows point in the same direction and create a large field. On the underside of the array, the field lines cancel and almost no field remains. The diagram and arrows are overlaid with color plot results from a finite element model of the field strength for a typical array.

ror is mounted to a stage machined from stainless steel and aluminum, which offers in-vacuum adjustment of both position and angle. The mirror and the stage are mounted to a 10" CF vacuum flange with two linear translation feed-throughs which control the two degrees of freedom (Figure 5.2).

5.3 Experimental setup

We generate a fast beam of metastable atoms with a velocity dispersion of $\Delta v/v \approx 0.02$ using an Even-Lavie pulsed supersonic nozzle in conjunction with an electron discharge source. The theoretical basis for this device is covered in Chapter 2. Details of the Even-Lavie valve specifically are discussed in Chapter 7. When the nozzle is at room temperature, helium atoms exit with a velocity of 1700-1800 m/s. Excited to the 2^3S_1 metastable state, He* has one LFS sublevel ($m_J = 1$). Ne* atoms are produced with a velocity of 800-900 m/s and, in the 3^3P_2 state, have two LFS sublevels ($m_J = 1,2$). After passing through a skimmer, the beam is collimated with a 300 μm circular aperture, 0.88 m from the nozzle, after which it propagates towards the

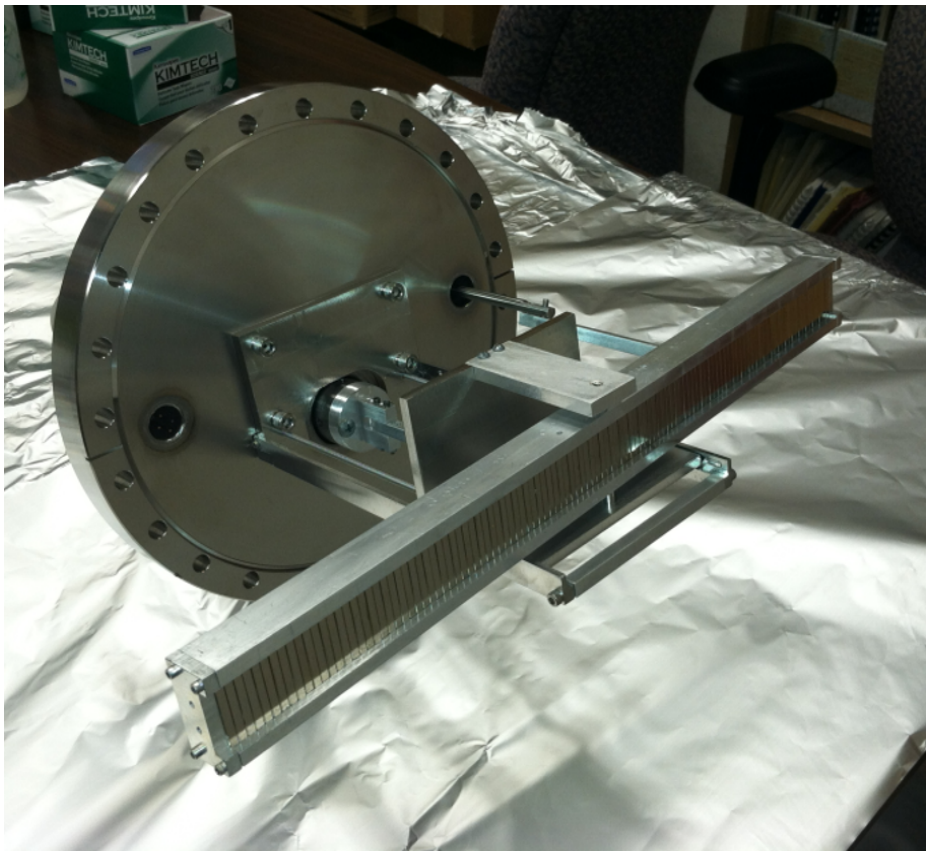

Figure 5.2: A photograph of the magnetic mirror used in this experiment. Two linear translators connected to the mirror stage allow us to adjust both position and angle while the mirror is in vacuum.

Halbach array.

We collect data for two distinct operating modes: deflective and reflective (Figure 5.3). In the deflective case, the beam enters the field region from the side and travels along the array surface (Figure 5.3(a)). Atoms in the beam deflect with angles that depend on their magnetic moments. In reflection, the beam approaches the array at an angle from above (Figure 5.3(b)). Depending on magnetic moment, atoms then either bounce off the array field with the same angle or collide with its surface and relax to the ground state. Once the beam has interacted with the array in one of these two modes, we observe it using a microchannel plate detector (MCP) in conjunction with a phosphor screen (Figure 5.4). Details of this detection system are discussed more completely in Chapter 7.

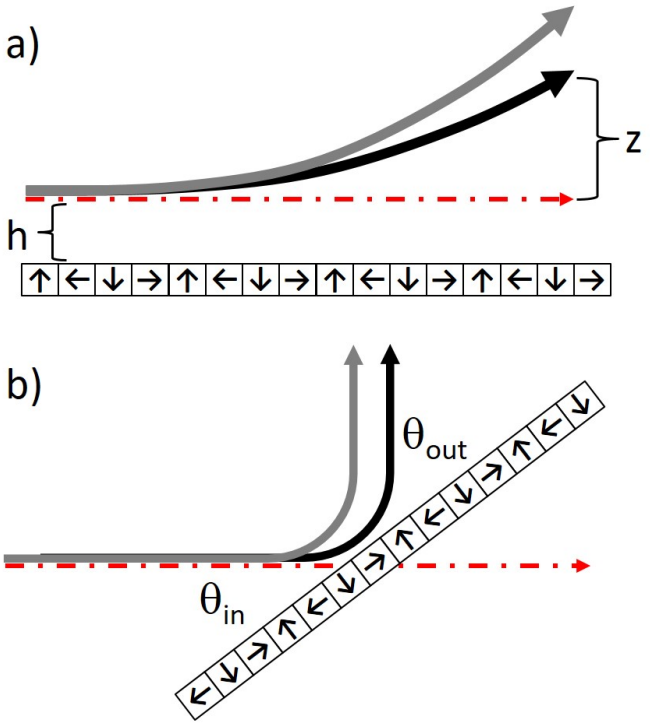

Figure 5.3: Two complementary modes of operation for our planar Halbach array. In (a), atoms enter the mirror field from the left side and deflect up. This converts some of their forward momentum into vertical momentum. The angle at which the atoms leave the field depends on their mass-to-magnetic-moment ratio. In (b), atoms enter the field region from "above," and experience force exclusively in the normal direction. Their parallel momentum is unchanged, while their vertical momentum is reflected. The departure angle is equal to the angle of incidence. In order for this reflection scenario to take place, the angle must be steep enough that the atoms do not interact with the edges of the array.

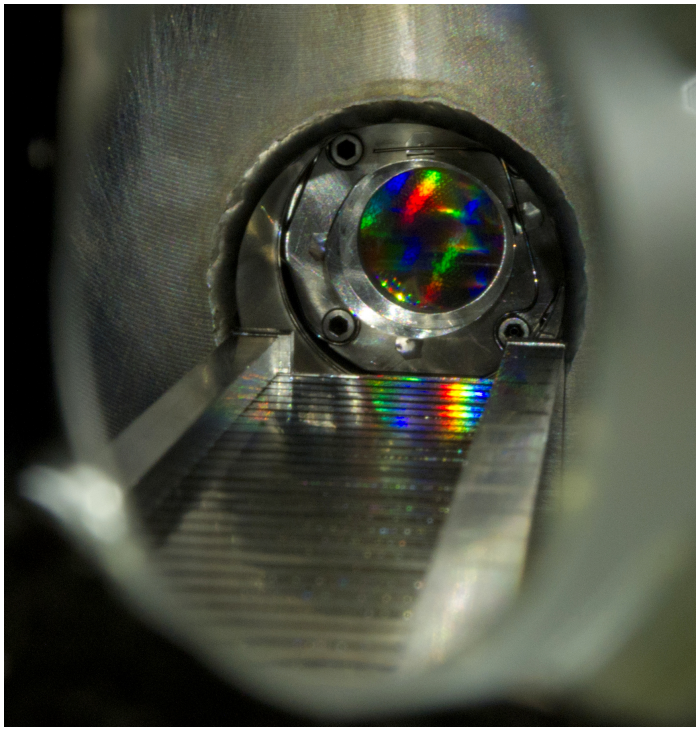

Figure 5.4: A photograph of the Halbach array next to the MCP.

5.4 Stern-Gerlach deflection

In the deflective mode, atoms enter the high-field region from the side, traveling parallel to the surface of the mirror (Incident angle $\theta_{\text{in}} = 0°$, impact parameter h; see Figure 5.3(a)). This involves a momentary longitudinal force, which slows them down and converts a portion of their kinetic energy into magnetic potential energy. While they are over the array, the atoms experience a force that is normal to the mirror surface. This results in a vertical acceleration whose magnitude depends on the atoms' mass-to-magnetic-moment ratio. The atoms therefore split into distinct beams, each consisting of a single magnetic species and leaving the high-field region at a specific angle. We observe these beams and measure the deflection of the LFS atoms with respect to the undeflected $m_J = 0$ spot. The results for He* and for both LFS species of Ne* are reported in Figure 5.5. We model this system using a Runge-Kutta ODE integrator and realistic assumptions for beam speed and temperature. The observed deflections agree well with our numerical simulations of particle trajectories. It is interesting to note that we see a mild collimating effect on the beam in the surface-

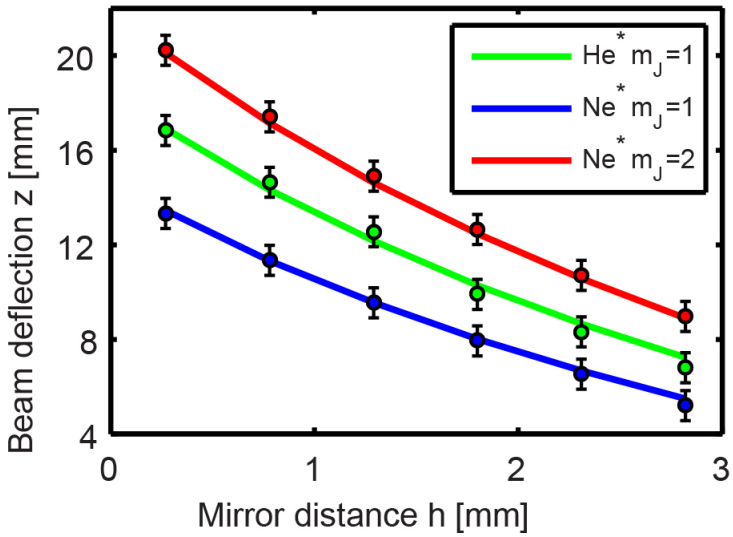

Figure 5.5: Experimental and theoretical deflection of 3^3P_2 Ne* and 2^3S_1 He* for a range of impact parameters. Atoms enter the field region moving approximately parallel to the array. They deflect according to their magnetic moment and are detected by the MCP. As one might expect, a smaller impact parameter—associated with the particle passing closer to the array surface, where the field is strongest—produces a larger deflection. Unsurprisingly, so does a smaller mass-to-magnetic-moment ratio. Simulations (solid lines) are performed in Matlab using respective beam velocities of 800 and 1700 m/s. Note added during dissertation: we had no good way to measure h or θ_{in}, so we used them as fitting parameters within reasonable bounds. In retrospect, this led to suspiciously good agreement.

normal dimension, indicating that the array has some of the properties of a cylindrical lens. This phenomenon is related to the deflective focusing in [50], and may be further explored in future work.

5.5 Magnetic mirror

In order for a reflection to occur, the atoms must encounter force exclusively in the surface-normal direction. This requires that they approach at a steep enough angle to avoid any interaction with the front and back edges of the array (Figure 5.3(b)). If this condition is met, the portion of their kinetic energy that is due to motion towards the mirror is absorbed as magnetic potential energy. Assuming the

maximum magnetic potential is large enough, this energy is then completely returned to the atoms, sending them away with exactly the same angle. Figure 5.6 shows the outgoing angles of Ne* atoms for a range of θ_{in}. For shallow incidence, the edge effects of the array are important and cause deflective behavior. As the incident angle increases, the atoms perceive the mirror as semi-infinite, and θ_{out} asymptotically joins θ_{in}. In this regime, the LFS atoms experience a repulsive force that reverses their perpendicular velocity ($v_\perp$) but leaves parallel velocity ($v_\parallel$) unchanged. In contrast to the deflective case, the departure angle in a reflection does not depend on magnetic moment. While a narrow, perfectly collimated beam would be split into two parallel parts, the mirror does not efficiently spin-separate a divergent beam. This does not mean, however, that the mirror is not spin sensitive: beam polarization can take place when only one magnetic species has a large enough magnetic moment to avoid colliding with the array.

Around $\theta_{\text{in}} = 2°$, the perpendicular kinetic energy $m{v_\perp}^2/2$ approaches the maximum magnetic potential of the $m_J = 1$ atoms, which begin to crash into the array. The outgoing beam for $\theta_{\text{in}} \geq 2°$ is therefore predominantly spin-polarized, with $m_J = 2$. Intensity profiles in Figure 5.7 show the progression from $\theta_{\text{in}} = 1.5°$, where there are two distinct spots, to 2.5°, where one spot has nearly vanished. Note that imperfect collimation and velocity dispersion broaden the attenuation of the $m_J = 1$ particles, reducing the efficiency of beam polarization near the cutoff angle. Though it is outside the spatial range of our detector, we expect the $m_J = 2$ beam to be cut off around 3°.

5.6 Phase space

The magnetic mirror does not change shape in phase space, but it does change position. Figure 5.8 shows this transformation in two 2D planes of the 6D phase space manifold. The images show again the way a mirror reverses perpendicular momentum without affecting the horizontal motion of the beam. Unlike the other cases we discuss, there is no redistribution of ρ between position- and momentum-space.

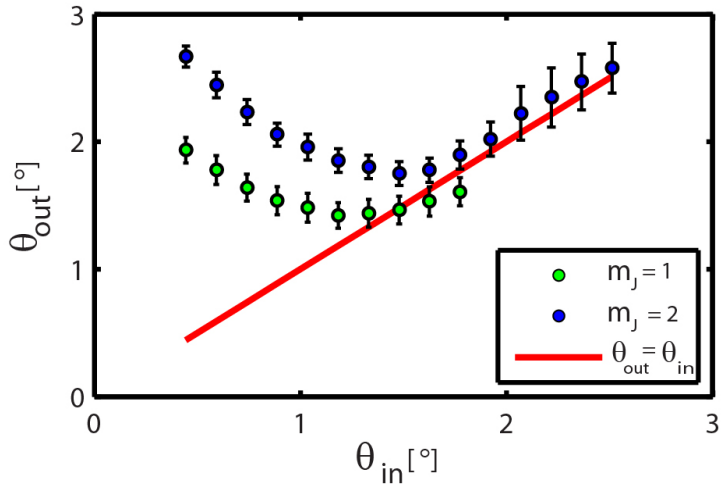

Figure 5.6: Outgoing angle as a function of incidence angle for Ne*. The red line represents ideal specular reflection (θ_{out}=θ_{in}). For low angles, atoms enter the field from the side and are partially deflected (see text), leading to a θ_{out} that depends on m_J. For larger angles, the atoms perceive the mirror as semi-infinite and asymptotically approach specular reflection. Around 2°, the $m_J = 1$ atoms no longer interact strongly enough to reflect and crash into the array. The reflected beam above this critical angle is spin polarized. Angles are calculated by combining experimental deflection distances with geometrical information from simulations. Simulation parameters are consistent with those used in Figure 4.1 and predicted deflections match well with observation. Uncertainty values reflect possible error in the calibration process and the disagreement between simulation and experiment.

5.7 Conclusion

In summary, we demonstrate the use of a planar Halbach array to either deflect or to specularly reflect a fast, nearly monochromatic beam of paramagnetic atoms. As a tool for beam manipulation and spin selection, this technique applies to any atom or molecule with an accessible magnetic state. To our knowledge, this is the first demonstration of specular reflection of a fast supersonic beam. While this device once played an important role in the magnetic focusing project, it has since been retired from the main beamline. Nevertheless, the principles from this research continue to serve: we use a short section of Halbach array in the deflective mode to monitor the efficiency of our optical pumping.

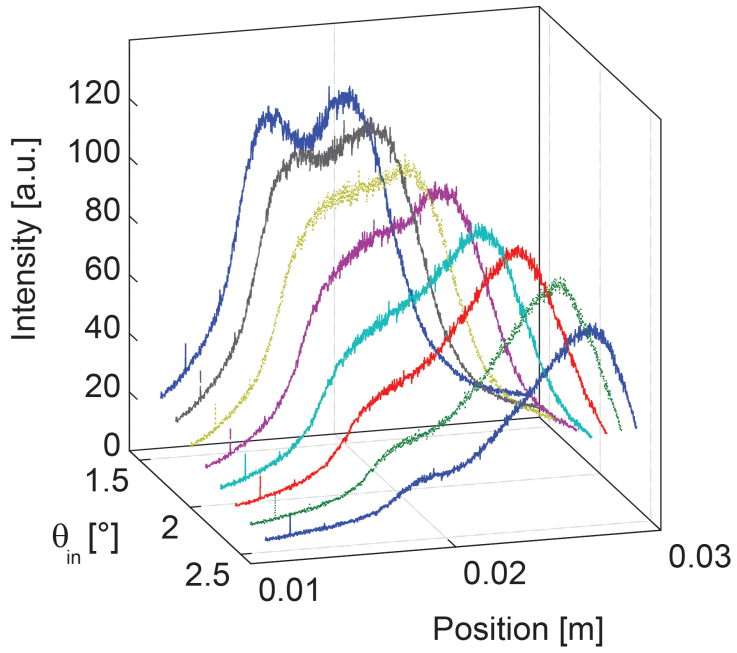

Figure 5.7: Intensity profiles for Ne* at a range of incidence angles, θ_{in}. These are flux averages as a function of distance from the mirror surface taken from the CCD image of the MCP. At 1.5°, both LFS species are present and distinguishable. As the mirror angle increases towards 2.5°, the $m_J = 1$ atoms begin to collide with the array and drop out of the beam. Between 2.5° and 3°, the reflected beam is spin-polarized.

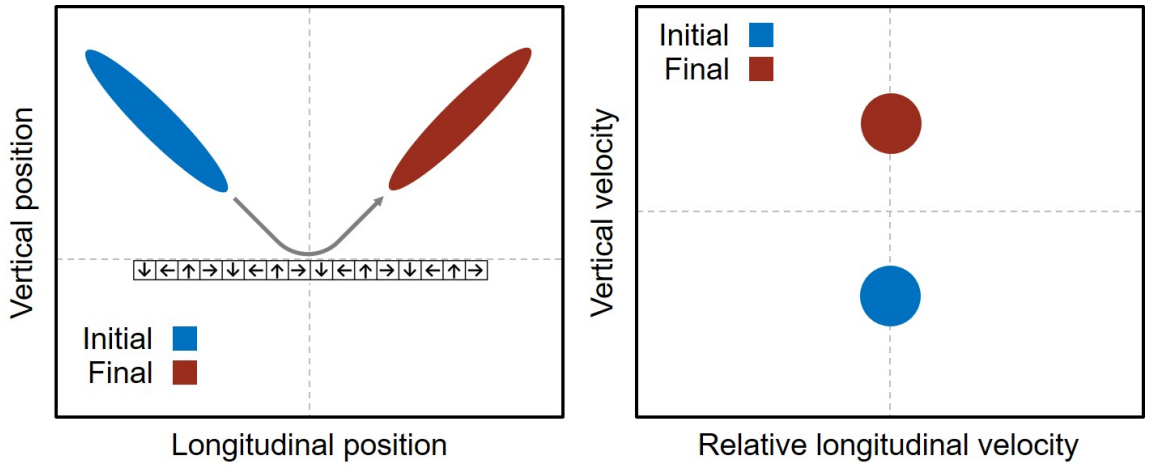

Figure 5.8: Two planes of the phase space manifold showing the transformation effected by the magnetic mirror. It is interesting to note the traditional reciprocal relationship between position and momentum, since the atomic beams are technically lines in position space and spots in momentum space.

Chapter Six: Lens design

We wish to construct an electromagnetic structure that acts on a beam of atoms the same way a refractive lens acts on a beam of light. To accomplish this, our lens must exert a force on atoms in the beam that depends on their radial distance from the beam axis. The deflection of paramagnetic atoms in an inhomogeneous magnetic field is based on the same principle as the Stern-Gerlach experiment, as described in Chapters 4 and 5. As before, the force on a given atom is given by

$$\boldsymbol{F} = \langle \mu \rangle \boldsymbol{\nabla} B = -\mu_B g_j m_J \boldsymbol{\nabla} B. \tag{6.1}$$

For LFS atoms with $m_J > 0$, F is always in the direction of smaller fields. For metastable neon in the $m_J = 2$ $3^3\mathrm{P}_2$ state,

$$\boldsymbol{F} = -3\mu_B \boldsymbol{\nabla} B. \tag{6.2}$$

Through optical pumping, it is possible to polarize a beam such that all atoms entering the lens have the same m_J. The problem of focusing therefore simplifies to that of constructing a magnetic field whose gradient exhibits the desired force profile.

6.1 Lens basics

It is worth reviewing the basic properties of the convex lens. In the simplest case, a perfectly collimated beam—or, equivalently, light from a point source infinitely far away—enters the lens and is focused to a single spot at focal length f (Figure 6.1). Classically, the size of this spot is zero. In real terms, the focused beam forms an Airy disk whose zero-order spot has a half-width given by:

$$\delta = 1.22 \, \frac{\lambda f}{D}, \tag{6.3}$$

where λ is the wavelength of the particle and D is the diameter of the lens aperture (Figure 6.2). The ratio f/D is called the lens's "f-number," or speed. Lenses with low f-number are called fast because of the high flux that passes through their relatively large apertures. Fast optical lenses can approach f/1, yielding a diffraction limit on

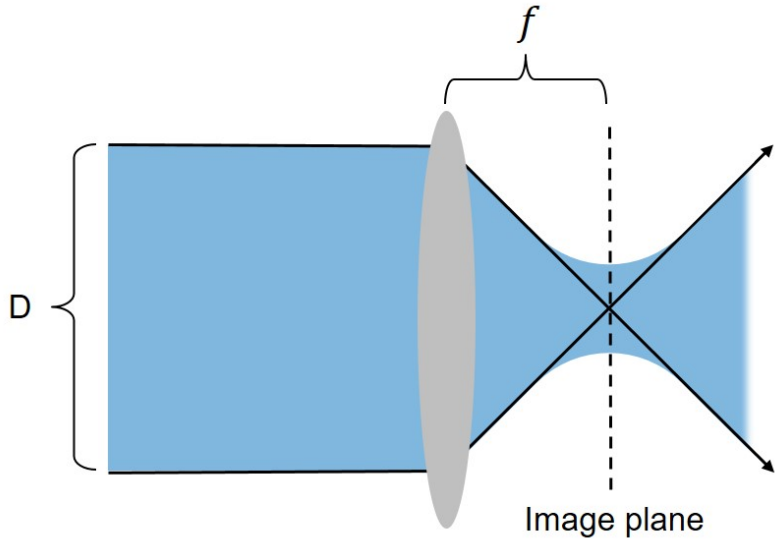

Figure 6.1: A diagram of focusing for the case of a perfectly collimated beam. While ray optics would suggest an infinitely small spot, diffraction causes a finite waist instead. The diffraction limit improves with lower f-number.

the order of 500 nm. Atom lenses are quite impressive if they exceed f/100. Due to sub-angstrom wavelengths, however, their diffraction limits remain on the order of a few nm. Along with diffraction, an important adversary in optics is aberration. This broad term refers to the failure of a lens to properly focus all components in a beam. Spherical aberration covers problems with the lens itself; for example, in which rays at certain radii are deflected by the wrong angle. Chromatic aberration occurs when specific components of the beam—photons or atoms of different wavelength, for example—interact differently with the lens. Figure 6.3 depicts an instance of chromatic aberration in which a portion of the collimated beam (represented by the shaded regions) is focused to the incorrect point. In an atom lens, this blue shaded beam might correspond to anomalously fast atoms. The non-aberrant beam (shown as black rays) focuses to the correct plane. If a detector were placed here, the aberrant beam would appear as a circle instead of a point. In photography, this is called the "circle of confusion." Its diameter is given by:

$$C = \frac{\delta D}{f + \delta}, \tag{6.4}$$

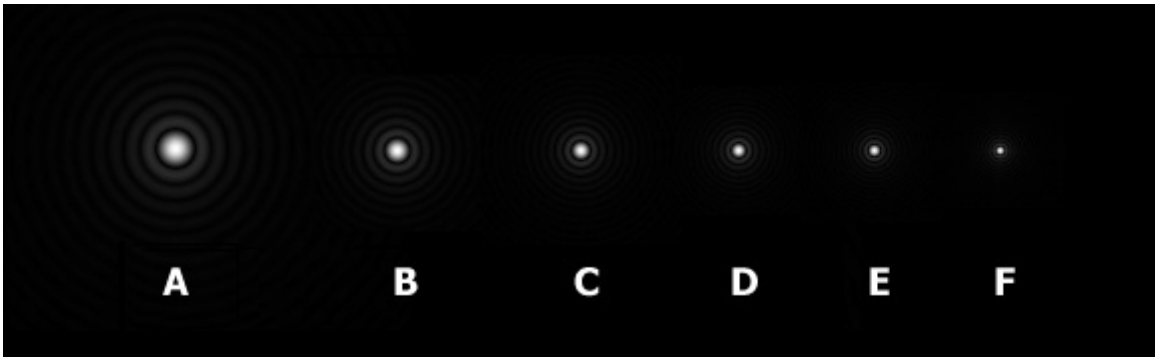

Figure 6.2: Simulated telescope images for lens apertures that increase from 10 cm (A) to 40 cm (F) [61]. For a distant object, a telescope does almost exactly what is shown in Figure 6.1. As the telescope's aperture increases, the Airy disk shrinks, and resolution improves.

where δ is the focal distance error of the aberrant particles. Similar geometric relationships apply for spherical aberration and for simple focusing errors. In all cases, the size of the circle of confusion is proportional to the lens aperture, as illustrated by the two aberrant beams (D and D') in the figure. This is the geometric reason that photographs taken with fast (wide aperture, low f-number) lenses often feature "bokeh," or blurry foreground and background structure. In the limit of small aperture—i.e., a pinhole lens—the circle of confusion becomes so small that all rays are in focus at all planes (ignoring diffraction). This leads to an unfortunate competition. We want to maximize flux and minimize diffraction, which suggests building as fast a lens as possible. Unfortunately, any aberrations in our system will be more damaging in a fast lens (Table 6.1). This is the essential conundrum: to build a lens as fast a lens as our aberrations will allow. We will return to this concept later on, when we push the theoretical limits of our atom lens into the nm regime.

Table 6.1: Short grid to show the competing interests in lens design. While fast lenses are important for maximizing flux and avoiding diffraction, they also exacerbate the negative effects of aberrations.

Property :	Diffraction	Aberration	Flux
Optimal f/D:	$\downarrow$	$\uparrow$	$\downarrow$

A perfectly collimated beam is neither realistic nor particularly useful. On the contrary, most lenses are used to reproduce the two-dimensional images of objects at

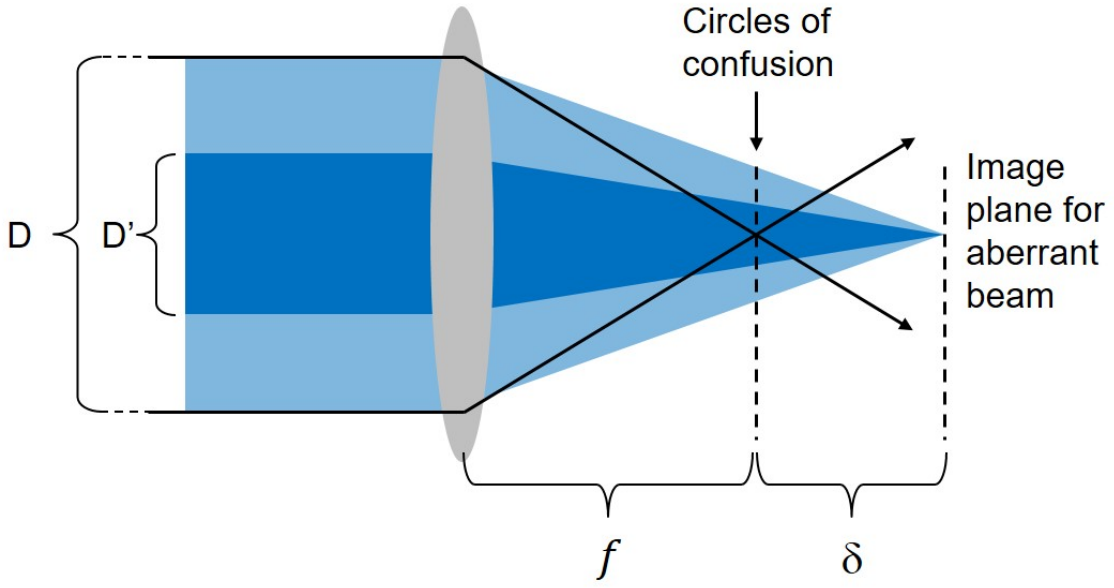

Figure 6.3: A geometrical explanation of "circles of confusion." We ignore diffraction for the moment and just look at ray optics for a perfectly collimated beam. Any components of the beam that are out-of-focus will form a circle instead of a point at the image plane. This results in blurriness and decreased resolution. The effect can be mitigated by using a smaller lens aperture, as shown by the darker shaded beam.

a finite distance. This situation is depicted in Figure 6.4. An object in this context consists of an extended surface, each point of which acts as a perfectly divergent source. Rays passing through a lens at distance $d_o > f$ form an image at d_i according to the thin lens equation:

$$\frac{1}{d_o} + \frac{1}{d_i} = \frac{1}{f}. \tag{6.5}$$

The image size s_i is related to the object size s_o by:

$$M \equiv \frac{s_i}{s_o} = \frac{d_i}{d_o}, \tag{6.6}$$

where M is the called the magnification factor.

If we want to create small spots and patterns from a larger transmission mask, we will need $d_i \ll d_o$. A powerful lens (small f) allows us to achieve a short image distance. In order to accommodate a large object distance, with its inevitable reduction in flux, we also want a relatively large lens aperture. Taken together, these requirements recommend building as fast a lens as possible. However, we will be restricted

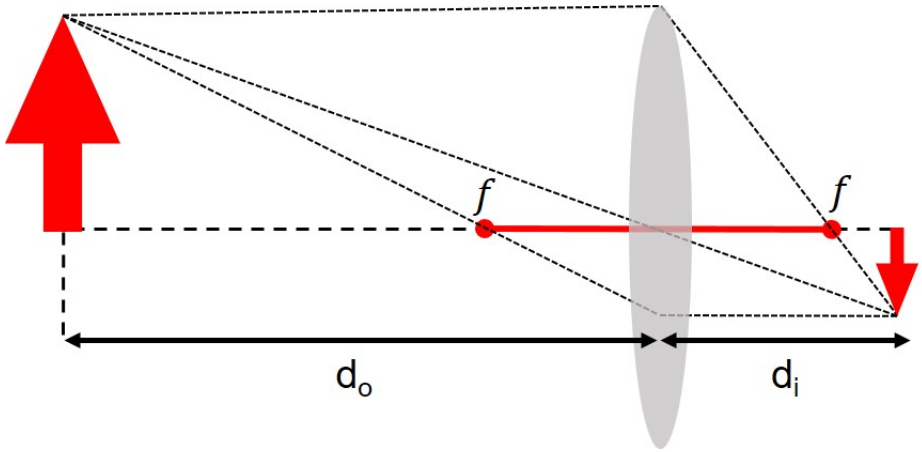

Figure 6.4: Simple illustration of ray optics. An object at d_o, outside of the focal point f, is imaged to d_i according to Equation 6.5.

in this effort by any focusing errors that arise, since aberrations are significantly more damaging when f/D is small.

6.2 Focusing an atomic disk

For the simple case of a single collimated disk of atoms inside a lens, the goal is to find a focusing field that sends each atom in the disk to the same focal point. Figure 6.5 depicts the situation for a perfectly collimated beam of atoms with uniform initial velocity $\boldsymbol{v}_{\parallel}$. For the purposes of this discussion, we assume that we are smart enough to build a lens that exerts a purely radial force on each atom, pushing it towards the beam axis. The lens pulse, of duration τ, imparts a perpendicular velocity $\boldsymbol{v}_{\perp} = \boldsymbol{F}\tau/m$ to each atom, where m is the atomic mass. Using the results above:

$$\boldsymbol{v}_{\perp} = \frac{-3\mu_B \tau \boldsymbol{\nabla} B}{m}. \tag{6.7}$$

Defining the focal length f to be the longitudinal position at which an atom crosses the axis, we have the simple relation:

$$\frac{f}{v_{\parallel}} = \frac{\rho}{v_{\perp}}, \tag{6.8}$$

where ρ is the radial position of the incoming atom. If we wish for all atoms to cross the axis at the same point, it is immediately clear that $v_{\perp} \propto \rho$. This leads to the

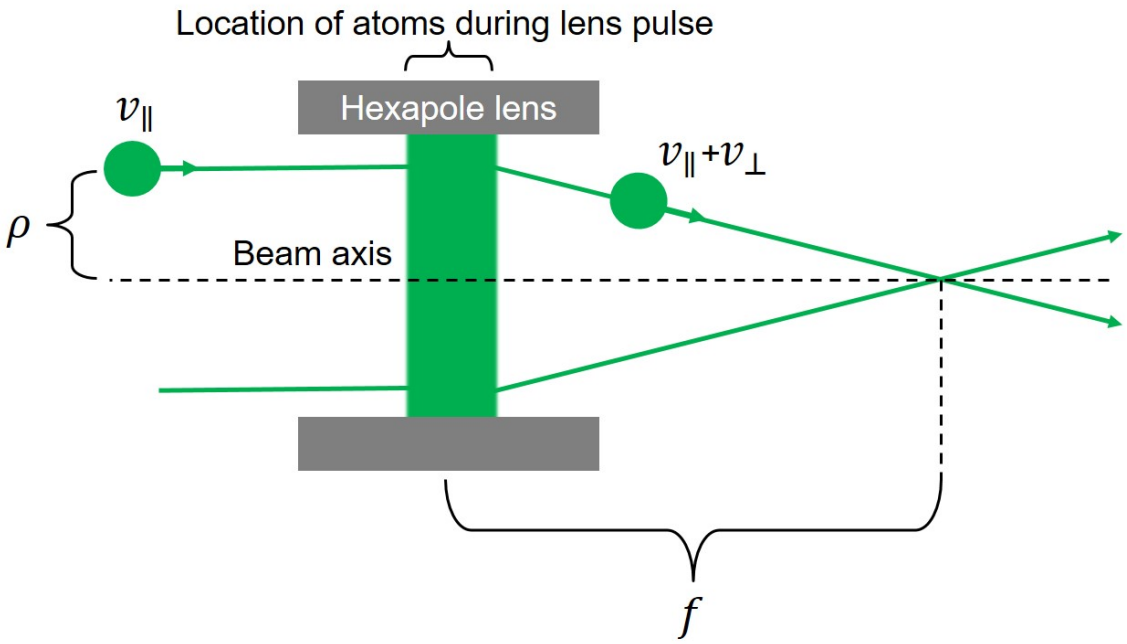

Figure 6.5: A diagram showing magnetic focusing of a collimated atomic disk.

principal requirement for magnetic lens design:

$$\boldsymbol{\nabla} B \propto \boldsymbol{\rho}. \tag{6.9}$$

In other words, we must configure our wires in such a way that B is a harmonic function of ρ. It would be somewhat undignified to describe the number of elaborate options we investigated before encountering the hexapole field, which is perfectly suited to our needs. For the purposes of this dissertation, we will pretend it occurred to us immediately.

An electromagnetic hexapole is formed by an array of six wires (or bundles of wires), carrying current in alternating directions. A cross-section of such an array is shown in Figure 6.6.

The field in the bore of a hexapole is very nearly quadratic. Explicitly,

$$B \approx \frac{6\mu_0 I \rho^2}{2\pi R^3}, \tag{6.10}$$

where I is the current and R is the distance of the wires from the axis. This approximation is quite good for $\rho \leq R/2$. Using equation 6.8, we quickly obtain an

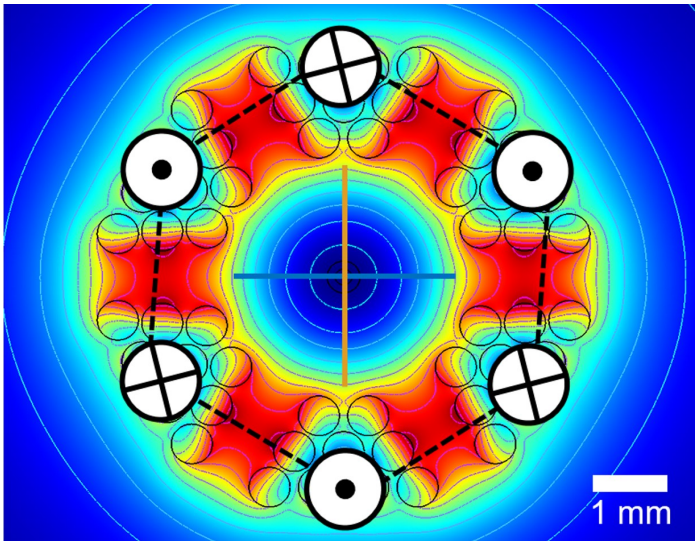

Figure 6.6: A diagram depicting an electromagnetic hexapole lens. Wires arranged at the vertices of a hexagon carry current in alternating directions into ($\times$) and out of ($\cdot$) the page. This diagram is overlaid with a color plot showing the field strength from a finite element model using bundles of wires at each hexapole point. For $\rho \leq R/2$, these models are in reasonably close agreement. Lines at the center of the image depict the traces plotted in Figure 6.8.

expression for the focal length of the disk:

$$f = \frac{v_{\parallel} m \pi R^3}{18 \mu_0 \mu_B I \tau}. \tag{6.11}$$

It is worth noting that this focal length is a linear function of $v_{\parallel}$. This differs from the steady-state lens case, in which $\tau \propto v_{\parallel}^{-1}$, yielding $f \propto v_{\parallel}^2$. A diagram depicting the focusing of a collimated disk is shown in Figure 6.11.

6.3 Focusing an atomic bullet: the case for a tapered lens

It would be an oversimplification to suggest that the linear dependence of f on $v_{\parallel}$ in the pulsed lens automatically reduces chromatic aberration. In truth, we have simply exchanged one factor of $v_{\parallel}$ for an entirely new source of error: longitudinal aberration. Even a pulsed supersonic beam has some longitudinal extent—generally

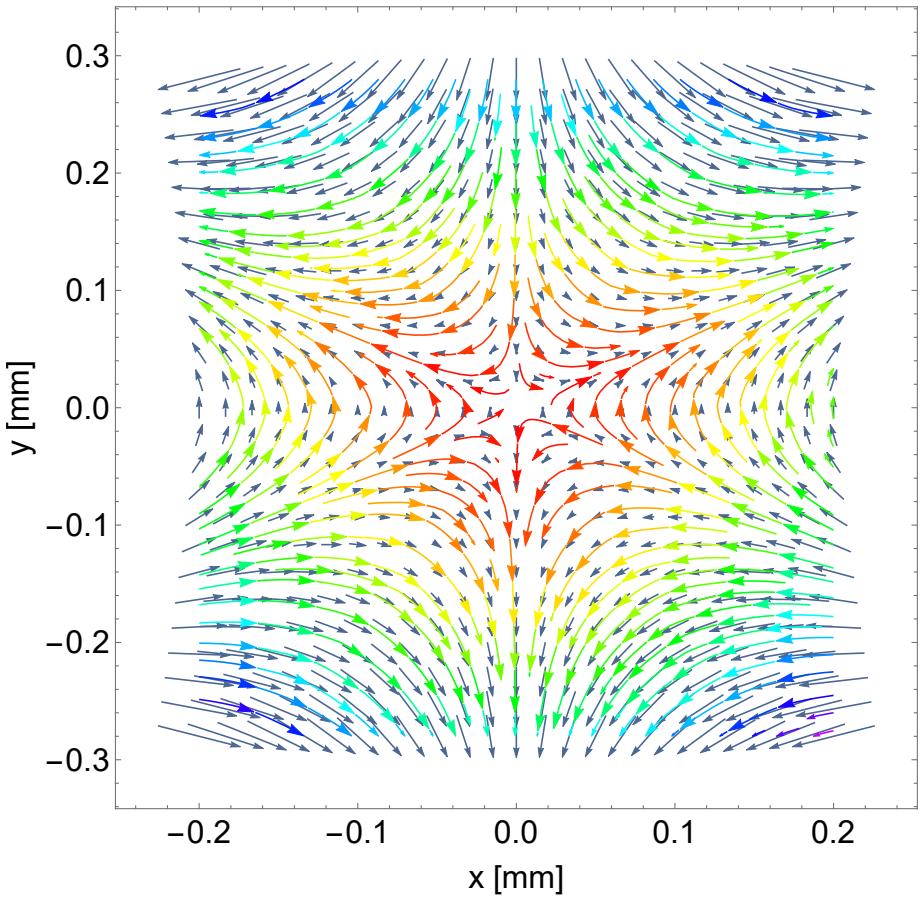

Figure 6.7: A plot showing the vector magnetic field as a function of position for the hexapole described in Figure 6.6. The arrow color represents field strength, which is weakest for small radii.

on the order of centimeters. We can think of this as a series of disks in the manner of Figure 6.9. In the steady state case, each disk passes through the entire lens, and focal point does not depend on initial position. For a pulsed lens, however, each disk focuses to a distance f from its *starting point* at the time of the pulse. Clearly this is less than ideal: we want the whole bullet to focus to a single point in space. We can achieve this by tapering the lens, thereby applying a stronger focusing field to the atoms at the front of the beam than to those at the back (Figure 6.10).

A tapered lens is beneficial in two ways. First, it allows us to correct the longitudinal aberration that arises from a pulsing the lens, thereby securing the benefit of the $f \propto v_{\parallel}$ relationship. Second, it can provide a means to further correct chromatic aberration, provided the atoms at the front of the beam are also the fastest. This so-

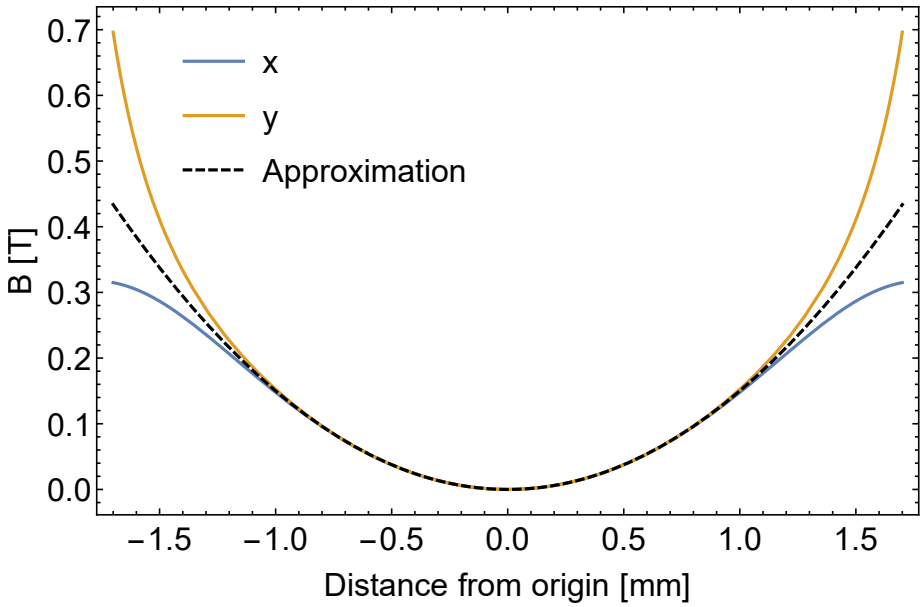

Figure 6.8: Magnetic field strength along x and y for the hexapole shown in Figure 6.6. This is calculated for $R = 2$ mm and $I = 1000$ A. For a large region inside the hexapole, the quadratic approximation (dotted line) given by Equation 6.10 is valid.

called "correlated beam" condition can be produced with the use of chopper wheels. Correlated beams have also been observed after ultra-short valve pulses, as in [3].

For a hypothetical beam whose velocity is perfectly correlated with longitudinal position, z, we can write $v(z) = v_0(1 + z/L)$. Here L is an empirical constant that heuristically corresponds to the distance the beam has traveled from the pulsed source. It is important to note that—because the nozzle is not a perfect temporal point source—any physical beam has thermal broadening on top of its correlated average velocity distribution. This temperature gives rise to chromatic aberration, but only according to $f \propto v_{\|}$. For a disk at position z relative to the center of the atomic bunch, we wish to produce a focal length:

$$f(z) = f_0 - z, \tag{6.12}$$

where f_0 is the focal length for the disk at the center of the beam. Our goal is to write an expression for the hexapole radius as a function of position: $R(z)$. From

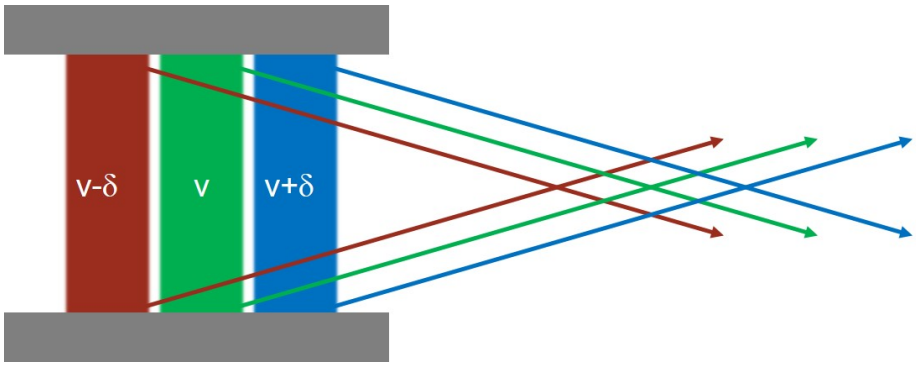

Figure 6.9: Focusing of a longitudinal series of disks by an untapered lens. Disks start at different positions and have different average velocities ($v_\parallel = v,\ v \pm \delta$). Because each disk focuses to a point a distance $f(v_\parallel)$ away from its initial position, there is no single focal plane. This results in both longitudinal and chromatic aberration.

Equation 6.11, we have:

$$R(z) = \left(\frac{f(z)}{\alpha v(z)}\right)^{1/3}, \tag{6.13}$$

where $\alpha = (m\pi)/(18\mu_0\mu_B I\tau)$. Defining $R(0) \equiv R_0$,

$$R(z) = \left(\frac{f_0 - z}{\alpha v_0(1 + z/L)}\right)^{1/3} \tag{6.14}$$

$$= R_0\left(\frac{f_0 - z}{\alpha v_0 R_0^3(1 + z/L)}\right)^{1/3} \tag{6.15}$$

$$= R_0\left(\frac{f_0 - z}{f_0(1 + z/L)}\right)^{1/3} \tag{6.16}$$

$$= R_0\left(\frac{f_0 - z}{f}\frac{L}{L + z}\right)^{1/3}. \tag{6.17}$$

While recent developments in 3D printing may facilitate the building of a pulsed lens with exactly this shape, we have found it more practical to set targets for f_0, L, and R_0, then approximate $R(z)$ to first order by applying a linear taper. Provided z is small with respect to both f and L, we quickly obtain:

$$R(z) \approx R_0\left(1 - \frac{z}{3}\left(\frac{1}{f_0} + \frac{1}{L}\right)\right). \tag{6.18}$$

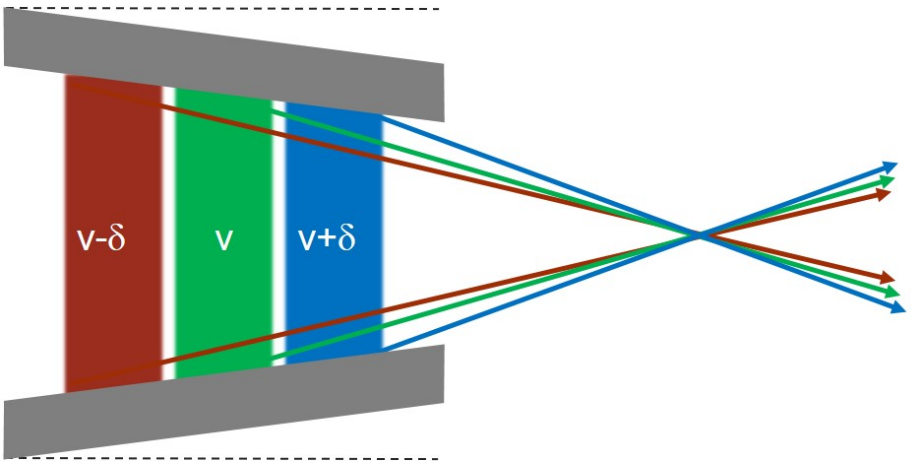

Figure 6.10: By tapering the hexapole wires, we can exert a stronger focusing field on the atoms towards the front of the pulse. If we choose the right taper, we can account for both position and momentum to send each disk to the same focal point.

Equation 6.18 is the last ingredient we need to design a tapered hexapole.

6.4 Simulations

We model this system numerically using a Runge-Kutta ODE solver (MATLAB's ODE45) to calculate atomic trajectories through the lens for various realistic beams. We assume Ne* from a supersonic valve at 77 K. Beam divergence and temperature are based on reasonable limits and varied depending on the parameters we wish to study. While it is possible to model the field gradient numerically using a finite-element model, the granularity of the mesh for such a model causes problems on the nanoscale. Because of this, we instead use the analytical approximation, which is as smooth as the true physical field.

It is important to begin by performing a few sanity checks to ensure that the model behaves as it should. The simplest case is a perfectly collimated atomic disk. Figure 6.11 shows such a beam passing through an untapered lens with a 1 mm diameter aperture and wires at radii of 1.2 mm. We invoke the "sanity check clause" (SCC: "A sanity check may ignore any factors undermining the desired result") and assume that each atom has precisely the same velocity (485 m/s) and longitudinal position. The hexapole is pulsed at 1000 A for 20 μs, yielding a focused spot 2.7 cm

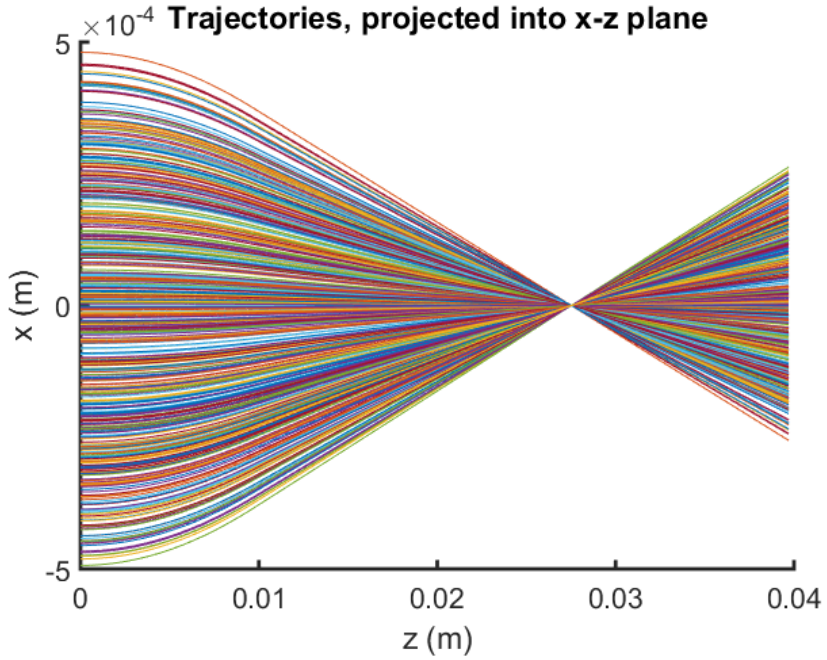

Figure 6.11: Atomic trajectories for the simplest possible simulation: a perfectly collimated disk with $T_{\|} = 0$ K. The aperture is 1 mm; the resulting spot has a FWHM of 9 pm. Just to be safe, we will simulate some more realistic beams before demanding our Nobel prize.

from initial disk position. Thanks to the SCC, the FWHM of this spot is 9 pm (not a typo). This result is excellent, as far as it goes. For one thing, it demonstrates that our hexapole field is indeed the correct choice. For another, it shows that the focusing scheme works even outside of the thin-lens regime, since atoms travel nearly a full centimeter inside the lens field. Beyond this, we can conclude almost nothing without simulating a more realistic beam.

We add transverse velocity to the beam by simulating a source aperture of diameter 1 μm, 2 m from the lens. Each point on the aperture acts like a perfectly divergent source. We retain the SCC along the beam axis, assuming uniform longitudinal position and velocity. This beam focuses to a FWHM of 6 nm. If the reader wishes to see a figure corresponding to this simulation, it suffices to cover the caption on Figure 6.11 and look at it again, pretending to see a larger final spot. From ray optics, we expect a magnification factor on the order of 0.01, so the new spot size checks out. Note that we are in the thick lens regime, so the thin lens equations will

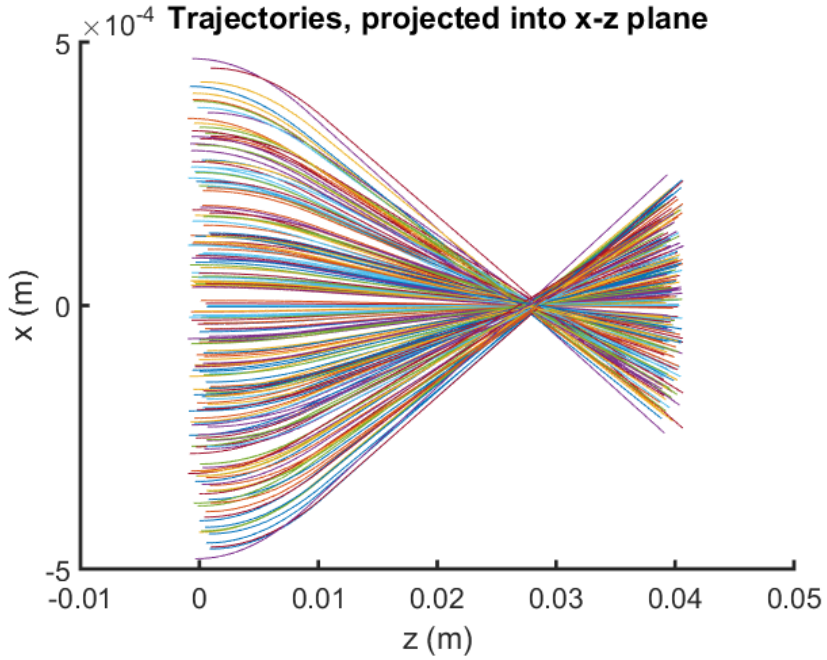

Figure 6.12: Simulated focusing of a 2 mm bullet with an untapered lens. The velocity at any given point is entirely determined by the linear correlation, meaning we are still making a fairly unrealistic assumption. Nevertheless, the 13 μm spot is enormous compared to the 6 nm we saw before. This is due to longitudinal and chromatic aberration.

only be approximate. From this simulation, we conclude that transverse velocities do not present any significant problems.

Next, we put on our helmets and give the beam a three-dimensional profile. We assume the atoms arrive in a cylindrical bullet 2 mm long. We model the longitudinal velocity using $v(z) = v_0(1 + z/L)$ with $L = 2$ m. This corresponds to a beam which starts as an uncorrelated temporal point source at the object plane. Since the temperature of any given disk within the beam remains zero, we are still making fairly strong use of the SCC. We keep the source, lens, and pulse characteristics the same. Figure 6.12 shows the mayhem that ensues. It is clear from the left side of the figure that the atoms are now starting at a range of positions. Just as we predicted in Figure 6.9, these atoms focus to different points. The result is a decidedly ugly spot with a width of 13 μm.

Now is the time to test the taper. Taking into account the average position of the atoms in the focusing field, we can estimate $f \approx 2$ cm. Equation 6.18 thus calls for a

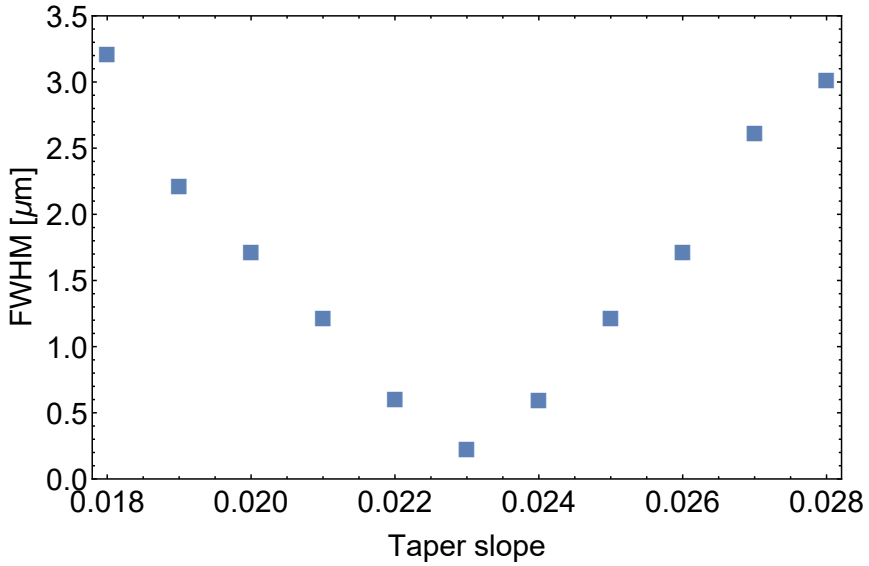

Figure 6.13: Focused spot sizes from simulations at various taper slopes. The best slope is approximately 0.23. This taper reduces the 13 μm spot from Figure 6.12 to 210 nm.

taper slope ($\beta = R_0(f^{-1} + L^{-1})/3$) on the order of 0.02 (this slope is unitless, though it sometimes helps to think of its units as [m/m]). Searching empirically around this value, we find the spot size varies smoothly. Figure 6.13 shows the data from this search, from which we obtain a minimum sot size of 210 nm at a slope of 0.23. The atomic trajectories from this optimized simulation are shown in Figure 6.14. This is a simulated realization of the model illustrated in Figure 6.10. Having confirmed that the model produces reasonable results for unrealistic systems, we now attempt to simulate a completely realistic beam. The main thing left to add is temperature. From front to back, the variation of the average beam velocity is on the order of the Doppler limit. At each position, however, we have assumed we know the speed exactly. We now relinquish this requirement, adding to the expected speed a random variation on the order of the recoil limit. The resulting velocity distribution is shown in Figure 6.15. This thermal broadening is clearly significant, but since the beam remains partially correlated we can still hope to put the taper to good use. Sure enough, the FWHM of a spot produced with this beam is only slightly larger than the "unphysical" version: about 220 nm. Adding a larger velocity spread causes somewhat more trouble. If each disk has a thermal component on the order of the

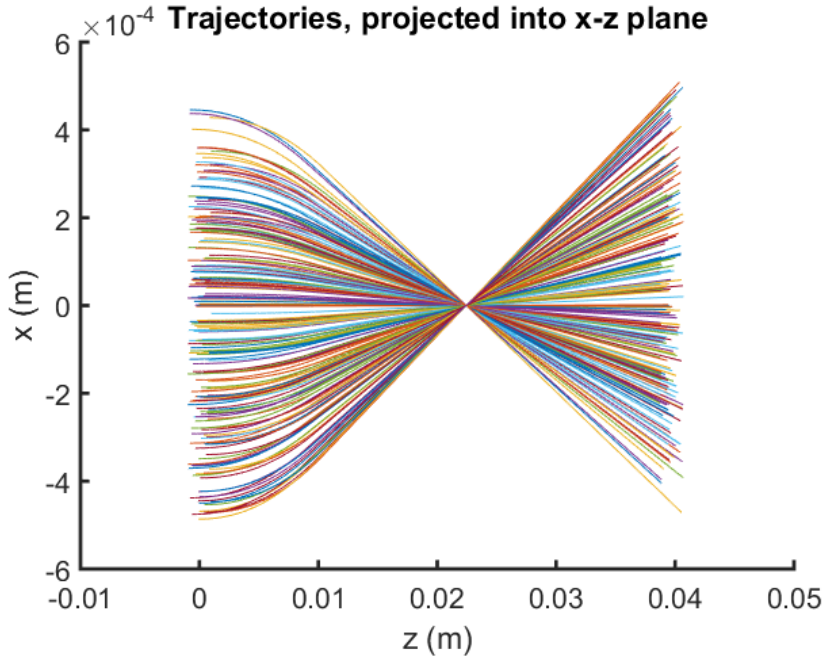

Figure 6.14: Atomic trajectories for a tapered lens and the same 2 mm beam as in Figure 6.12. At a taper slope of 0.23, the spot size is 210 nm. This is still larger than we would expect from ray optics, but it is quite an improvement.

Doppler limit, the bullet is completely uncorrelated and the spot swells to 800 nm. Note that the taper is still helpful, since 800 nm is a significant improvement over the untapered 13 μm spot.

We can now begin exploring the limits of the tapered lens with a physical—albeit cold—beam. Using the recoil-broadened, correlated bullet, we first "stop down" the lens aperture. As discussed at the beginning of this chapter, this shrinks the circles of confusion associated with incorrectly focused atoms. Naturally, the downside to this technique is that fewer atoms make it through the lens. At $D = 500$ μm, we obtain a 100 nm spot. Stopping down further to 100 μm, the spot hits 21 nm. We can obtain similar results by shortening the bullet, which is essentially an "aperture reduction" in the longitudinal direction. A 1 mm bullet with a 100 μm diameter lens aperture yields a 9 nm wide image spot, which is on the order of what we expect from ray optics.

The agreement with traditional optics in our final example suggests that this system may be capable of true imaging on the nanoscale. During a period (one of

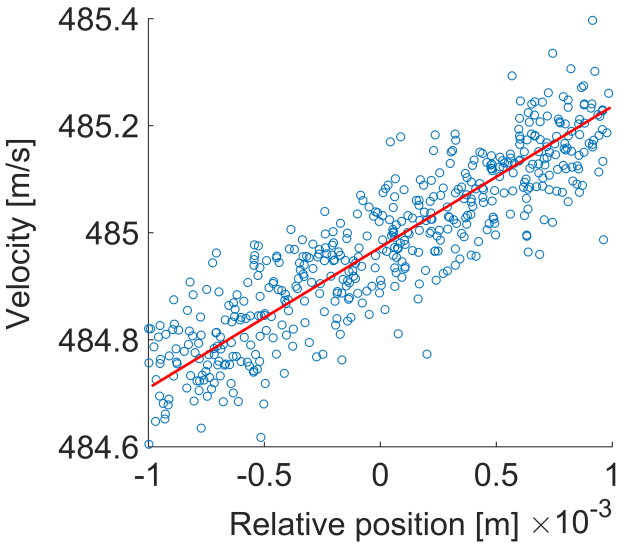

Figure 6.15: Correlated velocity spread for the 2 mm beam from Figure 6.14. The addition of a random longitudinal velocity component broadens the distribution, but does not destroy the correlation. From front to back, the velocity spread is a little over twice the Doppler limit. The red line indicates the correlation function for the un-broadened beam used for Figure 6.12.

many) when simulations were cooperating better than reality, we took the time to explore this. In order to properly evaluate imaging, it helps to use a shape with as few symmetries as possible. One such candidate is the letter F. Replacing the mask aperture with a hole shaped like an F is fairly straightforward. Figure 6.16 shows the simulated beam cross section for 2000 atoms at both the mask and the image planes. Despite a few stray particles, the imaged F is quite clear and has features on the scale of 25 nm. The width of the F at the object place is 10 μm, which makes the image width of 100 nm quite acceptable. It is interesting to look at the beam's cross section as it passes through the lens. Figure 6.17 shows the beam at the mask, at the aperture, and immediately after the lens. As in traditional optics, the "F" structure is completely undetectable at the lens plane. Also notable is the significant motion of atoms between the front and back of the lens. This is another indication that we are working in the thick lens regime. Finally, we note that the image appears upside-down and backwards, just as we expect.

Because the letter F does not always inspire passion, we decided to try imaging a

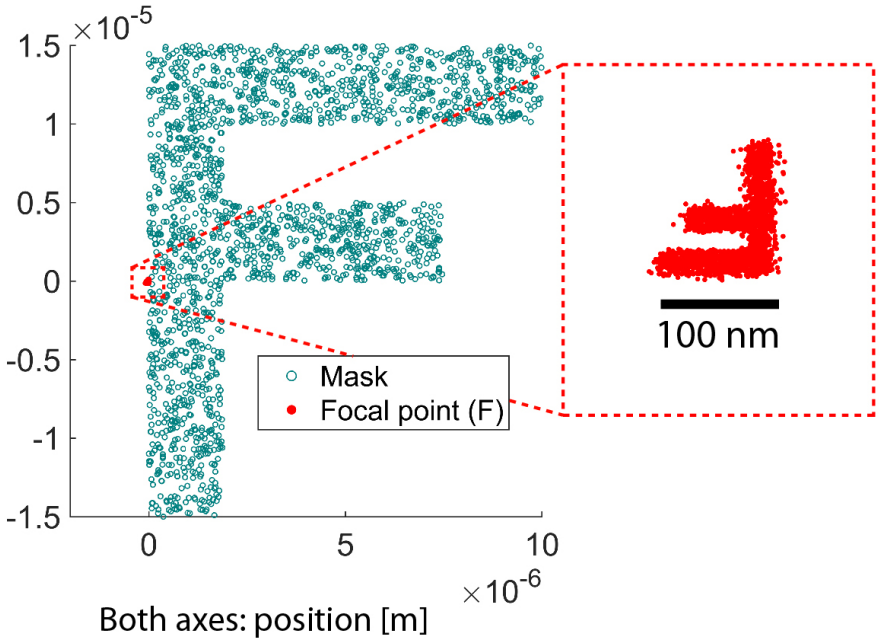

Figure 6.16: Simulated imaging of an object in the shape of the letter F. This simulation was run using the beam from Figures 6.14 and 6.15 and a 100 μm lens aperture. The width of the F is demagnified by a factor of around 100, just as ray optics would predict.

more interesting shape as well. Figure 6.18 shows a simulated projection of a Batman logo into the nanoscale regime. Geometrically, this worked just as well as the letter F. Psychologically, it was significantly more rewarding than the F due to its potential application; namely, summoning very small crime-fighters.

In addition to justifying the linear taper, these models support the prediction that a pulsed, tapered hexapole can achieve resolution on the scale of 10 nm and demagnification factors of 100x. With a 500 μm aperture, this lens has a speed of f/44.

6.5 Phase space

The behavior of the lens in phase space is a perfect example of Liouville's theorem in action. While the beam appears to become more concentrated in position-space,

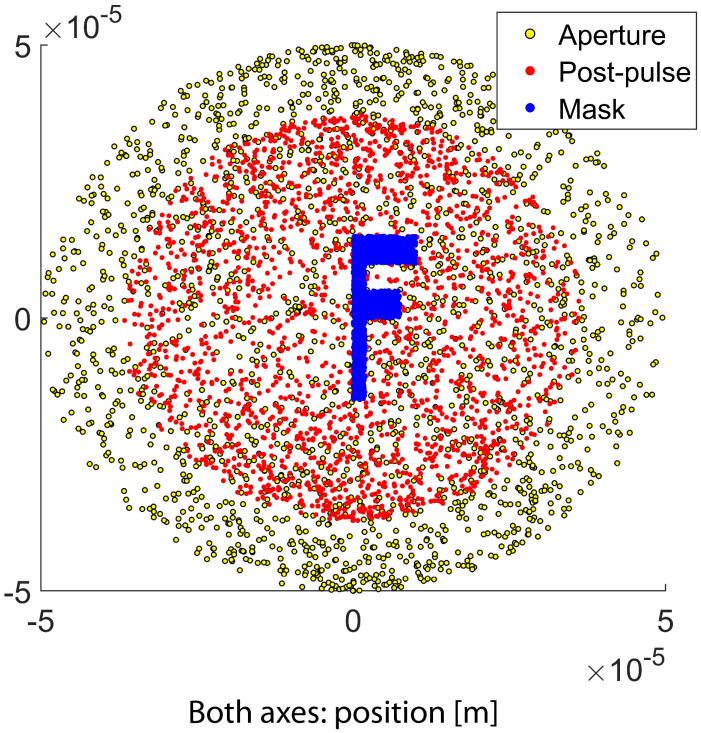

Figure 6.17: Three beam cross sections for the same case as in Figure 6.16. These show the difference between the beam at the mask, where the letter F is clearly visible, and the beam at the lens, where no information is apparent. Please attempt not to note the aspect-ratio difference between this F and the one in Figure 6.16, as it will reveal that in the latter case we adjusted the horizontal scale to make the shape look nice.

it broadens by the same amount in momentum-space. It turns out that any time-dependent force will yield the same result: no conservative force is capable of increasing a beam's phase space density. Lensing can be part of a powerful brightening technique when performed immediately before laser cooling, as described in [39].

We must also briefly discuss the phase space densities we will need in order to achieve nanoscale images. A 500 μm diameter aperture at a d_o of 2 m with a 2 mm bullet and a longitudinal temperature on the order of the recoil limit corresponds to a phase space density of around 3×10^{-7} per atom. The phase space density of atoms in a MOT is on the order of 10^{-6} [38]. Assuming we can achieve this density, we can expect only a few atoms per shot. That said, the high repetition rate of which EL valves are capable—as high as 600 Hz—means the lens could still deliver 10^3 atoms per second

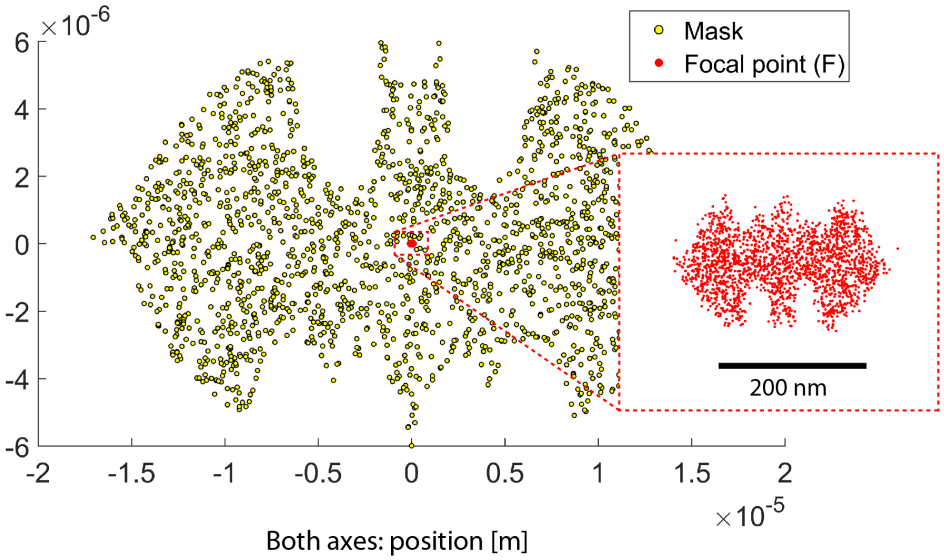

Figure 6.18: Simulated projection of the batsign into the nanoscale. This figure is made using the same simulation parameters as for the F.

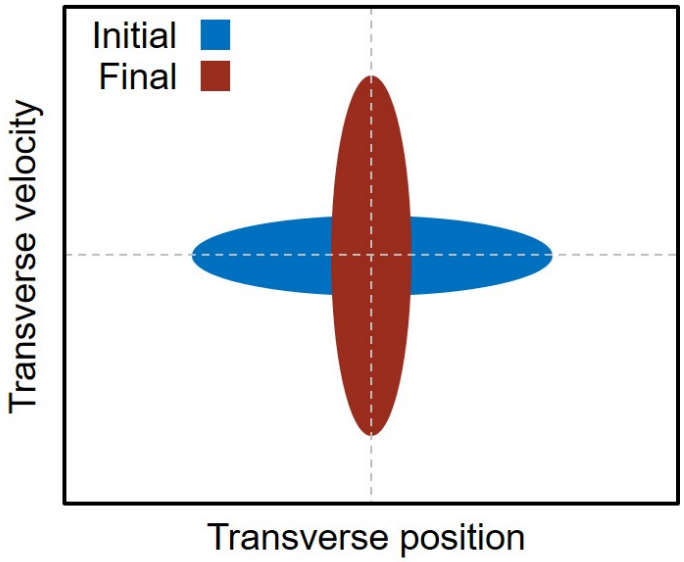

Figure 6.19: Phase space description of the lens transformation. While the beam appears to concentrate in position-space, this focusing is balanced by an expansion in momentum-space. Rather than brighten the beam, all a lens does is squish most of its phase space volume into the momentum dimension. It is worth noting that if laser cooling is used precisely at the focal point, the focused *and* cooled beam is much brighter than a beam produced by cooling alone.

to a 100 nm spot. This flux is high enough that even a 100 μm aperture—producing 10 nm spots—would be viable. Certainly, each of these cases involves higher atom flux than would pass through a 20 nm pinhole lens, even at a much smaller distance. Nevertheless, the rather stringent phase space density requirements for nanoscale focusing give further motivation to the MOP cooling efforts under development on the other side of the Raizen lab [62].

Chapter Seven: Experimental setup

Having discussed the important theoretical aspects of neutral atom focusing, we now turn to the task of building a working prototype. This requires coaxing several complex, fragile systems into functioning properly in concert. We avail ourselves of many useful tools in this phase of the project, perhaps none more crucial than strong coffee and a swearing dictionary [63]

7.0.1 Overview

Figure 7.1 provides a time-resolved picture of the experimental beamline. Neon is released from an Even-Lavie supersonic valve into a vacuum chamber. An RF discharge excites the atoms into the metastable Ne* state. After it passes through a skimmer, we collimate and brighten the beam using both transverse and chirped longitudinal laser cooling. We also optically pump the beam to the $m_J = 2$ LFS state. Following laser cooling and optical pumping, we pass the Ne* beam through either a set of individually translated knife edges or a brass slide containing apertures of various shapes. This serves as the object plane for our imaging scheme. After the object plane, the atomic beam propagates 135 cm before entering the pulsed electromagnetic hexapole lens. Immediately in front of the lens, a stainless steel chopper wheel reduces the longitudinal extent of the beam. Once the atoms have entered the lens, we pulse a current to focus the beam. For this first proof-of-principle experiment, we use currents on the order of 200 A, resulting in focal lengths between 0.4 and 0.6 m. After passing through the magnetic lens, the focused atoms arrive at a microchannel plate (MCP) that serves as the image plane. Metastable atoms arriving at the MCP excite an electron cascade, which is then accelerated towards a phosphor screen. We use a CCD camera to image the phosphor screen through a window in the vacuum chamber. This system allows us to characterize the shape and size of the cross section of the atomic beam where it hits the MCP.

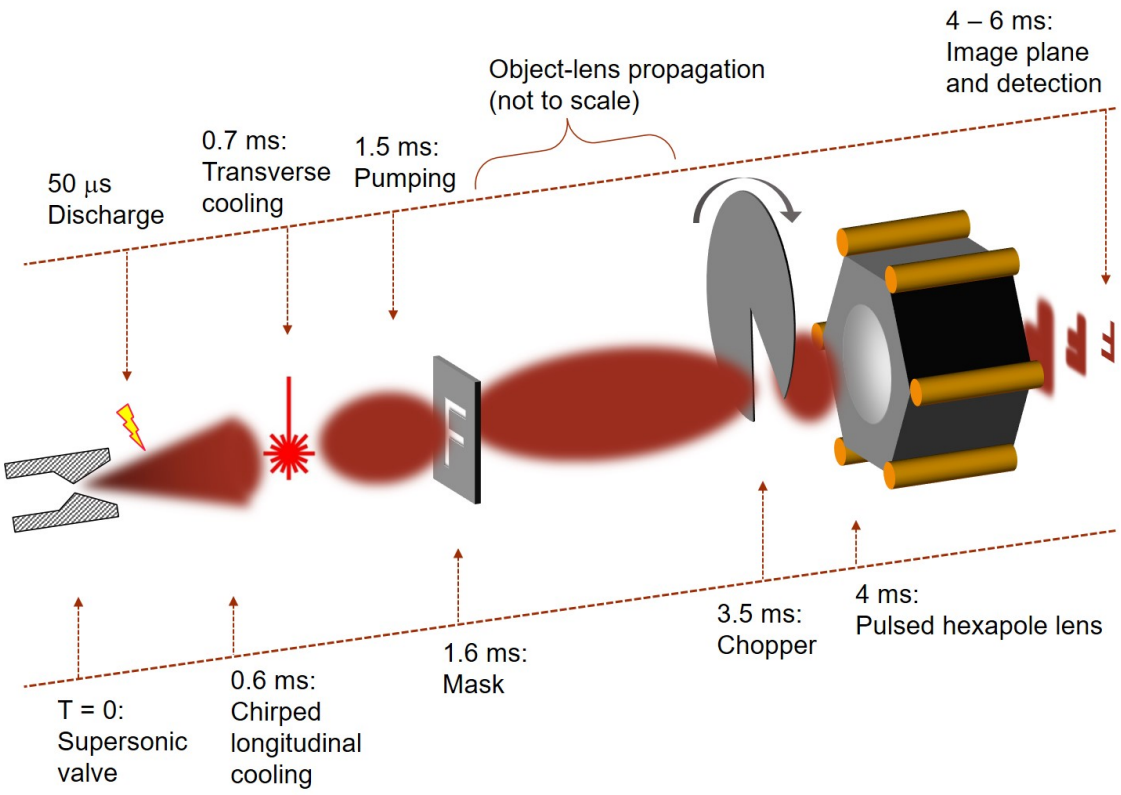

Figure 7.1: A time-resolved picture of the experimental beamline.

7.1 Even-Lavie cryogenic valve

All beams in this work originate from a pulsed Laval-type nozzle built by Dr Uzi Even and Nachum Lavie [64, 65]. Depicted in Figure 7.2, this device consists of a trumpet-shaped expansion aperture and a solenoid-actuated plunger capable of releasing gas pulses as short as 10 μs. Due to the supersonic expansion process (Chapter 2), the atomic beam from this nozzle is much colder and brighter than an effusive beam. In order to reduce the mean speed of the beam, the nozzle is held at 77 K using a cold-finger connected to a dewar filled with liquid nitrogren. A dielectric barrier discharge inside the valve trumpet excites the atoms via electron bombardment, leaving a fraction ($\sim 10^{-4}$) of the outgoing gas in a metastable state. A 3 mm skimmer placed 17 cm from the nozzle selects the center of the beam, transmitting it to the adjacent chamber. The majority of the gas load from the valve is contained inside the nozzle chamber, which is held at 10^{-8} Torr using a 300 L/s

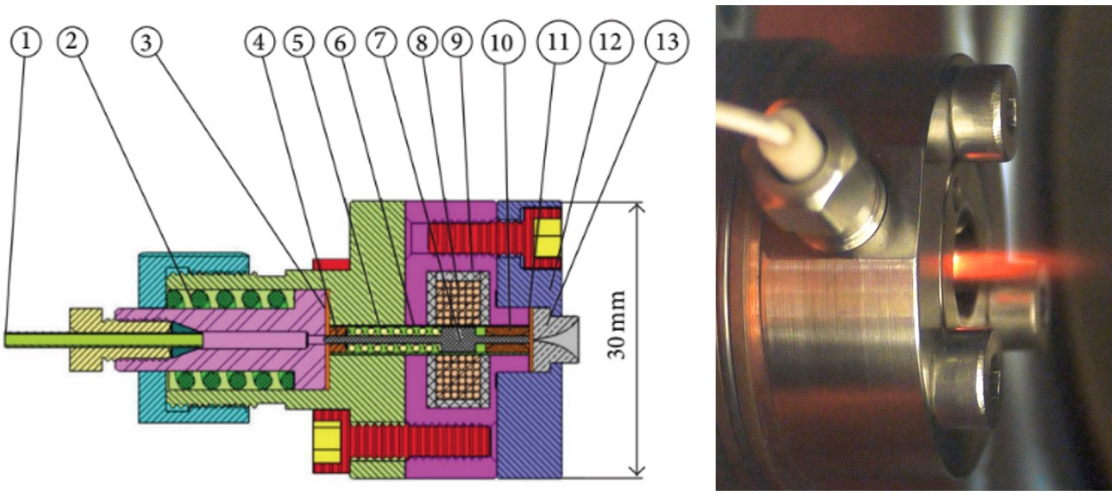

Figure 7.2: **Left panel**: (1) stainless gas inlet tube (1/16") gas feed; (2) tightening spring (180 N) and pressure relief valve; (3) Kapton foil gasket seals; (4) ceramic (Zirconia or Ruby) rear guiding precision ferrule; (5) return spring (stainless alloy); (6) thin walled pressure vessel (Inconel or Zirconia ceramic); (7) reciprocating plunger (magnetic stainless steel alloy); (8) Kapton insulated copper coil; (9) Permendur magnetic shield and field concentrator; (10) ceramic front guiding precision ferrule; (11) Kapton foil gasket seal (front, 0.125 mm. thick); (12) front flange and valve body (copper or stainless); (13) conical (or parabolic) shape expansion nozzle (Zirconia ceramic or hardened stainless steel). **Right panel**: Photo of DBD-equipped EL Valve with visible discharge. Images and description courtesy of Prof. Uzi Even and Nachum Lavie [66].

turbomolecular pump.

A diagram of the valve is shown in the left panel of Figure 7.2. The important moving part in this system is the plunger, which rests against a Kapton gasket to seal a 200 μm hole. This opening connects the gas reservoir (held at 20 bar) to the Laval nozzle and the vacuum chamber. The plunger is pulled back by pulsing a solenoid, which produces a brief field on the order of 2 T. This pulse retracts the plunger by just enough (around 100 μm) to admit a pulse of gas into the trumpet, after which the return spring re-establishes the seal. The pulse length can be varied quite widely, but during cryogenic operation we obtain the best results with a valve opening time of 21 μs. Under ideal conditions, this valve can produce intensities of 4×10^{23} atoms/sr/s [55]. The return spring and the plunger are quite delicate, and even a small deformation of either one can cause serious valve malfunction. The front

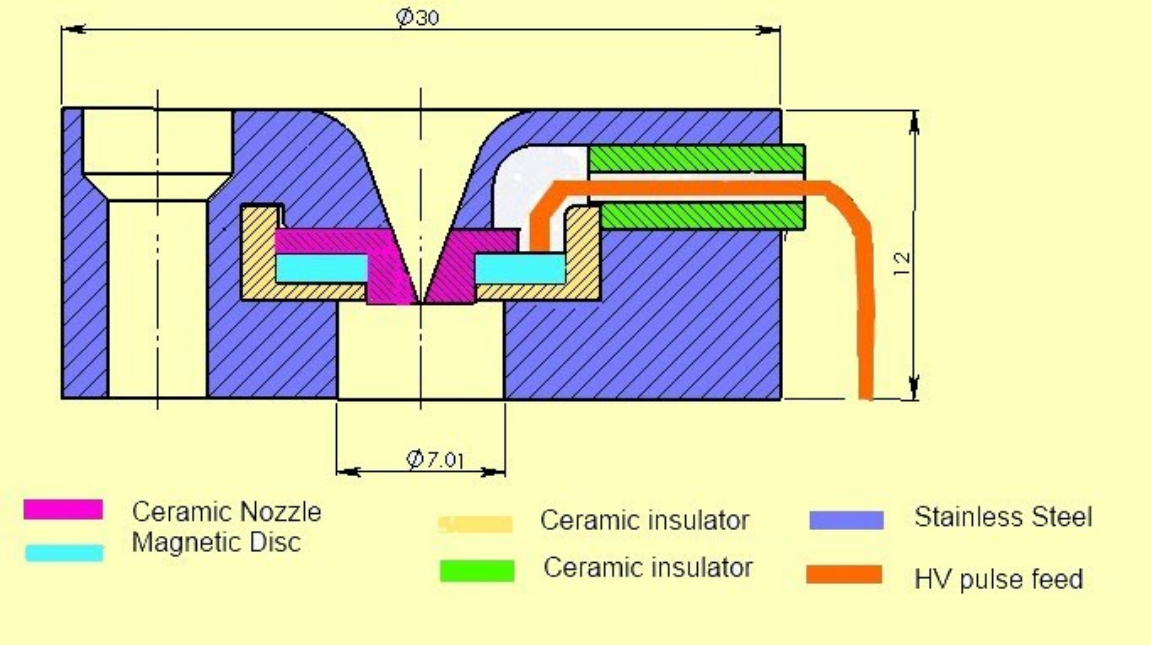

Figure 7.3: Schematic of DBD structure. The ceramic portion of the nozzle cone is designed to minimize sputtering due to high energy electrons colliding with a metallic electrode.

flange of our EL valve contains a dielectric barrier discharge (DBD) excitation source (Figure 7.3). This an upgrade, and is not depicted in the left panel of Figure 7.2. The DBD consists of a high-voltage RF electrode shielded by a ceramic case that forms the lower portion of the nozzle cone (Figure 7.3). The RF electrode, with the stainless steel flange face acting as ground, accelerates electrons through the emerging gas cloud. Electrons collide with and excite ground state atoms, leaving approximately 1 in 10,000 in the 3^3P_2 metastable state. The ceramic case surrounding the electrode reduces electron sputtering, yielding a colder beam. The DBD source allows us to produce metastable beams from a cold nozzle with speed ratios as high as $s = 37$, which corresponds to a temperature of 140 mK.

It is worth mentioning the somewhat pedestrian topic of gas line management. The EL valve is designed to quite precise specifications. At cryogenic temperatures, any contamination of the source gas can lead to extreme beam degradation. In severe cases, condensation of contaminants can cause the plunger to stick. Needless to say, this undermines scientific progress. In order to minimize contamination and moisture in our research grade neon, we operate our experiment without a pressure regulator.

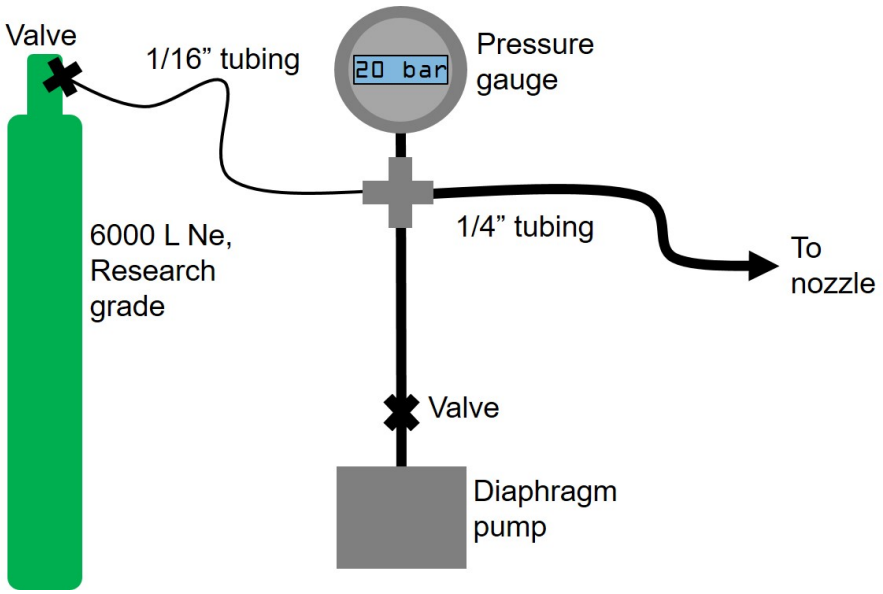

Figure 7.4: A schematic of the gas supply line. To avoid contamination, no regulator is used. The 1/16" Swagelok tubing restricts gas flow from the cylinder, affording reasonably good control over the pressure that reaches the valve. The 1/4" Swagelok tubing functions as a gas reservoir, allowing us to fill the line to the required pressure (around 20 bar) and then close all valves for up to eight hours of continuous operation.The diaphragm pump is used to flush and pump out the line before each use.

A 1 m long section of 1/16" Swagelok tubing connects the 6000 L Ne tank to a shorter network of 1/4" tubing, which in turn leads to a digital pressure gauge and the valve reservoir (Figure 7.4). A diaphragm pump is used to clear the gas line before use. The 1/16" tubing dramatically restricts the flow of gas towards the nozzle, so that we are able to briefly open the 6000 L tank (pressure 150 bar) without filling the experimental side of the gas line beyond about 30 bar. The 1/4" tube section functions as a tiny "lecture bottle" and provides enough gas for us to run the experiment continuously for a full day. When setting up a new section of Swagelok tubing, we exercise extreme vigilance in the process of leak-checking. Having eliminated all leaks, we also use the diaphragm pump to rough out the line for at least a day before cooling the valve. Finally, at the beginning of each experiment, we "cycle the line" by filling and vacuuming it, usually about three times. Taken together, these techniques help avoid contamination.

Following the skimmer, the Ne^* has a divergence of 17 mrad and a longitudinal

temperature on the order of 100 mK. We estimate a flux of 10^9 metastable atoms per shot at a firing rate of 4 Hz. To some extent, these numbers depend on the performance of the nozzle, which varies. We use apertures and a chopper to establish precise limits on the dimensions and temperature of the final beam, so the main negative effect of a misbehaving nozzle is a reduction in flux.

7.2 Cooling and pumping

In order to improve beam flux and magnetically polarize our Ne* beam, we use a frequency-stabilized extended cavity diode laser (ECDL) tuned to the 3^3P_2-3^3D_3 cycling transition. The system is locked using Doppler-free absorption spectroscopy. We injection-lock a slave laser to obtain more power. Acousto-optic modulators (AOMs) provide all necessary frequency shifts. Transverse and longitudinal cooling immediately after the skimmer brighten the beam by an order of magnitude. Immediately before the object plane, an optical pumping beam polarizes the Ne* into the $m_J = 2$ LFS state.

7.2.1 Laser system

We require approximately 100 mW of single-mode laser light, stabilized at the cycling transition with an accuracy better than one line-width (10 MHz). Two laser diodes, one in an ECDL and one injection locked, provide this light. A glass saturation cell excited with an RF coil provides a sample of Ne* to which we lock the master laser. The ECDL consists of a multiple quantum well AlGaInP diode (Opnext HL63133DG) in the Littrow configuration with a diffraction grating and an output mirror (Figure 7.5). The grating and mirror are placed together on a pivoting platform whose angle is controlled with a piezoelectric stack. Light from the diode passes through a collimation lens before hitting the grating, where first-order diffraction returns a frequency-correlated feedback signal to the laser diode. The zero-order beam continues towards the mirror and the rest of the optical setup. The first-order retroreflected light re-enters the laser diode, forming the eponymous "extended cavity." The frequency at which this cavity resonates is selected by changing the angle of the pivot plate. Using a piezoelectric stack (controlled with a Thorlabs MDT693A) allows us to automate this process, varying the grating angle according to an electrical error

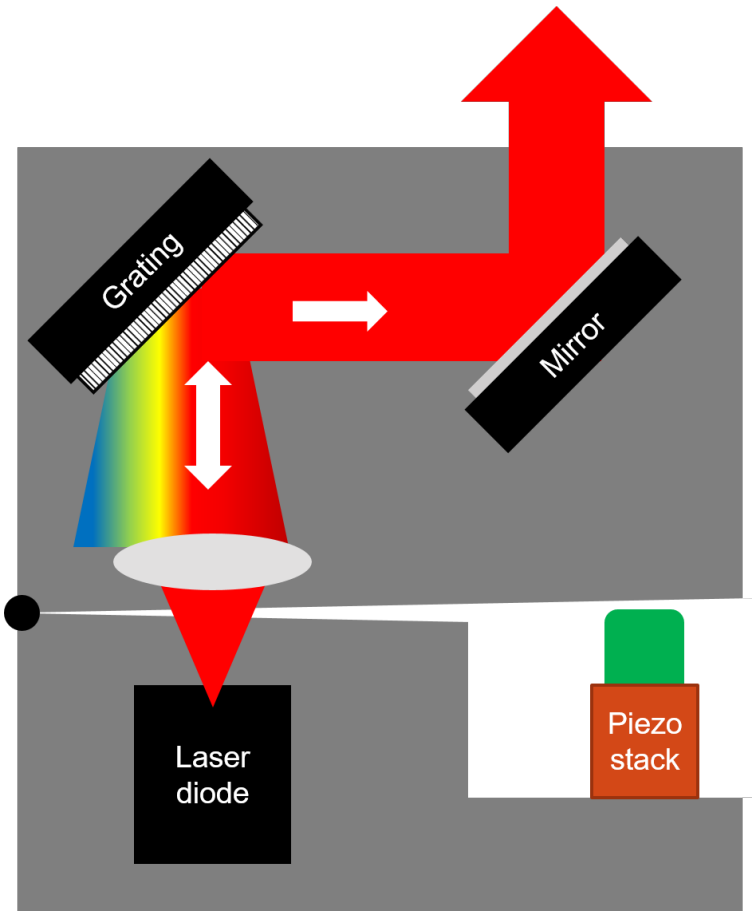

Figure 7.5: Schematic of the Littrow configuration for an extended cavity diode laser. The first-order retro-reflected beam re-enters the diode, forming an "extended cavity" whose frequency can be adjusted by pivoting the grating mount. The zero-order beam reflects off a second mirror to make the output angle independent of grating position. A piezoelectric stack provides electronic access to this system, which is an important step in automation.

signal that is discussed below. The ECDL output wavelength also depends strongly on both diode temperature and current. The temperature is stabilized using a thermoelectric cooler, a temperature transducer, and a proportional-integral-derivative (PID) control module (Thorlabs TEC3-6, AD590, and TCM1000T). The diode current is controlled with a Newport Model 505 current controller. A feed-forward circuit from the piezo controller adjusts the diode current in concert with the grating angle to extend the continuous-single-mode tuning range of the system. An optical isolator (Thorlabs IOT-3D-633-VLP-RFR) prevents unwanted feedback. A sampling mirror redirects a portion of the output beam to a Fabry-Perot cavity (Thorlabs SA200-5B) and a wavemeter (Exfo WA-1000). Though the diode output is nominally 175 mW, our need for a specific wavelength restricts the operational current range. After diagnostics and locking (discussed below), we are left with around 50 mW of useful power from the ECDL, which is less than we need.

We generate more power at the same frequency by injection locking a slave laser (Figure 7.6). This technique is based on Bose statistics; in particular, on the tendency of photons to stimulate emission of light that matches their own quantum state. Injecting light of the desired wavelength into the slave laser diode causes that wavelength to reach threshold more easily. In our system, the injection beam enters the laser diode through the side of a polarized beam splitter (PBS) in the slave laser's isolator. Temperature and current are controlled using the same methods as above, though no feed-forward circuit is necessary here. Careful mode-matching, using a series of telescopes and folding mirrors, allows us to produce 100 mW of added power with precisely the same frequency as the light from the master laser.

In order to properly implement an optical molasses (Chapter 3), we need to stabilize our laser to within one transition linewidth [67, 68, 69]. This accuracy—10 MHz at 640 nm—corresponds to one part in 10^7, or 0.00001 nm. Our wavemeter provides six digit precision, but even 640.402 nm is too uncertain by two orders of magnitude. We lock our laser system by measuring its absorption in 50 mTorr of neon in a glass cell (Figure 7.7). A high-voltage RF coil wrapped around this cell and run at 40 MHz produces a plasma, yielding a sample population of Ne^*. Because the effective temperature of this plasma is quite high, the Doppler-broadened absorption spectrum is not nearly sharp enough for our needs. To obtain a Doppler-free signal, we send a counter-propagating pump beam through the cell along a path that intersects with the probe. The pump beam has high enough power (generally a few mW)

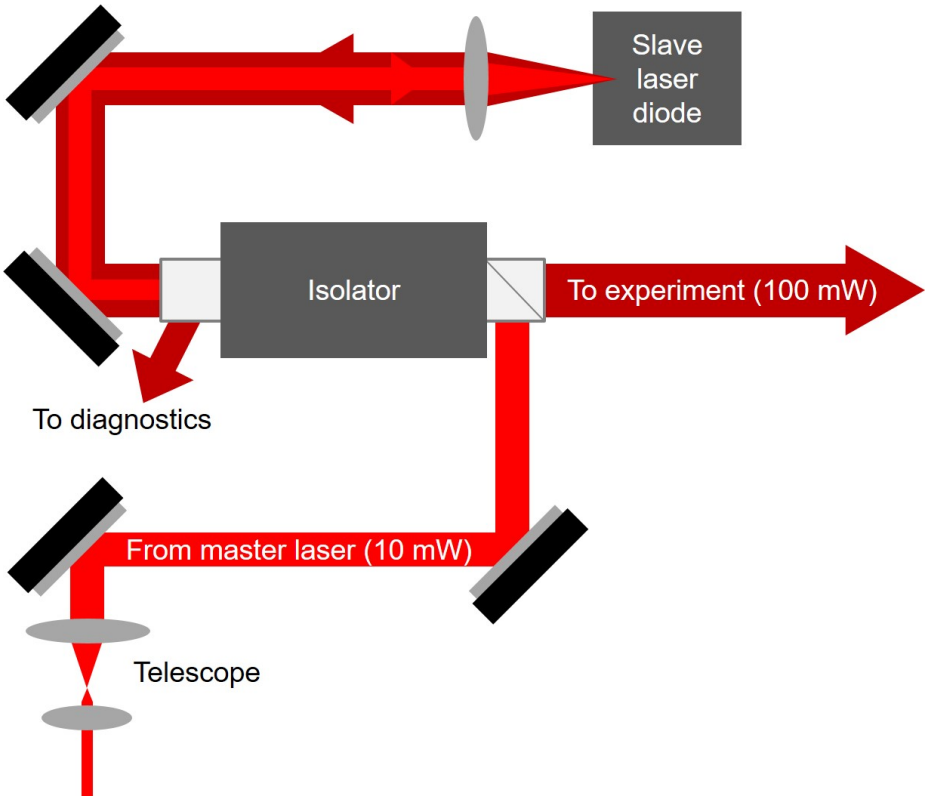

Figure 7.6: Injection locking schematic. Seed light enters through the side of a PBS in the slave's isolator. Careful mode-matching, temperature control, and current tuning allow us to clone the master laser light, producing around 100 mW more power. Not pictured: several other telescopes, folding mirrors, and waveplates.

to exceed the saturation intensity, reducing the population of potential absorbers for the (sub-saturation) probe beam. This is observed as an increase in the probe beam intensity at the photodiode. However, this absorption reduction only occurs for the atoms in the cell which are resonant with both beams. If the probe and pump were at the same wavelength, these atoms would be those with zero longitudinal velocity. For reasons that will become apparent, we instead use an AOM to shift the frequency of the pump beam up by 80 MHz. If the original beam is red-detuned by 40 MHz, the pump will end up blue detuned by the same amount. In this case, both lasers will be resonant with the velocity class of atoms moving towards the probe beam with a Doppler shift of 40 MHz (Figure 7.8). By scanning the pump and probe—with a fixed offset—through the transition, we observe sharply reduced absorption at the frequency for which both beams interact with the same velocity class. This is referred

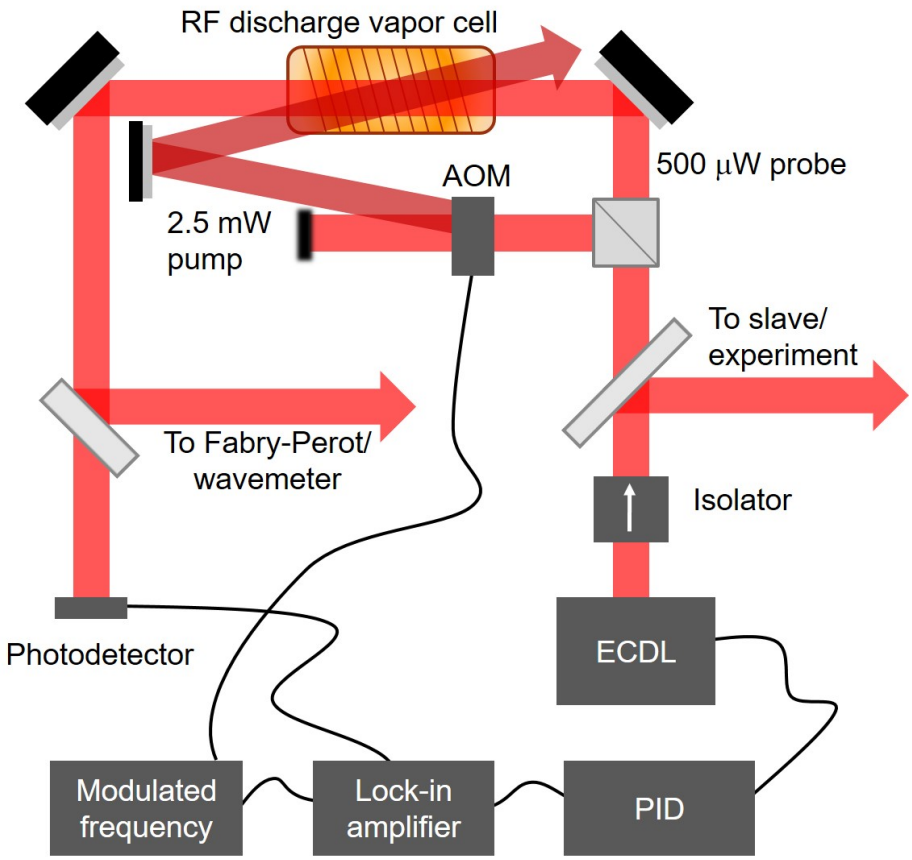

Figure 7.7: Beam schematic showing Doppler-free laser frequency stabilization. A portion of the ECDL output is split into pump (above saturation) and probe (below saturation) beams. The pump is frequency shifted using an AOM by 80 MHz plus a small time-dependent component. When the probe and the pump interact with the same velocity class, the absorption of the probe beam is reduced. This is seen as an intensity increase at the photodiode. The modulated signal is detected with a lock-in amplifier and used as the error signal for a PID controller connected to the ECDL grating.

to as a Lamb dip. The advantage of using an AOM on the pump beam is that the frequency shift can then be modulated:

$$\Delta f = 80\text{MHz} + \delta \sin \omega t, \tag{7.1}$$

where $\delta \approx 1$ MHz and $\omega/2\pi \approx 5$ kHz. This has the effect of shifting the Lamb dip from side to side in frequency space. Figure 7.9 shows the AC and DC signals arriving at a photodiode using this modulation technique. The DC signal is present, but only acquired after a fairly long integration. The AOM frequency modulation described in Equation 7.1 produces what amounts to a first-derivative of the DC signal, which is useful in two ways. First, the use of a lock-in amplifier (SRS SR510) dramatically improves the signal-to-noise ratio of the AC signal. Second, the first-derivative lineshape means that the AC signal crosses zero with approximately linear slope precisely at the peak of the Lamb dip. This makes the use of a PID (SRS SIM960) spectacularly easy. The error signal from the lock-in amplifier is fed to the PID, which (through an amplifier) controls the voltage on the piezoelectric stack. The final output beam is stabilized to within a few MHz at a point precisely 40 MHz below the Ne* transition. A photograph of this portion of the laser beamline is shown in Figure 7.10.

A starting frequency 40 MHz below the Ne* cycling transition is not particularly useful to us until we shift it to the desired energy. For transverse cooling, we want a red detuning of approximately 10 MHz. This frequency also works for the pumping, which we configure as a second round of transverse cooling, albeit with circular polarization and a carefully maintained background magnetic field. For the chirped longitudinal beam, we need a time-varying detuning on the order of 750 MHz. These frequencies are obtained using AOMs in a cat's eye double-pass configuration, which maintains a stable output beam angle for a wide range of frequency shifts [70]. A steady output angle is especially important for the chirped AOM, which would otherwise become hopelessly misaligned as the frequency changed. Illustrated in Figure 7.11, the cat's eye system consists of an AOM, a lens, and a mirror, each separated by one focal length of the lens. An input beam traveling horizontally from left to right in the figure is diffracted upwards at an angle given by $\sin(\theta) = \lambda F/c$, where λ is the wavelength of the light, and c and F are the respective speed and frequency of the sound wave in the AOM. We assume that this deflection constitutes the negative-first-order beam, in which case its frequency is shifted by $-F$. Reaching the lens,

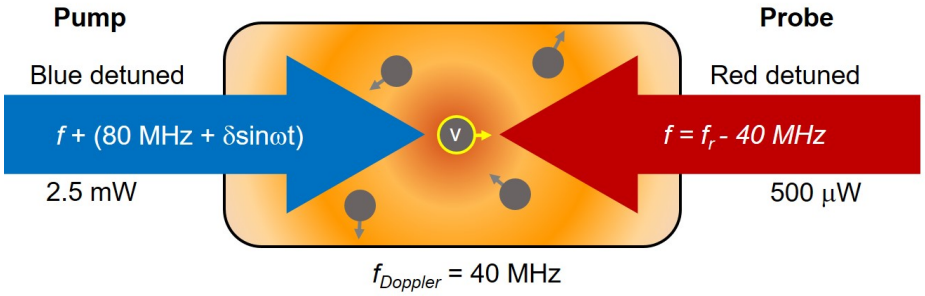

Figure 7.8: Doppler-free saturated absorption. The pump beam (above saturation, left-to-right) is shifted by 80 MHz with respect to the probe (below saturation, right-to-left). When the probe is red detuned by 40 MHz, both beams interact with the atoms moving from left-to-right with a Doppler shift of 40 MHz. This results in diminished absorption of the probe due to fewer atoms in the lower level of the transition. The resulting Lamb dip is very narrow compared to the Doppler-broadened absorption curve. Adding a small modulation (on the order of 1 MHz) to the pump frequency shift allows for the use of a lock-in amplifier, greatly simplifying both detection and the automation of a PID control system.

this beam is refracted back into the horizontal direction, as dictated by ray optics. It is focused to a waist at the mirror, which reflects it straight back along the same path. Reaching the lens a second time, the beam is re-collimated and directed back towards the focal point of the lens. Since this point also happens to be the center of the AOM, an identical diffraction process sends a twice-shifted beam back along the original path. Using a quarter wave plate (QWP) and a PBS, the final beam is siphoned away and sent towards its target atoms. Figure 7.11, as usual, neglects a great many folding mirrors and telescopes whose role is crucial, but un-edifying. It bears mentioning that the AOM efficiency improves with the use of a smaller beam. By minimizing beam size and carefully optimizing all geometric aspects of the cat's eye system, the double-pass efficiency can approach 75%. Since our injection-locked master-slave system provides plenty of power, we have been content with about 65%.

7.2.2 Lasers at the beamline

The theoretical basis for laser cooling is described in Chapter 3. For transverse cooling, we use laser light detuned from the transition by approximately one linewidth.

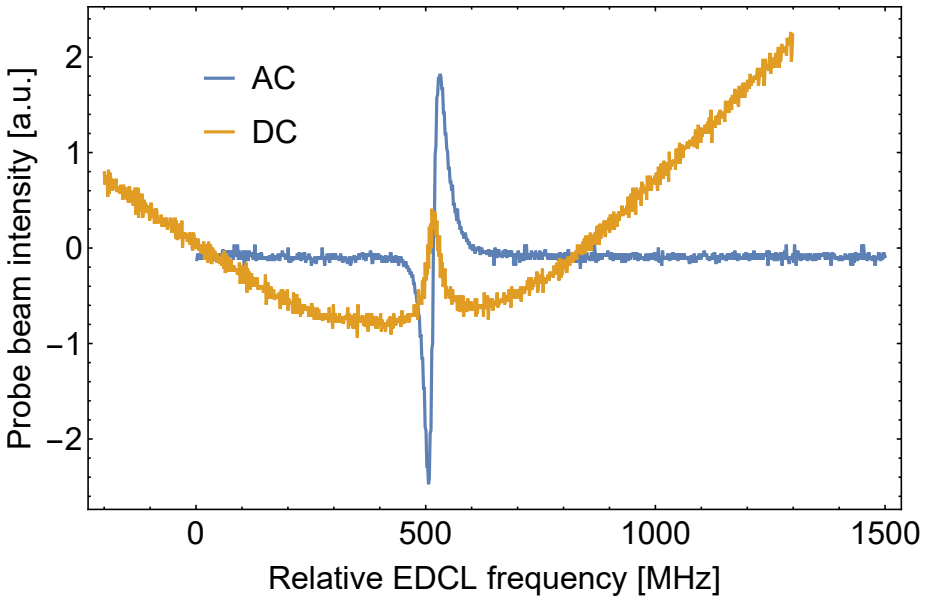

Figure 7.9: Oscilloscope traces from Doppler-free laser frequency stabilization. In the DC signal, the bottom of a Doppler-broadened absorption curve is shown. Slightly to the right of its minimum, a sharper Lamb dip appears. The DC signal is greatly amplified here for clarity, and both signals are the result of a long integration. The SNR of the AC signal is very large compared to the DC. Also advantageous is the fact that the AC signal crosses zero almost exactly 40 MHz below the desired transition, which makes PID-assisted control very simple.

We use a cylindrical telescope to elongate the beam in one dimension. This increases the interaction time between the cooling field and the atoms to around 50 μs, which is enough for approximately 2000 scattering events. The beam is split into a vertical and horizontal component using a 1" PBS (Figure 7.12). Each beam passes through a set of viewports in a 6-way-cross vacuum chamber section. Mirrors reflect the cooling beams back along the same path. The four beams meet at the axis of the atom beam, reducing the transverse velocity spread and collimating the beam. Optimizing the angles and positions of these cooling beams can take quite some time, but doing so successfully makes a remarkable difference in our final beam temperature.

The chirped longitudinal cooling is depicted schematically in Figures 7.13 and 7.14. The beam is shifted by approximately 750 MHz, with an additional saw-tooth modulation that sweeps the detuning through approximately 50 MHz (from more red-detuned to less) in 40 μs. The sawtooth waveform is produced using a function generator triggered by the EL valve driver with a fixed delay. It is fed into an amplifier

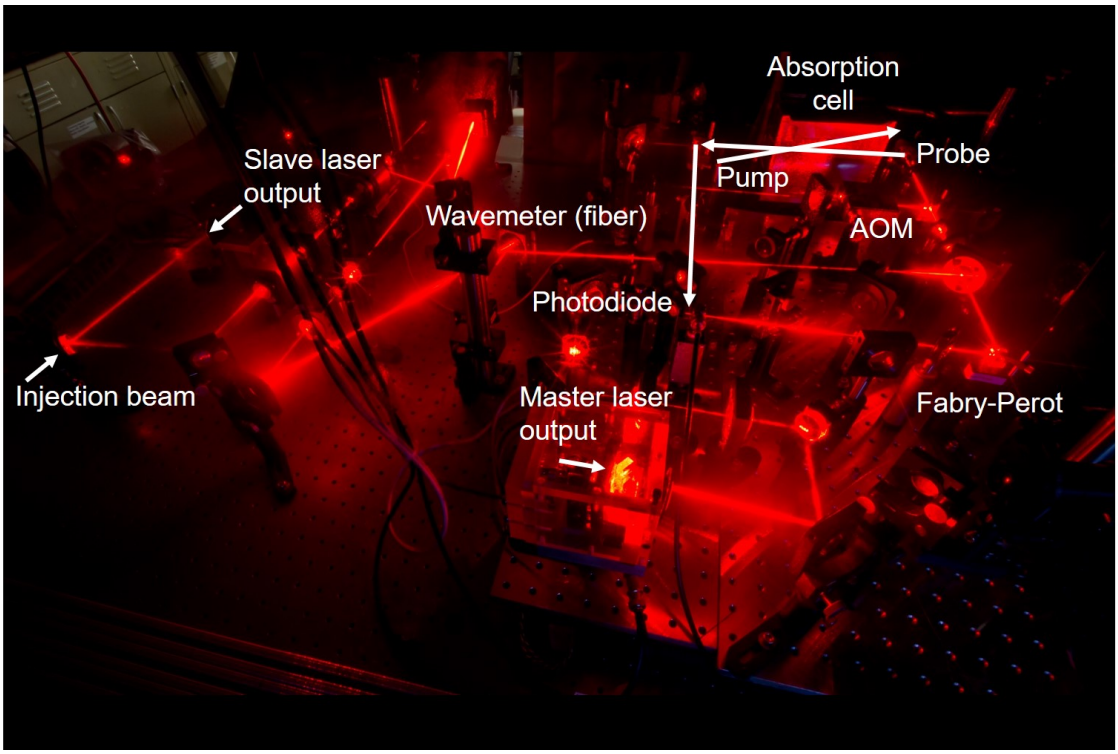

Figure 7.10: Photograph of the master and slave lasers and the saturated absorption cell.

and thence into the voltage-controlled oscillator that drives the AOM. As described in Chapter 3, the linear frequency sweep acts as a velocity-space "shovel," slowing fast atoms and piling them all into progressively slower velocity classes. While the theoretical final result is not as cold as the one from a proper optical molasses, this chirped cooling is an effective and easy way to improve the beam flux.

Taken together, the laser cooling beams achieve a flux improvement of between one and two orders of magnitude. We estimate transverse and longitudinal temperatures of 2 mK and 10 mK, respectively. This is somewhat worse than we would expect from an ideally tuned system, but for our purposes it is entirely sufficient. In the future, smaller apertures may require a return to the optimization process. The transverse beams are oddly temperamental, suggesting that some fundamental problem might undermine their efficacy. Several steps could theoretically be taken to exceed the Doppler limit in the transverse cooling stage [39]. It is also quite possible to implement a bidirectional moving molasses in the longitudinal direction. This would require a

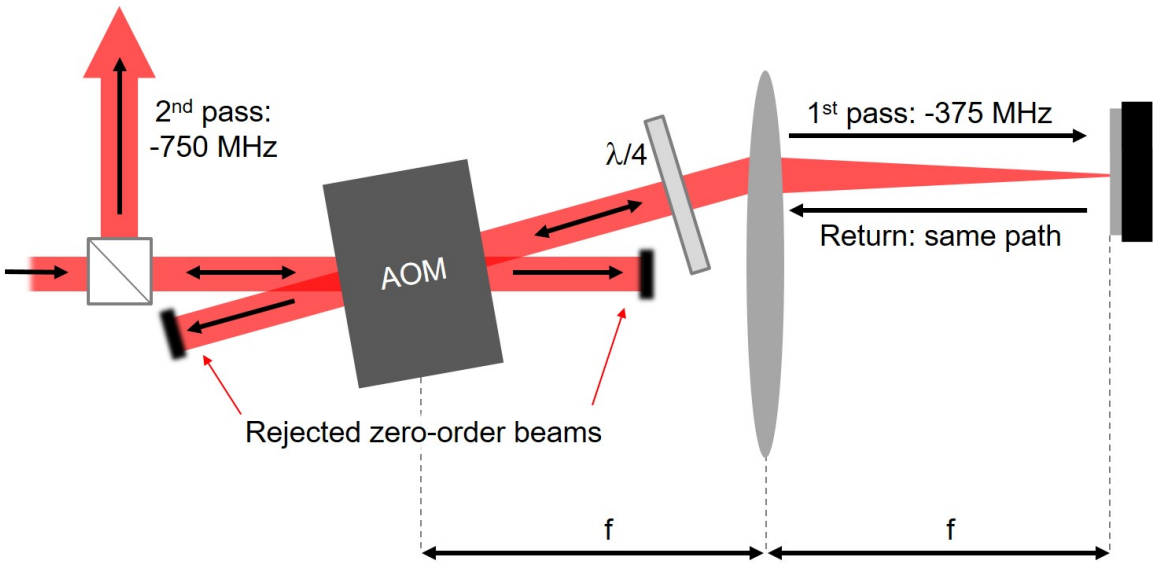

Figure 7.11: Cat's eye double pass configuration for AOM. The standard AOM-mirror system is greatly improved with the use of a lens, separated from each component by one focal length. The incoming beam, moving from left to right, is deflected by an angle that depends on its frequency. The lens collimates this ray, deflecting it into a horizontal trajectory no matter what angle it acquires from the AOM. The lens also focuses the beam, but by placing the mirror one focal length away, the return beam is recollimated. Because this beam also re-enters the AOM at the same angle, it is already ideally configured to maximize the efficiency of a second pass. A waveplate and a PBS redirect the shifted beam towards the experiment. Efficiencies of this system can approach 75%.

second beam with a +750 MHz shift and a rather painful alignment procedure, but no fundamental limits prevent it.

We optically pump the atoms into the $m_J = 2$ LFS state. This requires σ^+ circularly polarized light, which we produce using a PBS and a QWP. The background magnetic field in the pumping region must be aligned with the wave vector of the light. We ensure this condition with three sets of Helmholtz coils connected to low-current Kepco power supplies. It is interesting to note that the lab has a natural background field that points predominantly up, which allows us to pump reasonably well without any Helmholtz coils. Unfortunately, the polarization obtained in this manner is insufficient. We monitor beam polarization using a short section of the Halbach array described in Chapter 5. The array is connected to a linear translator inside the chamber, which allows us to move it towards the beam for measurements

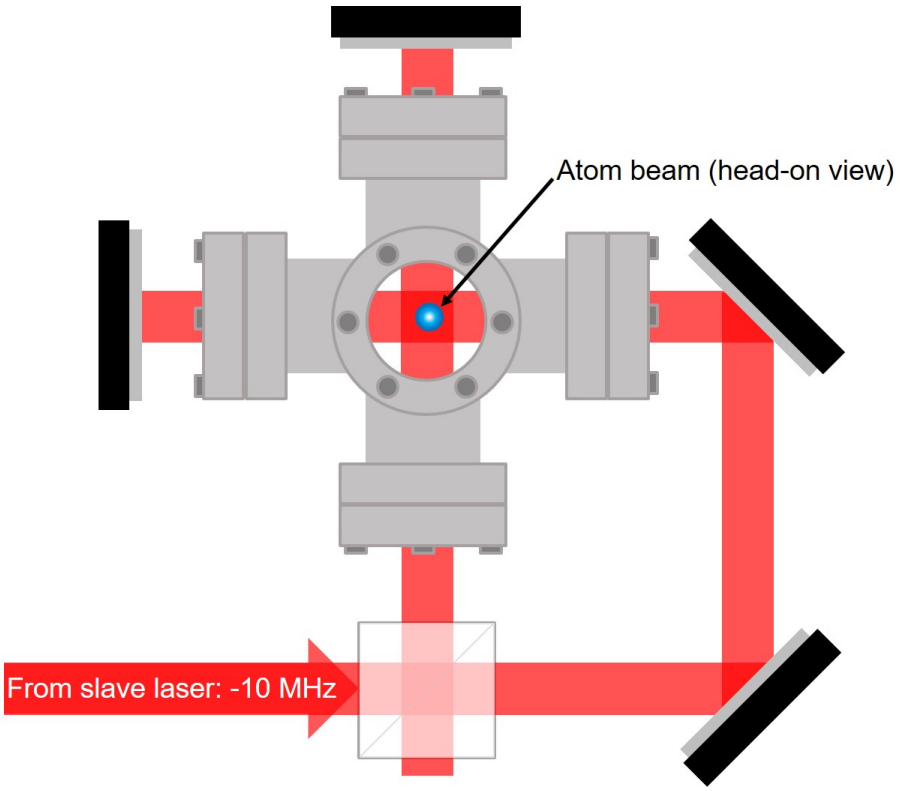

Figure 7.12: Transverse laser cooling, looking down the atomic beamline.

and to retract it otherwise. By monitoring the intensity of the spots corresponding to m_J =0, 1, and 2, we are able to empirically optimize the current in each of the three Helmholtz pairs. Using this method, we achieve greater than 99% magnetic polarization. In our optical pumping, we use 10 MHz red-detuned light near the saturation intensity—more out of convenience than necessity. We have found that setting up our pumping beams in the same manner as the vertical molasses yields slightly better flux (due to cooling) and perfectly serviceable pumping.

7.3 Object plane

The object plane for our lens consists either of a pair of knife edges, which form a slit, or of a brass slide into which are cut shaped apertures. From a ray optics perspective, it is important that each point on our object plane act like a point source. In geometric terms, this just means that the beam must not be so collimated that

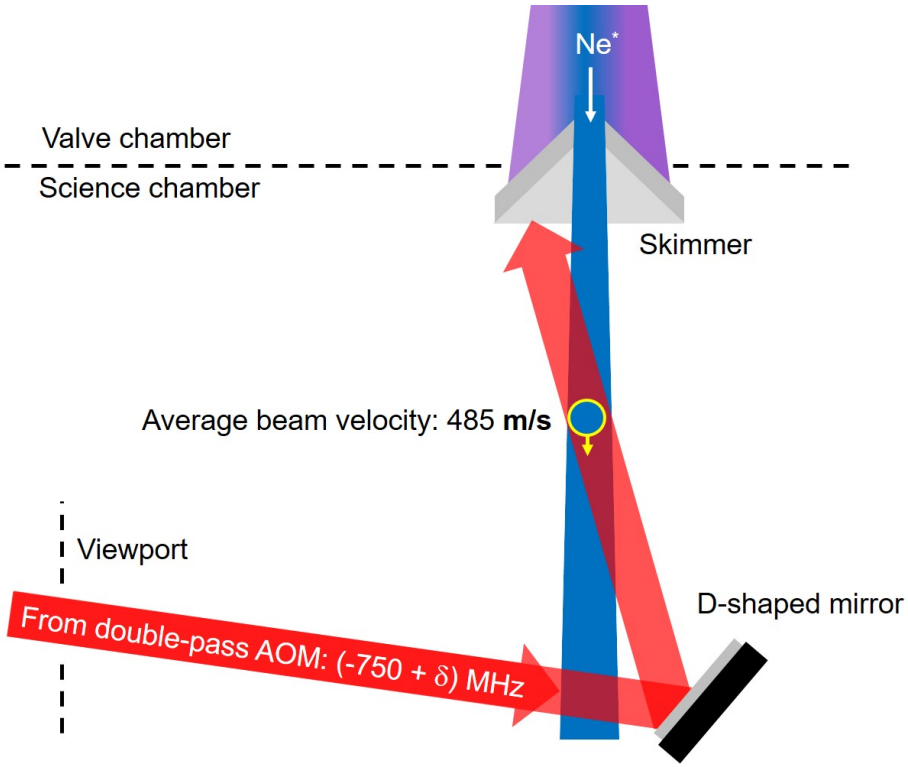

Figure 7.13: Schematic of chirped longitudinal cooling.

the top of the object aperture cannot send atoms to the bottom of the lens aperture. This is a thermal condition on the order of the Doppler limit, so we need not give it another thought. The knife edges are formed with cleaved Si wafers attached to linear-translation vacuum feedthroughs. An earlier version consisted of steel razor blades, but these were discovered to have a permanent magnetic moment—not the best characteristic, given their proximity to our optical pumping. By translating the knife edges individually, we change the width of the slit through which the atoms pass. Translating in concert, we shift the position of the aperture. Both techniques offer excellent quantitative insights into lens performance (Chapter 8). As a first attempt at true imaging, we rotate one knife edge so that it intersects the other at an angle. This forms a vertex whose vertical and horizontal position are independently adjustable. It is an added benefit that the vertex has two-dimensional asymmetry, which provides a qualitative test of true imaging. Finally, the brass slide is attached to one translator and placed in the beam path (Figure 7.15). The translator, which has a range of 2", allows access to all shapes in the slide. It can also be backed off so that the

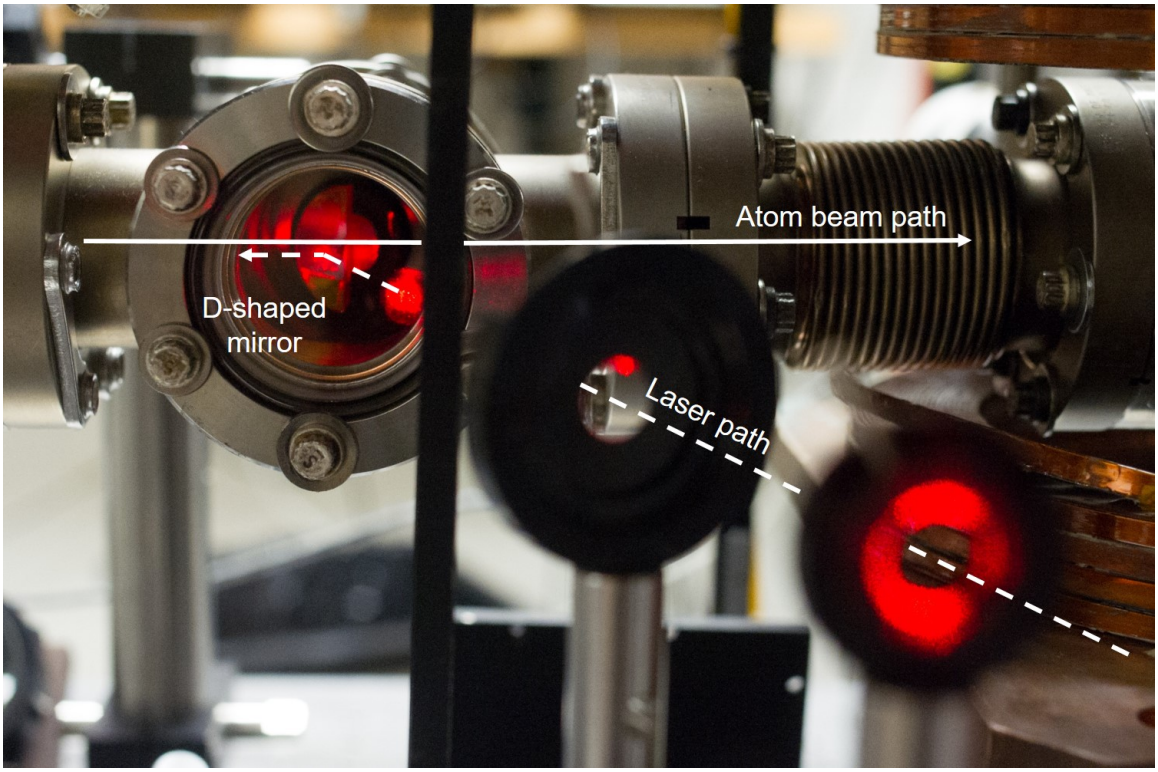

Figure 7.14: Photo of chirped cooling beam entering the vacuum chamber.

slide is removed from the beam path. Edge-welded bellows throughout the vacuum chamber provide sufficient freedom of motion for vertical position adjustments.

The shapes cut into the slide have dimensions on the order of 1 mm, with features as small as 75 μm. Though brass is not the best vacuum material, it is quite soft and easy to work with. Because the slide is so small, priority was given to machinability. To our knowlede, the material choice has not caused any vacuum problems.

7.4 Propagation and phase space evolution

As in optics, the distance between the object plane and the lens has important implications for the image. Because we want to eventually work at short focal lengths and produce highly demagnified images, we selected a moderately long propagation length of 1.35 m. On the face of it there is little to say: this section of the experiment consists of a long vacuum tube. However, this is an opportunity to discuss the adiabatic following and spin flip question we introduced in Chapter 4. We showed

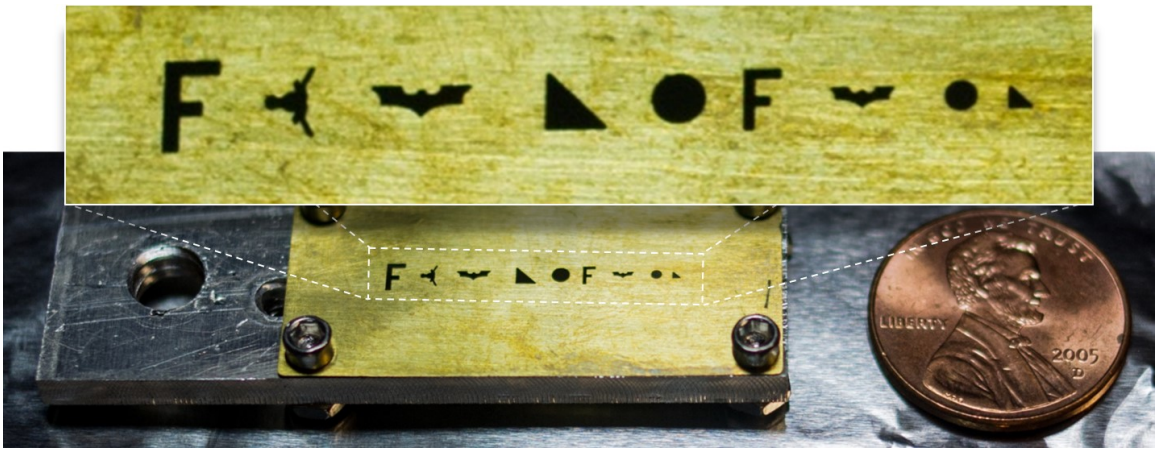

Figure 7.15: Photograph of the slide used as an object for the focusing experiment. The atom beam passes through shaped apertures, just as in an optical transmission mask. The goal of the atom lens is to refocus the beam and reproduce the original shape. The letter F is an excellent object for early investigations, since it is asymmetric in two dimensions and has a simple, recognizable structure. For more advanced tests, shapes like the Texas Longhorn offer more detail and a broader range of size scales. The Batman logo, which is objectively cooler-looking than the version in Chapter 6, is included primarily to impress members of the opposite sex.

mathematically that atoms in a given magnetic eigenstate would stay there, provided the change in field direction was slow compared to the Larmor frequency. Unfortunately, this implies that any sections of the beamline at which the field vanishes could act as depolarization zones. We observe exactly this, despite simultaneously observing an average lab background field of around 3 G. To reduce spin flips, we pass a small current (0.3 A) through a loose solenoid wound along the beamline (Figure 7.16). This maintains the quantization axis, but produces no discernible field gradient. Unfortunately, this wire alone is not entirely sufficient. Using the retractable Halbach array to monitor polarization, we observe a time-dependent fluctuation that persists even with our added background field. These odd spin-flip episodes are only completely eliminated by placing a 1/2" x 1" NdFeB rare earth magnet against the wall of the chopper chamber, generally at a slight angle. It is unnecessary to record the language we used in the lab while investigating this phenomenon. Based on the solution, we suspect the chopper chamber may shield external fields.

It is worth making note of the phase space evolution of the beam at this stage, since doing so provides another example of Liouville's theorem in action. If we assume

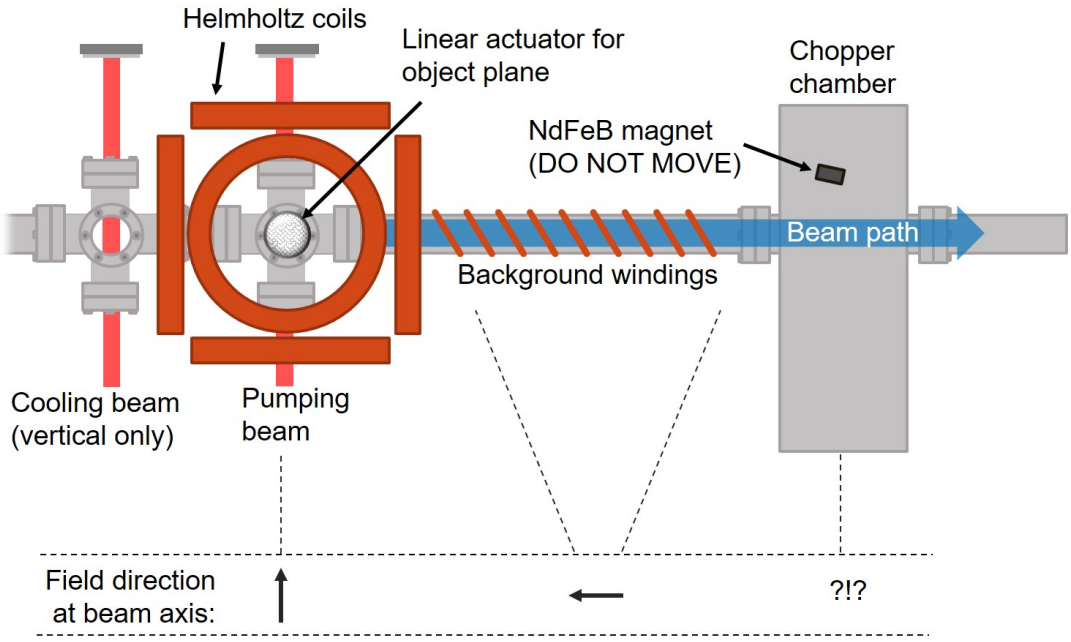

Figure 7.16: Diagram of the beamline midsection. The beam travels 1.35 m from the object plane to the lens. The most important task during this period is to maintain a quantization axis, which prevents spin flips. There is a well defined field at the pumping stage, established by the Helmholtz coils. We add a loosely wrapped wire along the beam to maintain a field between the object and the chopper. The field inside the chopper chamber appears to vary in time, occasionally passing through zero and causing large depolarization episodes. This is prevented by the placement of a large, strong rare earth magnet against the side of the chamber.

the beam starts out uncorrelated in phase space, we can model its evolution over the ensuing trajectory. After traveling a certain distance, the velocity differences in the initial beam begin to take effect. Specifically, the fastest atoms eventually end up at the front of the beam. This is represented in Figure 7.17. Liouville's theorem works in our favor this time, since it ensures that whatever phase space density we started with will remain constant as the beam propagates. Provided we can produce—through some combination of cooling and trapping—the phase space density we need at the beginning of the beamline, we can be confident that it will remain constant downstream.

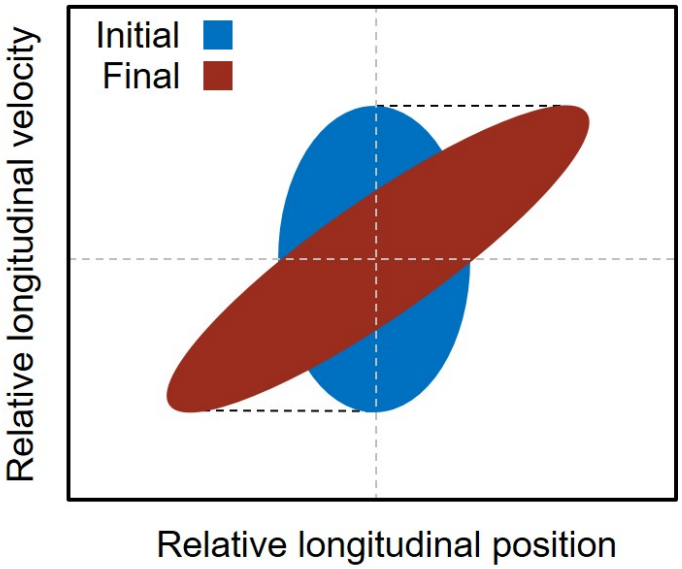

Figure 7.17: Phase space diagram of the beam before and after propagation. As faster atoms move towards the front of the bullet, the beam becomes correlated, though it occupies the same volume.

7.5 Chopper

The pulsed lens requires a similarly pulsed beam. Longitudinal cooling shortens the atom bullet to around 5 cm, which is similar to the length of the lens itself. Since we need the bullet to remain inside the lens throughout the lens pulse, we must shorten the bullet. We do this with a mechanical chopper. The wheel is made from 0.010" thick stainless steel. Its diameter is 13.5". A 0.12" (3 mm) slit at the edge of the chopper allows atoms to pass for a brief period every cycle. The chopper is powered using a brushless DC motor (MOOG BN34HS-25AN-02LHE) connected to a water-cooled ferrofluidic rotary feedthrough. The motor is rigidly mounted to the chopper chamber with 1"-diameter steel stock, which reduces vibration and prevents a variety of catastrophic failure modes. We run the chopper at 165 Hz, which shortens our atomic bullet to a length of 1 cm (δt = 21 μs). For balance, the 3 mm slit actually appears twice in the wheel, since doing otherwise would cause a rotational imbalances. Because our timing precision is quite capable of it, we add another set of slits with a width of 1 mm. These allow us to cut the beam down to a length of 3 mm, if desired. A photograph of the mounted chopper wheel appears in Figure 7.18. A second photo

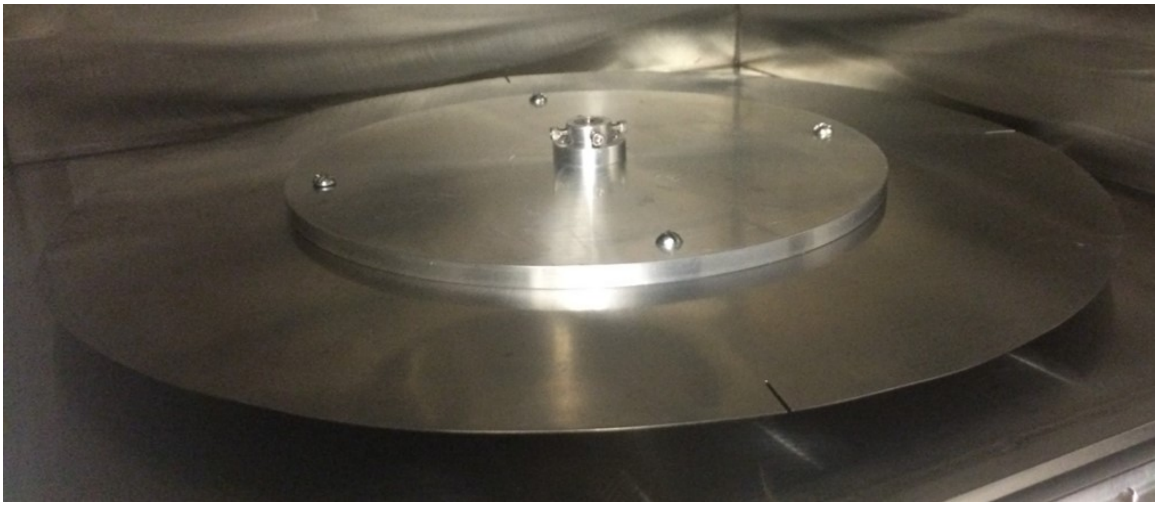

Figure 7.18: Photo of the mounted chopper with a 1 mm slit showing.

showing the outside of the chopper chamber depicts the system's orientation with respect to the beam. The chamber is built from 1/2" stainless steel stock and weighs on the order of 50 kg. This thickness was selected after calculating the rotational energy stored in the chopper wheel, which, for early designs, was equal to the kinetic energy of .50-caliber machine gun round.

Because the chopper is the only component in the experiment whose timing depends on a mechanical momentum, we synchronize the entire beamline to its phase. In other words, the EL valve fires after receiving a signal from the chopper that a slit will open 3.5 ms in the future. All other electronics are synchronized to the valve signal. The chopper may not be a permanent solution to the problem of limiting bullet length. For one thing, the vibration associated with its operation would likely undermine any nanoscale resolution. For another, it is not an especially versatile system. In the future, it would be useful to have the ability to continuously vary the bullet length.

7.6 Lens

The main event in the beamline takes place over the course of 20 μs inside the pulsed electromagnetic hexapole. After the chopper, the bullet has a length of 1 cm and a longitudinal temperature of around 10 mK. The lens aperture reduces the beam's

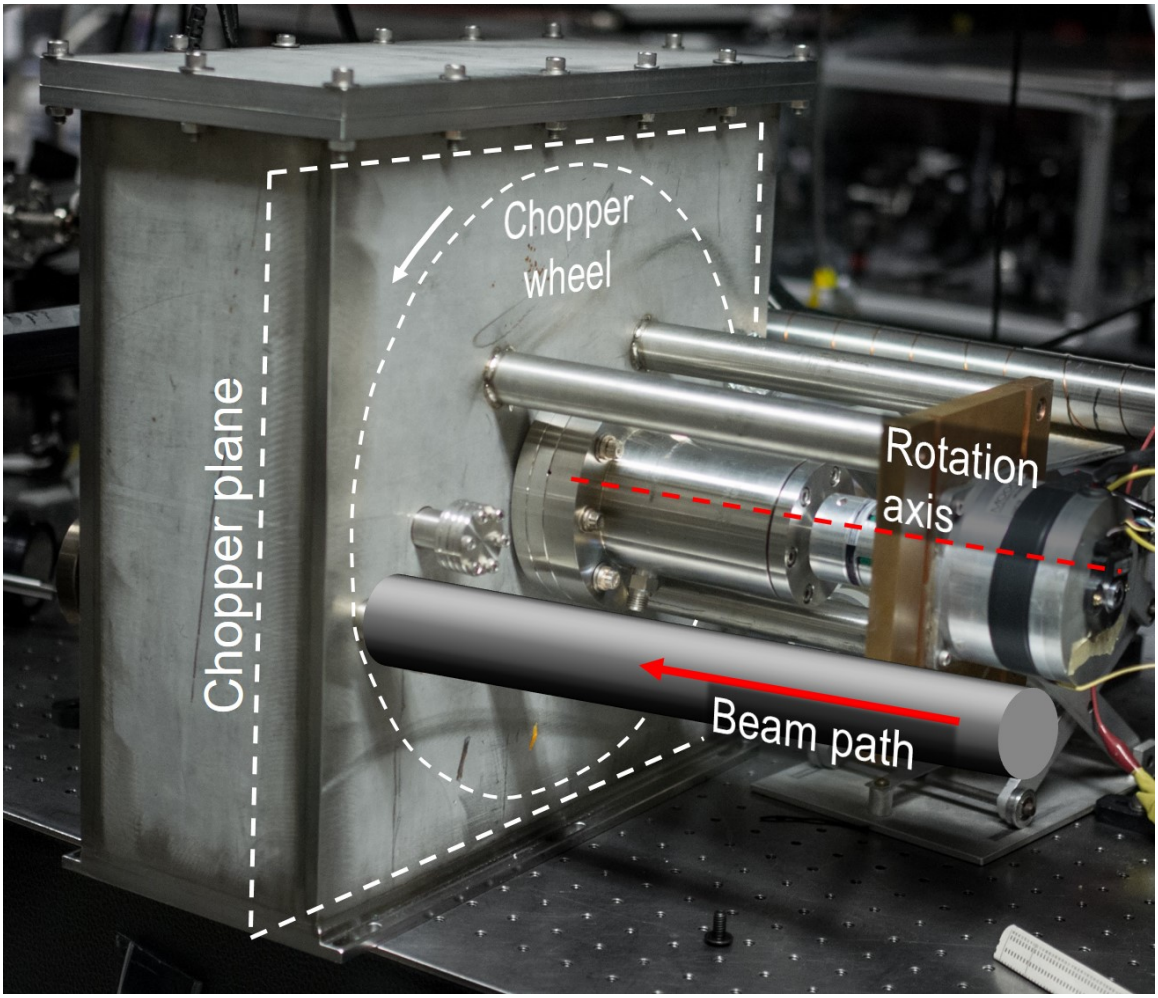

Figure 7.19: Photograph of the chopper chamber with overlays to show the mounted wheel geometry. The beam arrives from the right side of the photo through a tube (digitally added for clarity) that was not mounted at the time of the photo. Slits in the chopper wheel allow short pulses of atoms through the chopper chamber and on to the final stage of the experiment.

cross sectional diameter to 1.5 mm, thereby cutting the transverse temperature to around the Doppler limit. The temperature and dimensions of this bullet are entirely sufficient for a preliminary test of the pulsed lens.

The lens consists of a single wire (Kapton-insulated copper, rectangular cross section, 0.5 mm x 1 mm) wound into a hexapole pattern consistent with Figure 6.6 on page 53 . The wire sections are 5 cm long and sit approximately 2 mm from the beam axis. A photograph in Figure 7.20 shows the lens as it appears in the beamline, though electrical tape and zip ties covering the wire make it difficult to immediately see the geometry. An explanatory drawing overlaid with this photo shows the geometry of the wire underneath the electrical tape. The wire rests against a hollow cylindrical Vespel frame (inner diameter 1.5 mm), which also acts as a section of the vacuum chamber. The ends of the Vespel cylinder have an outer diameter (OD) of 1/2". The center section is machined to an OD of 5 mm. Grooves in this narrow section of the Vespel—visible in the photo, but not in the drawing—facilitate accurate wire placement. The grooves are set into the cylinder with a slight taper, but that feature is not used for the focal lengths discussed in this thesis. The lens wire is looped somewhat unscientifically between consecutive sections. The only intentional aspect of this looping method is to restrict stray fields to regions far away from the beam axis. Further reduction of the stray fields is attempted by shielding the routing loops with μ-metal, though it is not clear whether this has any effect. The wire routing method is not crucial, since the current is only pulsed when the atoms are inside the lens. However, designing a more stable routing system than the haphazard method in the photograph is a goal for the next-generation lens under development.

The 1/2" diameter ends of the Vespel cylinder are connected to vacuum flanges (CF 2.75") using Swagelok hardware. This forms a surprisingly good seal, and allows vacuum pressures on the order of 10^{-7} Torr on the lens side of the vacuum chamber. The pumping hardware used on this side varies depending on the image plane, but generally consists of two turbomolecular pumps with a combined pumping speed on the order of 400 L/s. The long, narrow tunnel through the Vespel cylinder creates a significant differential pumping problem, which we mitigate by connecting a 30 cm hose (CF 2.75") between the detection chamber and the chopper chamber. The CF flanges connected to the Vespel are bonded to each other with welded 1/2" steel rods. This ensures rigidity and prevents bending of the lens tube. Because the detection chamber and the lens position must be adjusted periodically, these rods are extremely

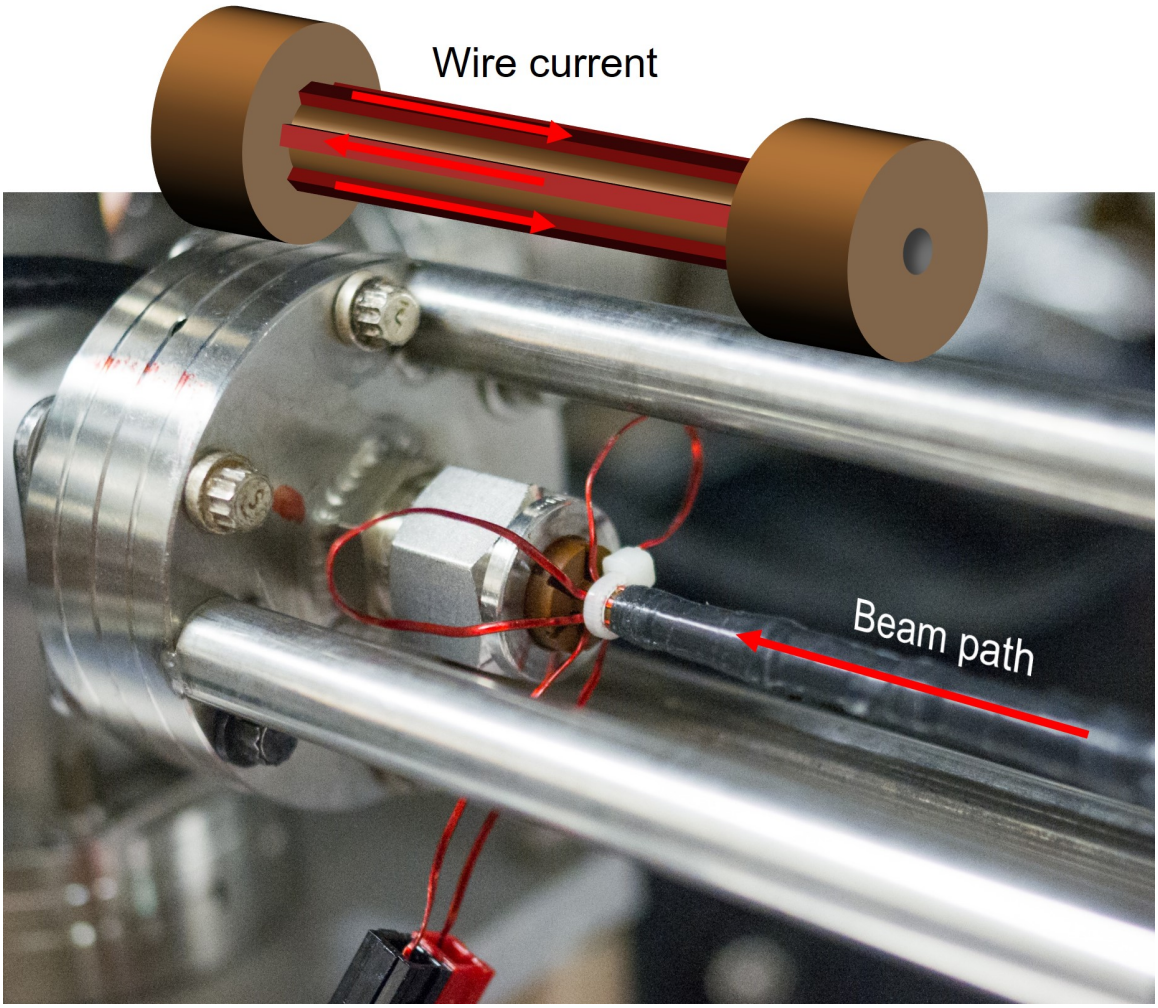

Figure 7.20: Photo with explanatory drawing showing one end of the lens where it attaches to the vacuum chamber.

useful. The results section will not include a discussion of "magnetic focusing using an awkwardly warped hexapole," but this omission is not for lack of data.

A bent Vespel tube is the least frustrating of the many problems we encountered while refining the hexapole frame. The first attempt was based on epoxy and precision-machined CF flanges; it never held vacuum. The second version—which lasted for two years—is shown in Figure 7.21. In this design, a 1.5 mm OD glass tube holds vacuum between two 1.33" CF flanges. A tortoise-shell Vespel frame holding the Hexapole wires surrounds this tube. The whole system is held in place with a se-

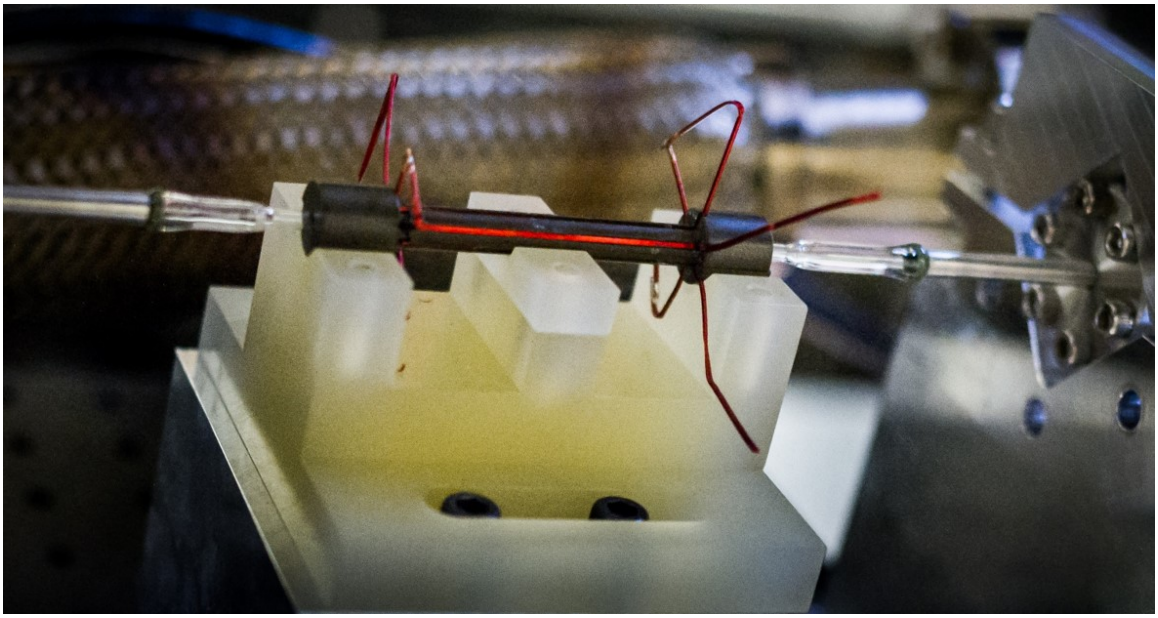

Figure 7.21: An old version of the lens frame, associated mainly with the sounds of breaking glass, weeping, and gnashing of teeth.

ries of firm-but-gentle clamps. As might be expected, all members of this experiment are now familiar with at least half-a-dozen ways to break small glass tubes.

The robust design of the current lens is quite useful, since the first task following installation is alignment. This involves placing an MCP into the beam beyond the lens (usually around 10 cm) and manually adjusting the chamber angle to maximize the signal in time-of-flight mode. The MCP is then switched into phosphor screen mode, and the lens angle is adjusted to produce as circular a cross section as possible. This helps to ensure that the lens is aligned with the beam axis. Both of these steps involve exerting fairly large forces on the detection chamber and on the CF flanges which hold the lens. The steel rods supporting the Vespel chamber are immeasurably better than the series of clamps we used in the past. In theory, a laser alignment would obviate the imprecise "bump the chamber" technique we use. In practice, our laser alignments have always needed fine tuning. Improving the ease and accuracy of the lens alignment process is another priority for future lens designs.

The electronic circuit that produces the lens pulse uses a Powerex CM600DU-24NFH IGBT. This transistor can deliver up to 600 A with timing resolution well into the 10 μs range. We switch it using a Powerex BG2A gate driver, which includes—

among other things—a high-speed optocoupler to protect upstream circuit elements from potential damage. A simplified version of the lens control circuit appears in Figure 7.22. We use a bank of capacitors—equivalent capacitance around 1 mF— to store energy from a Lambda TDK 1500 W power supply. The lens is triggered by an appropriately delayed pulse from the valve. Using a function generator, we produce an inverted square wave with the desired pulse width. The BG2A driver is configured to fire when the input signal drops below a certain threshold. Early versions of this circuit had a problem in which the lens would "stick" open at high voltages. Needless to say, this produced undesirable focusing results, along with enough RF radiation to unlock our laser. We fixed the problem by modifying the BG2A circuit using a method developed by students working on the atomic coilgun.

We measure the lens current by monitoring the voltage across a high-power 1/4 Ω resistor (not pictured) in the driver box. An example of the time-resolved pulse for τ = 33 μs appears in Figure 7.23. While the edges of the pulse are not perfectly square, the current delivery profile is well within design specifications. The negative voltage spike at the end of the pulse is a result of the fast switching inside the driver box, and probably does not correspond to an actual current in the lens. It is interesting to point out that, if it did correspond to a current, this negative spike would not cause any significant problems. Figure 7.24 shows how the lens current varies with applied voltage, increasing quite linearly all the way to the power supply's maximum of 300 V. At this voltage, the lens delivers a robust 1024 A.

For the experiments reported in Chapter 8, we use lens pulses between 20 and 33 μs at voltages between 0 and 80 V. The resulting focal lengths are on the order of 0.5 m, which produces modest-but-measurable demagnification of the object images. The lens pulse time is controlled with 2 μs precision using an analog pulse generator with built-in delay. This piece of equipment is at least 40 years old, but for our purposes it is quite sufficient. In future versions of the experiment, higher precision may be required.

The lens field is supplemented by two sets of elongated Helmholtz coils that provide control over the background transverse magnetic field at the lens axis. This helps mitigate the effects of background fields and improper wire placement. The current in the coils is generally below 0.4 A, producing fields at the beam axis between 0 and 10 G. The coil current is empirically selected to optimize image quality, as will be discussed in Chapter 8. In future versions of this lens, we hope the background coils

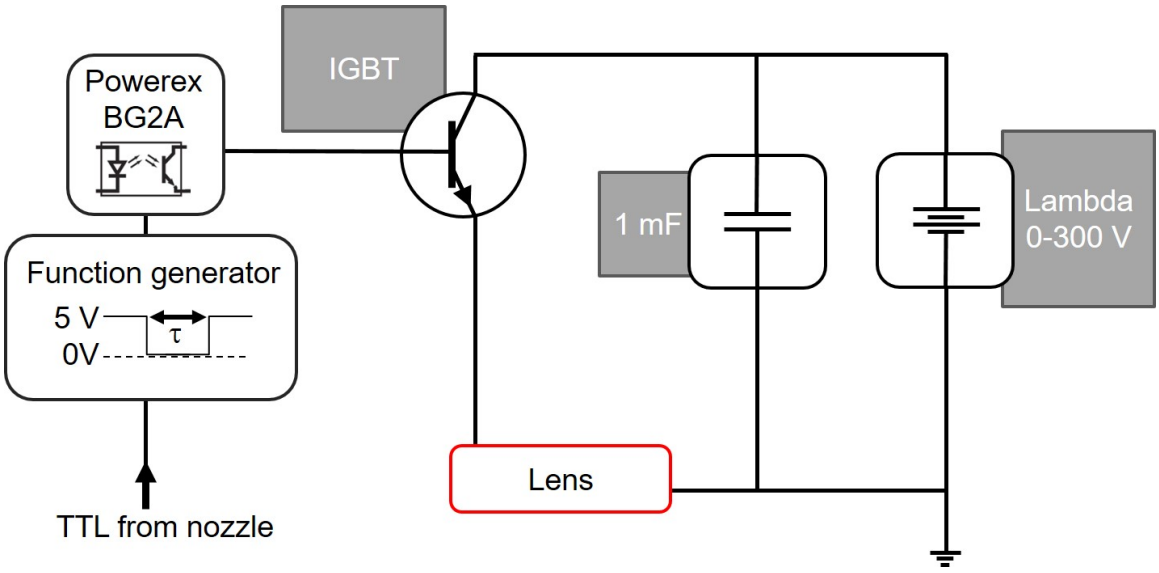

Figure 7.22: Dramatically simplified circuit diagram showing the lens electronics.

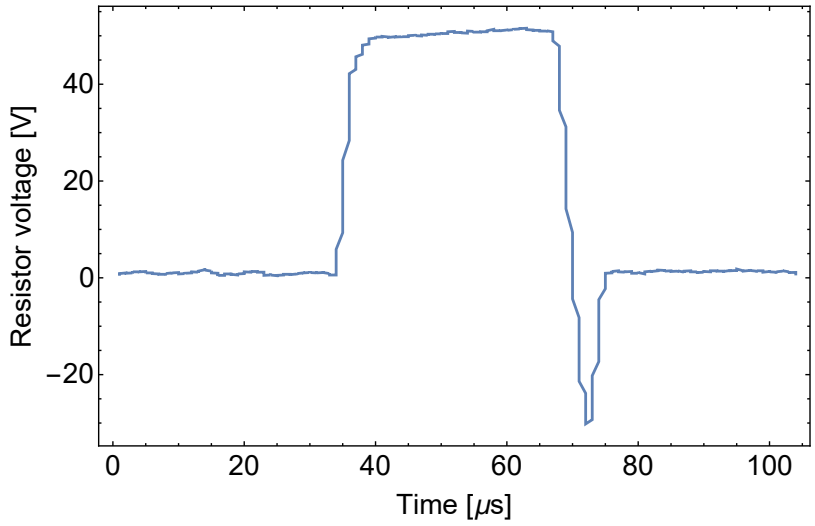

Figure 7.23: Time-resolved oscilloscope trace showing the voltage across a 0.25 Ω resistor for a 33 μs pulse. For this plot, 62 V are applied across the capacitor bank.

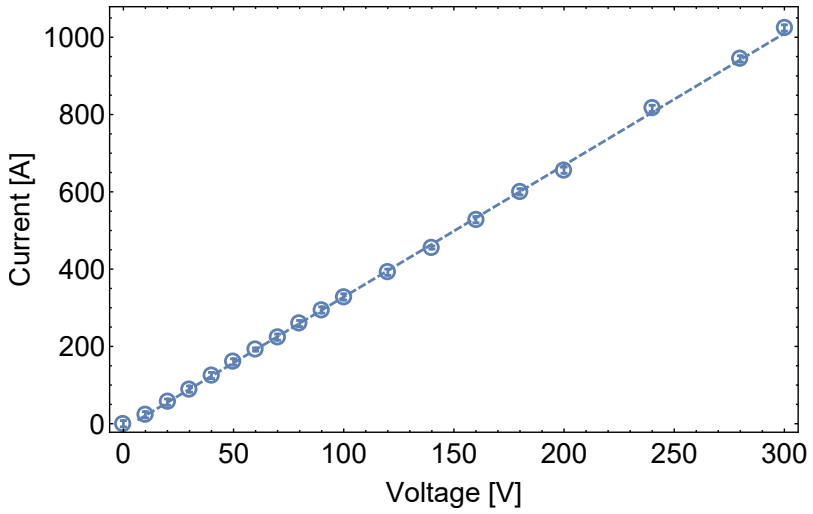

Figure 7.24: IV curve showing the peak current through the lens as a function of the voltage on the capacitors.

will be rendered unnecessary by improved magnetic shielding and an adjustable wire positioning system.

7.7 Detection

We detect the metastable atom signal with a BOS-18 microchannel plate (MCP) from Beam Imaging Solutions. The MCP comprises an array of electron multiplier tubes, 10 μm wide and separated by 15 μm. The tubes—or channels—are held at a front-to-back potential of around 1 kV. They are parallel to each other but arranged at a slight angle with respect to the normal vector. This angle helps ensure that incident atoms will interact with the channel walls, where they produce a cascade of electrons in the strong electric field. While ground state atoms do not trigger an electron cascade, other beam components—including ions and UV rays—certainly can. Thanks to the many magnetic fields in the beam and to the chopper, we are confident that our signal is produced almost entirely by Ne*. Arriving at the back plate of the MCP, the electron current can either be collected and measured (time-of-flight mode; ToF) or accelerated towards a phosphor screen (imaging mode).

Collecting the current without using a phosphor screen provides a time-resolved flux measurement, but no spatial information. The electron current is converted into a

voltage, which is then read with an oscilloscope triggered by the valve synchronization pulse. This technique is quite useful when we need a quantitative metric with which to optimize laser cooling. It also provides a sensitive, fast detection tool during lens alignment, which requires attention to faint, transient signals. Beyond diagnostics, however, the ToF measurement is not very useful to us. For one thing, we have found that the time constant of the detection system is on the order of 30 μs, which is longer than our bullet pulse. Because of this, meaningful time-resolved measurements of our system are not possible. More importantly, ToF mode discards all spatial information. This is unfortunate, because the beam cross section is literally the main thing we wish to investigate.

Instead of collecting the electrons at the back plate of the MCP, we can project them onto a phosphor screen using an electric potential on the order of 4 kV. Because the electrons from each channel remain in roughly the same transverse position, this mode of operation provides a two-dimensional picture of the beam's cross section. A diagram of the entire detection setup is shown in Figure 7.25. Atoms from the lens arrive at the MCP and produce an electron cascade. The current is accelerated towards the phosphor screen, broadening somewhat due to charge repulsion along the way. The phosphor responds to the electrons by luminescing. With a viewport in the vacuum chamber and a fast optical lens (a Nikon AF Nikkor 50 mm f/1.8D with a Sigma Life Size macrophotography attachment), we project an image of the glowing phosphor onto a CCD detector (an Apogee Alta U47, manufactured for digital astrophotography). Reading the resulting images with astronomy software (Maxim DL4), we are able to make quantitative measurements of beam flux as a function of transverse position. We calibrate the camera using a ruler and establish a conversion factor of 17.6 μm/pixel. At moderate apertures, the lens system is diffraction limited to spots on the order of 75 μm. It is worth noting that the depth of field of this lens with the macro attachment is fairly narrow. A crucial step in the experimental setup, therefore, is making sure the optical lens is properly focused.

With a gap between the MCP back plate and the phosphor screen of 1 mm, we expect space charge spreading on the order of 100 μm. We have verified this resolution by passing a collimated atom beam through a 25 μm pinhole, obtaining a phosphor screen spot of 120 μm. Naturally, this limit will hinder our characterization of nanoscale images, so future detection strategies will require a new approach. One candidate is knife-edge detection, in which signal attenuation is observed for a knife

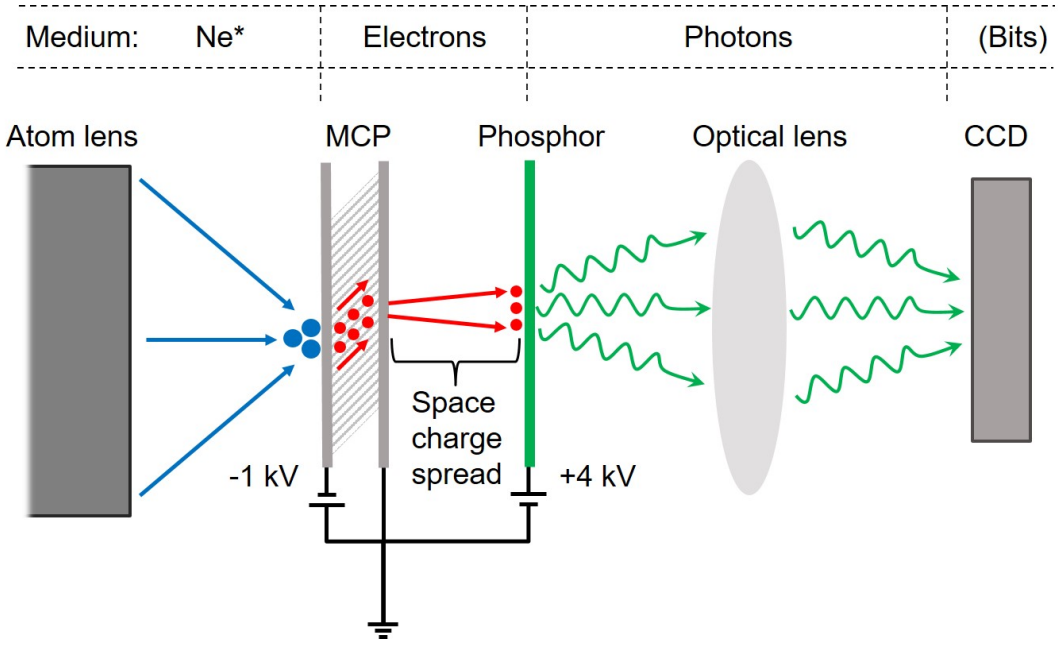

Figure 7.25: A diagram showing the detection technique. Atoms from the lens trigger an electron cascade at the MCP. These electrons can be collected at the back plate of the MCP or accelerated to a phosphor screen. The phosphorescence from the screen is observed by a camera system set outside of vacuum, pointed through a viewport. In measuring the width of our beam, we have to contend with both space-charge spreading of the electrons and the resolution of our optical observation system. The overall spatial resolution limit for the current system is on the order of 120 μm.

edge blocking the beam. This only works for simple geometries, but in principle it should permit measurement of very narrow beams. A more advanced technique would be to use the metastable beam for lithography or direct deposition. This has been successfully demonstrated in pinhole imaging [23, 21].

7.8 Timing

It is worth briefly mentioning the synchronization methods used in this experiment, since timing is such an important factor. Several computer-based approaches were used in early work. Labview provided a perfectly reliable platform. Cicero, a GUI-based suite specifically designed for atom optics, worked even better. Following a computer crash, we "temporarily" resorted to a stack of rather crotchety, 33-year-

old pulse generators (Phillips PM 5715). Despite their age, these boxes performed flawlessly and have been in service ever since.

The timing chain begins, paradoxically, at the middle. The chopper is the only element whose function cannot be triggered on demand, so its index pulse is used as the starter pistol for the rest of the experiment (Figure 7.26). We empirically determine a delay that will fire the valve approximately 3.5 ms before the chopper slot crosses the beam axis. The valve controller fires both the valve and the discharge and produces a synchronization pulse that we send to the rest of the experiment. The chirped longitudinal cooling begins its sweep at 600 μs. The lens fires after a delay of 4 ms. Each of these is adjusted using Vernier scales on the pulse generators with a precision of 2 μs, though this level of control could be improved if necessary.

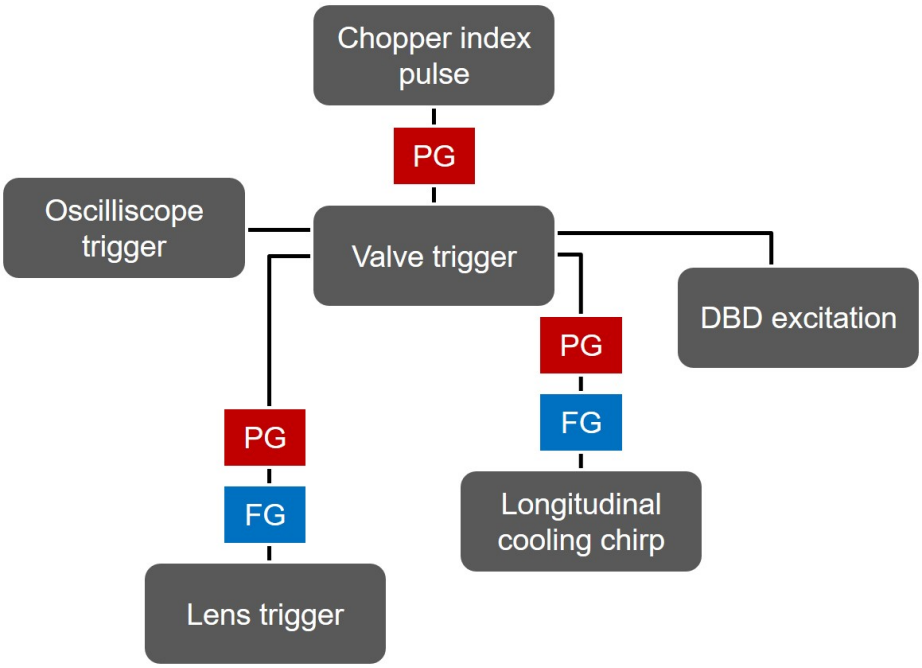

Figure 7.26: A hierarchy diagram showing how the timing trigger propagates through the experiment. The chopper index pulse start the clock. An empirically determined delay, implemented by a pulse generator (PG), delivers a TTL trigger to the valve 3.5 ms before the chopper slit will open. The valve driver box triggers both the valve and the DBD excitation source. A synchronization signal from the valve box is independently sent to the oscilloscope, the chirp, and the lens. In the latter two cases, a pulse generator provides a delay and a function generator produces the required waveform. The vertical position of the tiles in this diagram are vaguely representative of their temporal order, though the distances are not to scale. For more precise timing details, see Figure 7.1.

Chapter Eight: Results

Having constructed the (world's first) pulsed electromagnetic hexapole lens and built a beamline to match, nothing remains but to test it. For the sake of clarity and narrative—and to avoid "burying the lede"—we present our results in slightly non-chronological order.

8.1 Basic results

The simplest experiment we can perform is the focusing of a single slit. Using linear translators connected to cleaved Si wafers, we form an adjustable vertical slit at the object plane. Passing through this aperture, the beam propagates a distance d_o before reaching the lens aperture. For all experiments described in this chaper, $d_o = 135$ cm. When the atom bullet—chopped and cooled as described in Chapter 7—is entirely

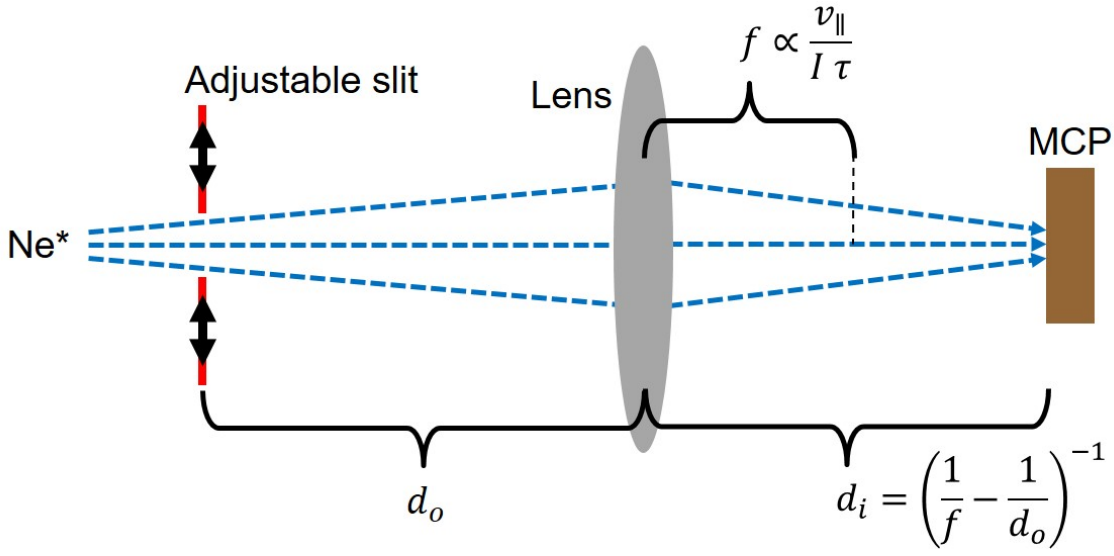

Figure 8.1: Diagram of single-slit focusing with two adjustable knife edges forming the object plane (view from above). Atoms pass through the vertical slit formed by the knife edges and propagate a distance d_o before reaching the lens. The pulsed hexapole field focuses the beam at distance d_i, where an MCP detects the imaged beam.

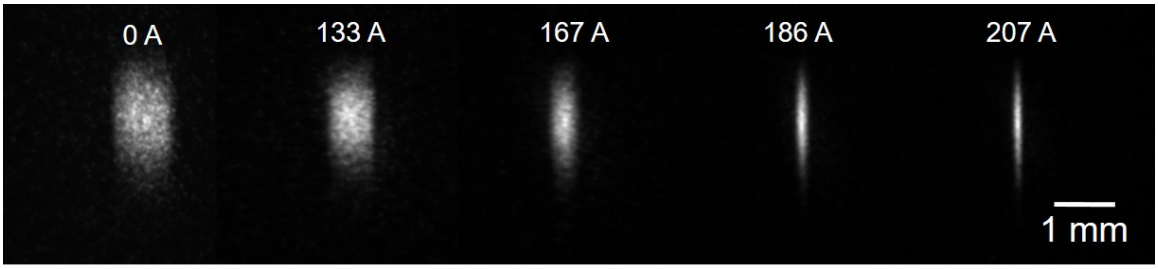

Figure 8.2: MCP images of the beam cross section at the image plane for a range of currents. The slit is blurry at low currents and comes into focus around 207 A. The object-plane slit width for this case is 230 μm; the image distance is 113 cm. Ray optics predicts an image width of 190 μm. The measured FWHM of the imaged slit is 170 μm. Considering the sources of error (see text), these numbers are surprisingly close.

within the lens, a current pulse produces a brief focusing field (Chapter 6). We detect the focused atoms using an MCP/phosphor screen system, which we place a distance d_i from the lens. We monitor the phosphor screen through a viewport using a digital camera connected to a desktop computer. Though we have discussed many similar examples, a diagram of this setup is provided for quick reference in Figure 8.1.

We start by placing our detector at an image distance of 113 cm. If the thin lens equation applies, we expect this d_i to yield a magnification factor of 0.83 $\pm$ 0.02. The uncertainty in this number results from the error of $\pm$2 cm on d_o and d_i, since the lens cannot be localized to a single point. We arrange the knife edges to produce a 230 $\pm$ 30 μm slit at the object plane. We pulse the lens for 25 μs at currents ranging from 0 to over 700 A. Selected CCD images appear in Figure 8.2. At low currents, the beam cross section forms an extended spot. The spot looks somewhat rectangular, but this is largely due to the fact that the slit collimates the beam in the horizontal direction. The spot narrows with increasing current, reaching a minimum at 207 A. Figure 8.3 shows the image size as a function of current for this image distance and for d_i = 87 cm, discussed in the next paragraph. The horizontal full-width-at-half-maximum (FWHM) of the spot at I = 207 A and d_i = 113 cm is 170 $\pm$ 20 μm. Taken at face value, this represents a magnification factor of 0.7 $\pm$ 0.1.

We repeat the same procedure for $d_i = 87 \pm 2$ cm, for which we expect $M = 0.64$ $\pm$ 0.02 (predicted image width around 150 μm). Image width as a function of current is plotted in Figure 8.3. This time, the slit comes into focus at 227 A. A larger current

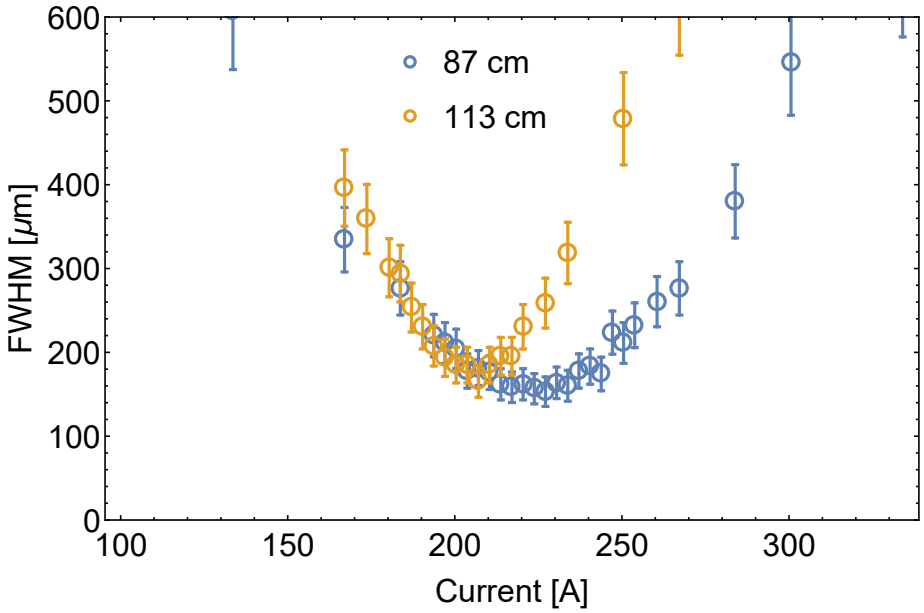

Figure 8.3: Measured image width (FWHM) as a function of current for image distances of 87 ± 2 and 113 ± 2 cm. The width varies smoothly with current in both cases, reaching a minimum when the current produces a focused image of the object plane. Due to requiring a stronger field gradient, the 87 cm image comes into focus at a larger current (227 A) than does the 113 cm image (207 A). The in-focus widths are 150 ± 20 μm 170 ± 20 μm, which compare reasonably well with the expected widths of 150 μm and 190 μm. Unfortunately, the error in the measured numbers is too large to draw any meaningful conclusions.

is appropriate, since the shorter image distance requires a larger focusing force. The imaged slit for this case has a FWHM of 150 ± 20 μm, which gives a magnification factor of 0.7 ± 0.1—the same as in the 113 cm case.

The large uncertainty in these measurements stems in part from the fact that the expected spot size is very close to the 120 μm resolution of the MCP. This makes it rather difficult to determine how much of the measured width is "real" and how much is added by our detection equipment. Additionally, the image brightness is not uniform. Where we would hope to observe a flat-topped intensity curve with clear edges, we instead see a rather Gaussian peak function. Another source of error is the knife edge calibration, which is accomplished by closing the silicon wafers around a slab of aluminum with known thickness. This procedure could be improved—for example, using a laser and a beam profiler—but the vacuum hardware surrounding

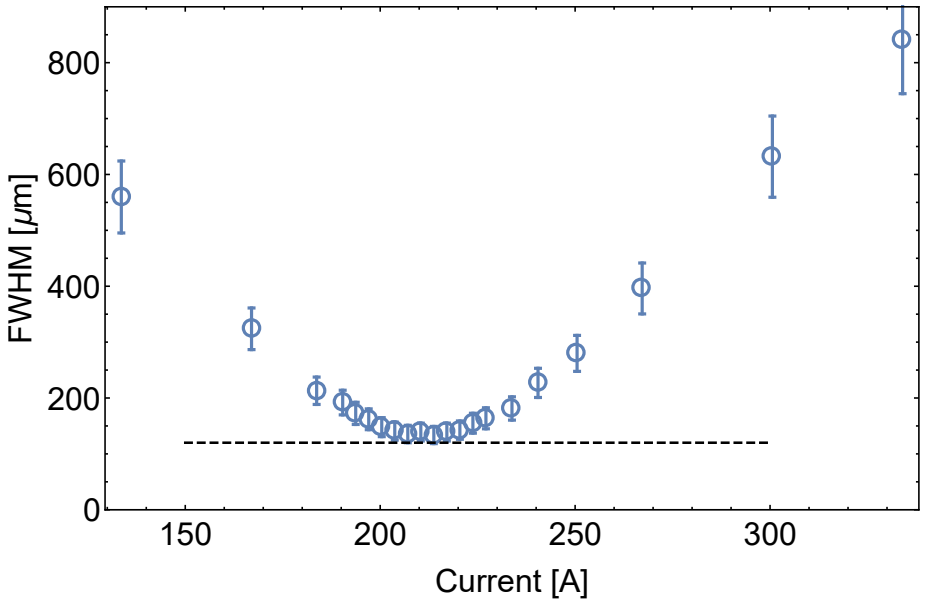

Figure 8.4: Measured image width (FWHM) as a function of current for an image distance of 61 ± 2 cm. As in Figure 8.3, the FWHM varies smoothly with current. The focused image width is 130 ± 20 μm, whereas we expect 100 μm. This disagreement—as well as the error in the other numbers—stems largely from the 120 μm resolution of our MCP/Phosphor-screen/camera detection chain.

the object plane makes such a measurement quite inconvenient.

The same sources of error become more serious at shorter image distances. Placing the detection plane at 61 ± 2 cm yields a focused image of 130 ± 20 μm. For reasons that will become clear later, the lens pulse for this case is lengthened to 33 μs. With this longer pulse time, the slit comes into focus at 214 A. The image width as a function of current is plotted in Figure 8.4, from which it is apparent that the image size comes very close to the resolution limit of the detector (represented by a black dotted line). The expected spot size for this case is 100 μm, which would lead to a magnification factor of 0.45 ± 0.02. Instead, we calculate $M = 0.6 \pm 0.1$.

Clearly, we need to address the large uncertainties in these results, along with the systematic error that appears when our expected spot size is smaller than the MCP can resolve. Fortunately, we remembered to make our slit completely adjustable.

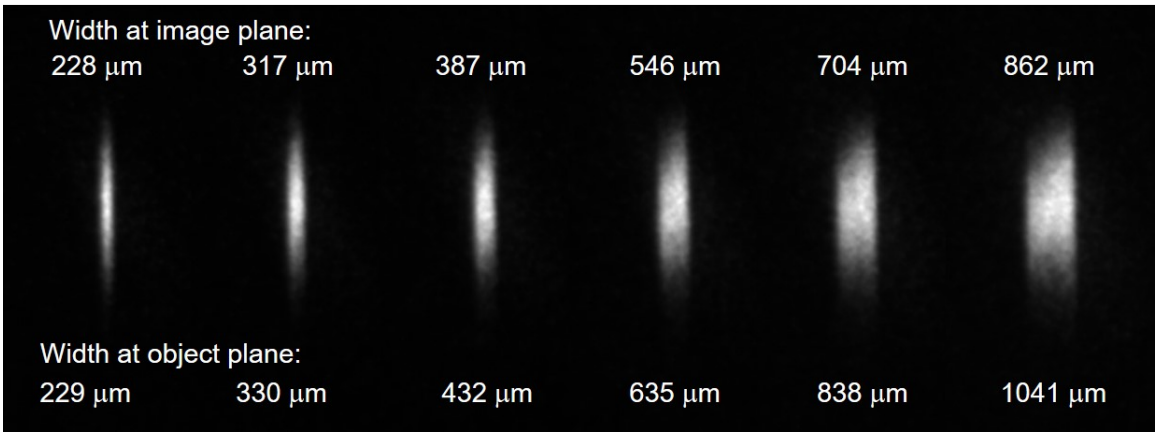

Figure 8.5: A sequence of MCP images showing the expanding slit measurement at 113 cm. As the object plane expands, the width of the focused image grows large enough that the detector's resolution plays a less important role. We further reduce error by fitting a set of data points (Figure 8.6).

8.2 Advanced slit measurements

We now discuss two approaches to reducing the error in our magnification factor measurements. In the first, we expand the aperture and move into regimes where the image size is significantly larger than the detector resolution. In the second, we measure relative changes in the image position, thereby avoiding the problem of width measurement entirely. Both of these approaches have the advantage of producing full data sets, rather than single measurements. Fitting these data sets leads simultaneously to better agreement with theory and to dramatically reduced uncertainty.

Expanding the slit width at the object plane produces a commensurately expanded image, the measurement of which is less hindered by detector resolution. We expect the change in image size to be proportional to the change in object size, where the proportionality constant is simply the magnification factor. Figure 8.5 shows a sequence of MCP images for $d_i = 113$ cm as the aperture expands from 230 μm to just over 1 mm. As the aperture expands, clearly defined edges become apparent in the image. Because of variations in beam brightness, we find that a visual measurement of the image edge is more accurate than a FWHM calculation. We conservatively estimate the error from this procedure to be 4 camera pixels, or 70 μm.

We measure images from an expanding slit at all three focal lengths and plot the

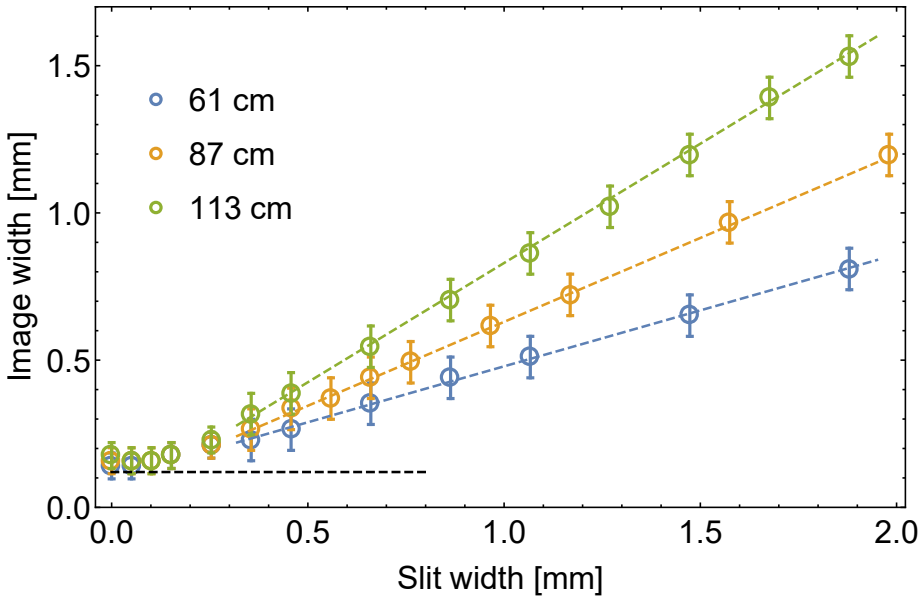

Figure 8.6: In-focus image width as a function of object-plane slit width for all three focal lengths. For small widths, the detector resolution (dotted line) plays an important role. As the aperture expands, the images begin to follow the linear relation that ray optics predicts. The slopes extracted from the data—which correspond to the magnification factors—are 0.38 ± 0.08, 0.57 ± 0.08, and 0.81 ± 0.08. These numbers are in agreement with the theoretical predictions (Table 8.1).

results in Figure 8.6. At small widths, the detector resolution is clearly a problem. For larger images, the linear relationship that we expect begins to dominate. We now have the enormous advantage of being able to calculate the magnification factors using many data points instead of just one. Discarding the measurements for apertures smaller than 400 μm, we fit the remaining data to linear curves. Rather than explicitly including our uncertainty on the aperture widths, we simply allow the trendlines to cross the axes at any point. This is reasonable, since we know the change in width (from vernier scales on the linear translators) to a much greater precision (5 μm) than we know the absolute knife edge separation. The magnification factors from this method are 0.38 ± 0.08, 0.57 ± 0.08, and 0.81 ± 0.08. These values are in agreement with those expected from ray optics, and the uncertainty is lower than before by a factor of two. Nevertheless, these are large error bars: they just barely separate the measurements from one another. We should be able to do better.

Our problems so far have stemmed from the difficulty of measuring image width.

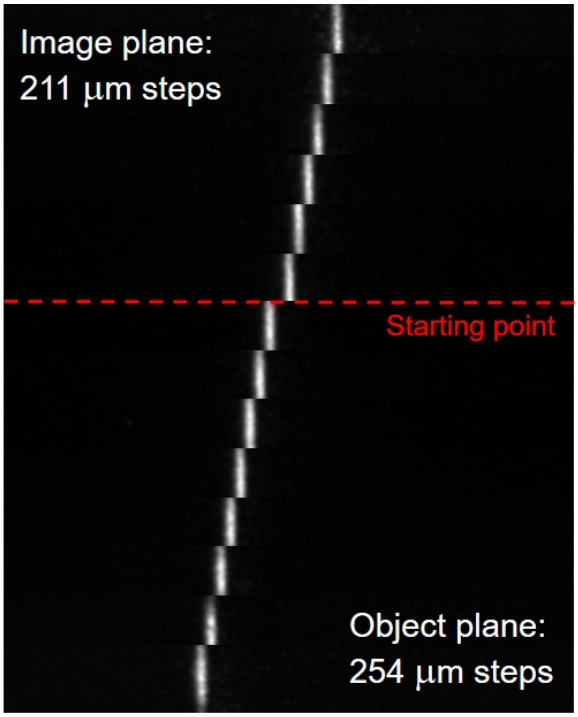

Figure 8.7: Cropped, aligned MCP images of the focused slit at 113 cm as we translate the object-plane aperture position by 10 mil increments. The image shifts by proportional amounts, following a remarkably linear trend (Figure 8.8).

In our third approach, we dispense with this requirement entirely. Shifting the aperture at the object plane should result in a similar displacement of the image. Because we can measure the center of a thin image with excellent precision—within one pixel—we can record displacement with much smaller uncertainty than we can record width. Figure 8.7 shows a series of images (cropped for efficiency) obtained at $d_i = 133$ cm by repeatedly shifting the object aperture in 10 mil (254 μm) increments. This sequence is surprisingly linear over a large range. Figure 8.8 shows data obtained by this process for all three focal lengths. Considering the 1.5 mm aperture of our lens, it is somewhat remarkable that the linear relationship in these plots holds for a range in excess of 3 mm. Fitting the data as before, we obtain magnification factors of 0.42 $\pm$ 0.01, 0.63 $\pm$ 0.01, and 0.83 $\pm$ 0.01. These numbers actually have lower uncertainty than our theoretical values, and in many ways they are likely more accurate.

The results from all three trustworthy methods—that is, the geometrical calculation, the window expansion, and the slit translation—are reported in Table 8.1. The

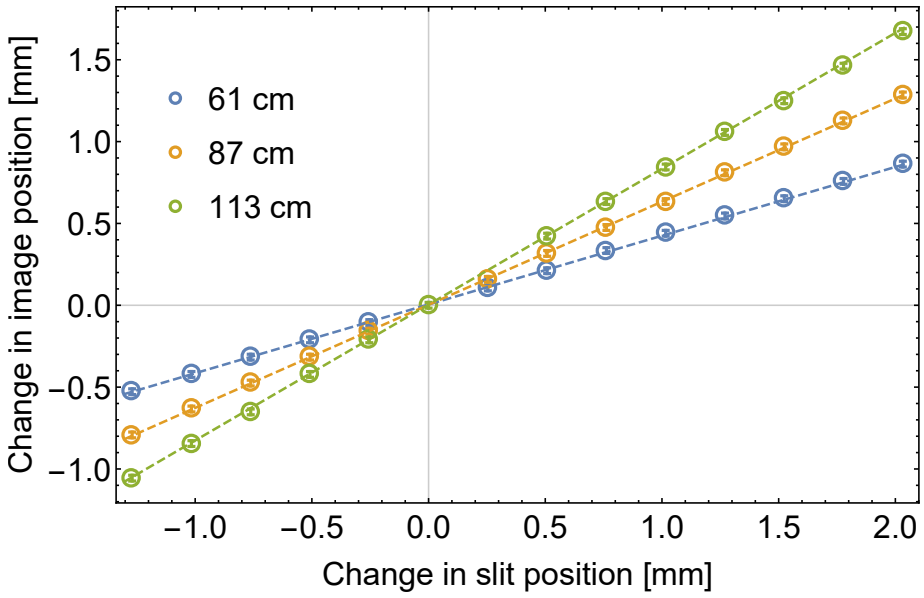

Figure 8.8: Data obtained by shifting the object-plane aperture in 10 mil increments. The linear relationship, which corresponds to magnification factor, is apparent at all three focal lengths. The slopes obtained by fitting these data sets are 0.42 ± 0.01, 0.63 ± 0.01, and 0.83 ± 0.01. These values agree with and have lower uncertainty than the theoretical predictions from ray optics.

factors obtained from our naïve, single-data-point calculations are not included in the table, since we can now recognize them as markedly inferior. The results in this section show that our atom focusing system is—at least in some ways—capable of acting like a traditional optical lens. By changing both the size and the position of a single slit, we measure magnification factors in surprisingly good agreement with the predictions of ray optics. But single slits are not the waters in which a lens was meant to sail! We cannot declare our system seaworthy without a providing a demonstration of true imaging.

Table 8.1: Magnification factors calculated for three focal lengths using three different methods.

Image distance:	61 cm	87 cm	113 cm
Thin lens equation:	0.45 ± 0.02	0.64 ± 0.02	0.84 ± 0.02
Aperture expansion:	0.38 ± 0.08	0.57 ± 0.08	0.81 ± 0.08
Aperture translation:	0.42 ± 0.01	0.63 ± 0.01	0.83 ± 0.01

8.3 A little bit effy

At this point it makes sense to step back and briefly discuss the chronological development of this project. The results described above are the fruits of a long optimization process; in fact, they are most recent measurements we have. Various earlier incarnations of our beamline led to much less presentable data, of which we shall report very little.

Our first design included the magnetic mirror described in Chapter 5, whose role was to separate the $m_J = 2$ LFS atoms from the rest of the beam. This made beam alignment both difficult and unreliable. The lens during this time was formed by clamping a Vespel frame around a glass tube (Figure 7.21 on page 92). As long as the glass did not break, this worked acceptably. Unfortunately, it meant we had to exercise extreme caution while re-aligning the lens. Because the magnetic mirror polarization was so unreliable, re-alignments were regrettably frequent. Another problem during this time was with atom beam quality. We were using crossed-diagonal laser cooling beams to form a moving molasses, cooling the atoms simultaneously in the longitudinal and horizontal directions. We pumped only a narrow slice of the atoms into the $m_J = 2$ state, pumping the rest into m_J = -2 and separating the species with the mirror. We hoped this would be sufficient to produce a cold, short atomic bullet at the lens, but it never was. On our best days, the bullet was still longer than the lens, forcing us to operate in DC mode rather than pulsed. The valve was consistently inconsistent, working fine one day and not at all the next. The lens driver only worked at low voltages, and even then it was noisy enough to self-trigger and—often as not—to unlock our laser system. Despite all of these problems, we were able to demonstrate primitive hexapole focusing. By December of 2014 we had focused the image of a pinhole to a spot of around 300 μm. The spot was not quite circular, and it did not focus with the current we expected, and—because of our valve problems—we could only produce it around 40% of the time; nevertheless, it was a spot.

Having proven that our version of hexapole focusing was not doomed to complete failure, we set out to fix the myriad problems that prevented us from producing better results. One of us escorted the misbehaving Even-Lavie valve on a pilgrimage to Israel, where Dr Uzi Even himself—through some combination of intuition, bravado, and intimidation—coaxed his creation into compliance. We dispensed with the magnetic

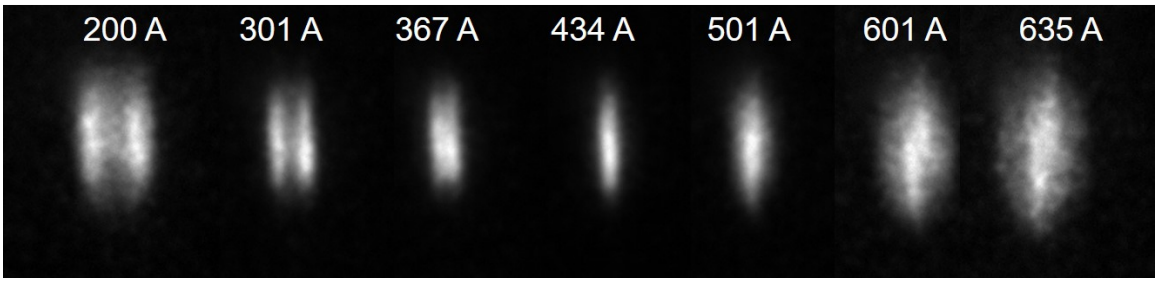

Figure 8.9: Focusing sequence for a vertical slit at $d_i = 45$ cm. While there is a clear focal point at $I = 434$ A, the unfocused beam has a strange, double-peaked structure.

mirror, which permitted us to align the beam on a straight line instead of on a velocity-dependent curve. We replaced the diagonal moving molasses with traditional transverse cooling and a chirped longitudinal sweep. In order to achieve the bullet length we wanted, we adopted the brute-force solution of physically chopping the beam with a steel disk spinning at 10,000 rpm. Having become quite experienced in the art of shattering tiny glass tubes attached to 50 kg steel blocks, we replaced the glass lens tube with a steel-reinforced Vespel frame. By March of 2016, we had installed the adjustable knife edge aperture and were beginning to observe pulsed focusing of a 1 cm bullet. While the shortened bullet and the pulsed lens yielded sharper images, this clarity uncovered an odd phenomenon. As the slit came into focus, we often observed two distinct shapes slowly merging into one. Figure 8.9 shows a typical focusing sequence at $d_i = 45$ cm. This "double peak" effect became the dominant mystery of the experiment.

Despite the double peaks, our slit results were good enough that we began to attempt true imaging. By rotating one knife edge so that it crossed the other at an angle ($\approx 30°$), we converted our vertical slit into the vertex of a triangle. Moving the linear translators in concert shifted the horizontal position of the vertex; moving just the slanted blade changed its vertical position. These degrees of freedom gave us the flexibility we needed to explore true imaging for the first time. We soon produced spots that consistently looked "a little slanted" on one side. Even more encouraging was the fact that the images appeared to be upside-down and backwards, just as we would expect for true imaging. We formed a right triangle by adding a horizontal strip of Kapton tape to our vertex. Figure 8.10 shows a typical focusing sequence for this triangular aperture at $d_i = 85$ cm. Despite prominent double peaks, the triangle shape

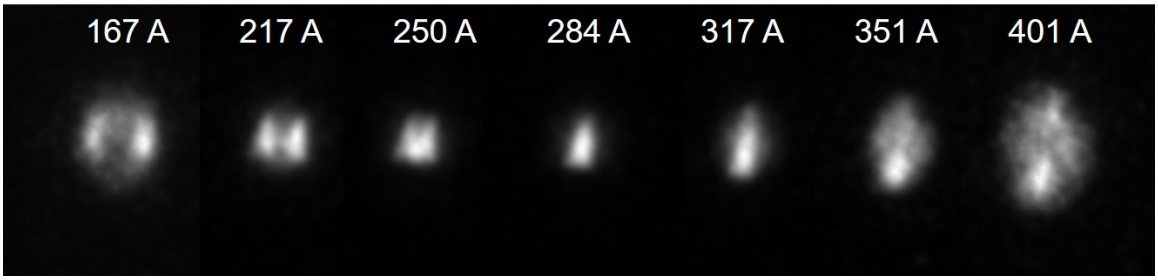

Figure 8.10: The first evidence of true imaging, taken at $d_i = 85$ cm. By rotating one knife edge, we created the vertex of a triangle. A horizontal strip of Kapton tape between the knife edges provided a third side. The imaged triangle is apparent at 284 A. It remains rather blurry, and the double peaks are extremely distinct. With the triangle aperture it is easier to see that the peaks split horizontally for low currents and vertically for high currents. This behavior resembles astigmatism in optical beams.

was recognizable. This aperture also showed what we had not noticed before: double peaks that start out horizontal for low currents reappear later, splitting vertically as the lens current increases beyond the focal point. This behavior bears a striking resemblance to that of an astigmatic optical lens. Double peaks notwithstanding, our success with the triangle aperture was sufficient to justify machining a more complex set of apertures.

Perhaps the most salient scientific revelation from the following period of research was psychological, rather than physical. We discovered that almost any amorphous blob—and we stared at hundreds—can look like the letter F, provided that an F is what the observer expects to see. Eventually, we refined our system enough that real shapes began to emerge. The standard description of these images was "a little bit effy." Figure 8.11 is an example of an image so incontrovertibly "a little bit effy" that it would certainly have led to enthusiastic high fives. Gradually, we cataloged all of the shapes on the slide. We found that the images were generally recognizable, but only to observers who knew what they were expecting to see.

This was the state of the project in June of 2016. We had (recently) achieved true imaging, but our images were only impressive when compared with amorphous blobs. We were ready to throw in the towel and blame the most obvious culprit, chromatic aberration. This is exactly what would have happened, had one mystery not persisted: the double peaks. Pulling this thread unraveled the whole knot, and

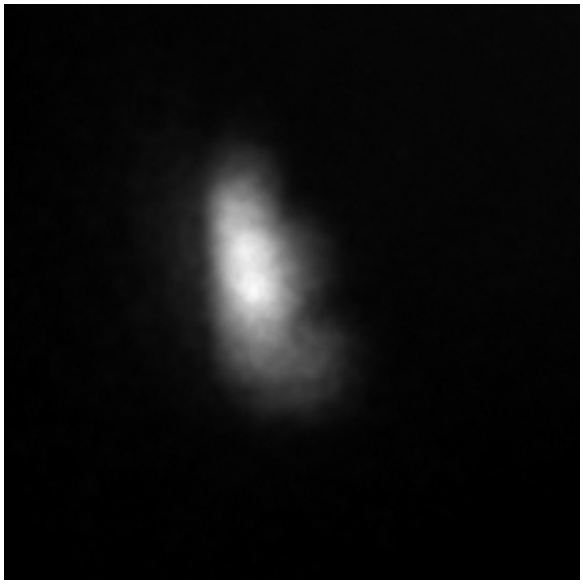

Figure 8.11: An image that is, without a shred of doubt, a little bit effy. The skeptical reader is invited to look at it upside-down, from far away, with one eye closed.

led to more visible progress in 3 months than we had seen in the 3 preceding years.

8.4 Double peaks

In an uncorrected, first generation hexapole lens, double peaks form as the system is brought into focus. Figure 8.12 shows this phenomenon for the aperture shaped like a longhorn (d_i = 113 cm). While the smallest spot occurs at 207 A, this spot appears to be a merged version of two separate images. Furthermore, each of the two secondary images seems to be more in-focus at points other than 207 A. In the hopes that the double peaks are to blame for the relatively low quality of the focused image, we consider potential causes for this odd behavior. Anything causing a horizontal bifurcation in the beam must necessarily break the rotational symmetry of the system. This allows us to rule out the nozzle and the aperture (Note: The aperture breaks axial symmetry in the longhorn example, but only in a trivial way. We still observe the double peaks when the aperture is a pinhole.). Laser cooling and optical pumping clearly do break this symmetry. Unfortunately, blocking these beams still yields double peaks—albeit significantly uglier and fainter specimens. The chopper technically breaks axial symmetry, but it is difficult to see how it would do

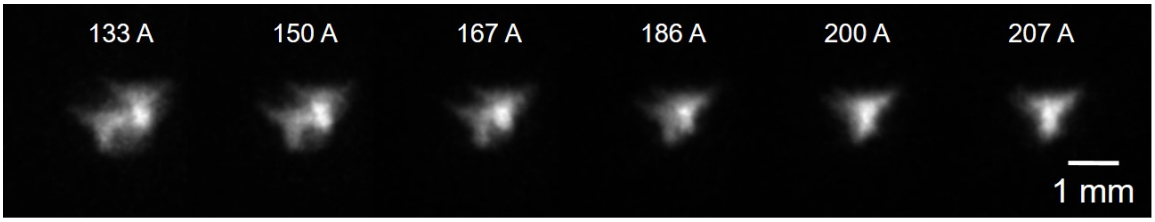

Figure 8.12: A final example of the double peaks, this time for a longhorn at d_i = 113 cm.

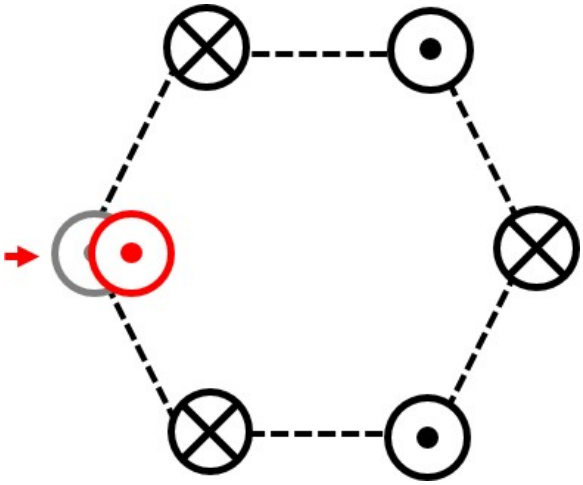

Figure 8.13: A diagram showing one wire out of place. This leads to the double peak phenomenon that undermines our early imaging attempts.

so in a meaningful way. Only two suspects remain: the background field in the lab and the lens itself. As it turns out, the culprit is a combination of two. Fortunately, the solution is the same in both cases. For simplicity, we proceed with this discussion as though the aberration were entirely due to lens defects.

The most obvious way to introduce a defect into our magnetic lens is by misplacing one of the six hexapole wires. Imagine an error of the type illustrated in Figure 8.13, in which a single wire is placed too close to the axis. Figure 8.14 shows a vector plot of the field at the center of such a lens, in which the leftmost wire is placed too close to the axis by 5%, or 100 μm. Compare this to the expected vector field, shown in Figure 6.7 on page 54. From this comparison, it is clear that something serious has gone wrong. In particular, there appear to be two separate lens centers. We confirm this by plotting the magnitude of the field as a function of x and y (Figure 8.15).

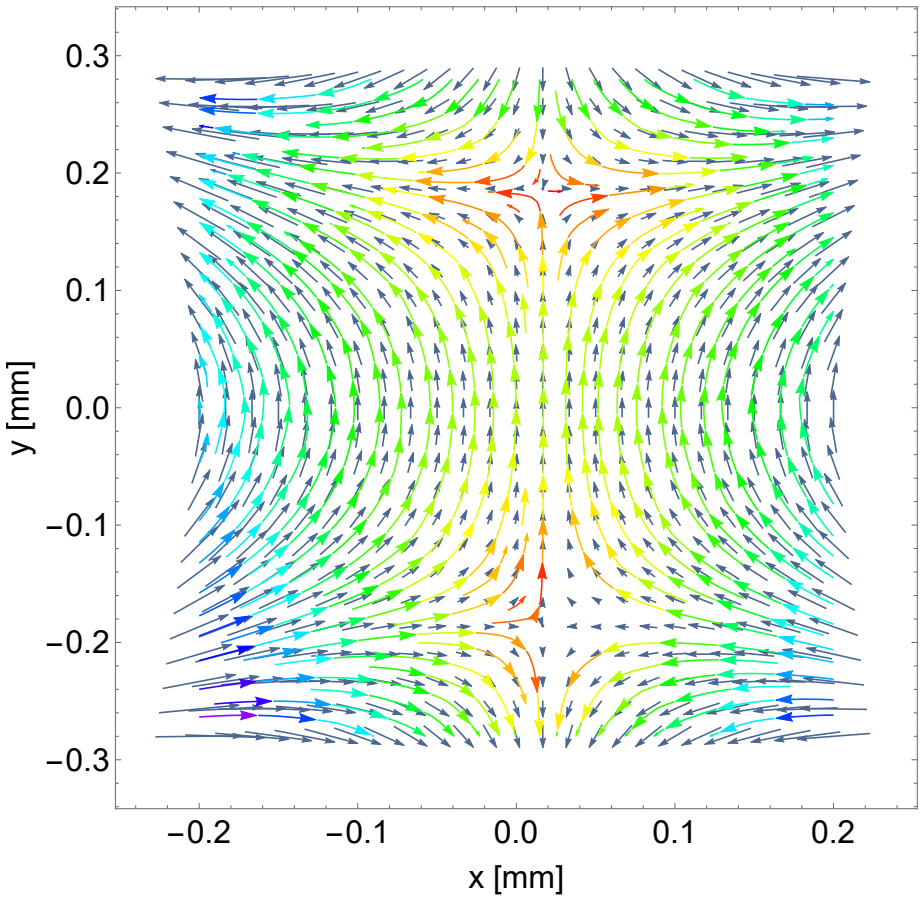

Figure 8.14: A vector plot showing the field produced at the center of a lens (with R = 2 mm) when one wire is too close to the axis by 100 μm. Compare this to the ideal case, shown in Figure 6.7 on page 54. The two local minima independently attract atoms, forming two focal spots.

In the y direction, two local minima have replaced the single minimum we expect. It is fairly easy to imagine how this situation would lead to double peaks. Atoms passing near the middle of the lens are now deflected towards the local minima rather than towards the true center of the lens. In the example given, these minima are around 400 μm apart. Furthermore, the focusing potential in this region is decidedly un-harmonic. This could easily explain the ugly results observed in Figure 8.12.

The only real solution to the problem of an improperly placed wire is simple: re-place the wire; and try not to screw it up this time. In our case, we need to build a more precise frame, probably incorporating micron-scale adjustability into the wire positions. In the meantime, however, we can avail ourselves of a surprisingly effective

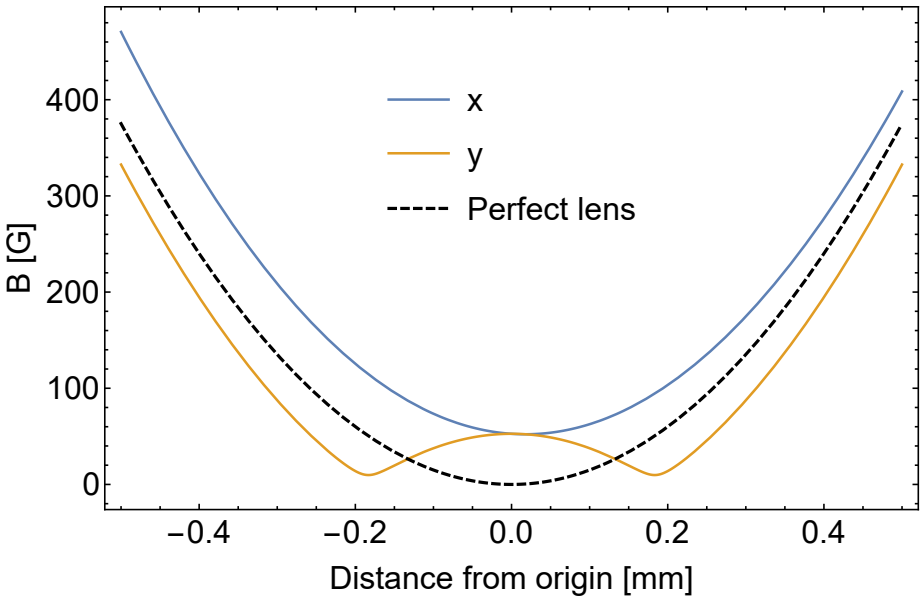

Figure 8.15: Two line-cuts showing the magnitude of the magnetic field corresponding to the vector plot in Figure 8.14.

temporary solution. It turns out that a background magnetic field can create almost exactly the same lens defect as the one represented in Figure 8.14. Fighting fire with fire, we try to correct the defective lens by adding a background field that would—on its own—create exactly the opposite defect. Figure 8.16 shows vector plots of the defective lens field (blue) overlaid with a background field of 50 G in the -y-direction. From the vector plot, it is clear that this will (at least) fix the problem of two local minima along the y-axis. Plotting the field magnitude as before, we discover that the new potential is quite smooth along the x- and y-axes (Figure 8.17). We do not reproduce it here, but a contour plot shows that this smoothness extends throughout the lens.

Returning to the experiment with this new insight, we place two orthogonal sets of Helmholtz coils around the lens. These serve the dual purpose of canceling (in the transverse direction) any existing background field and of using a new background field to correct any defects arising from wire placement. We set the lens current to a position for which the double peaks are apparent, then we adjust the background field until the double peaks go away. Repeating this procedure for several different lens currents both above and below the expected focal point, we obtain the focusing

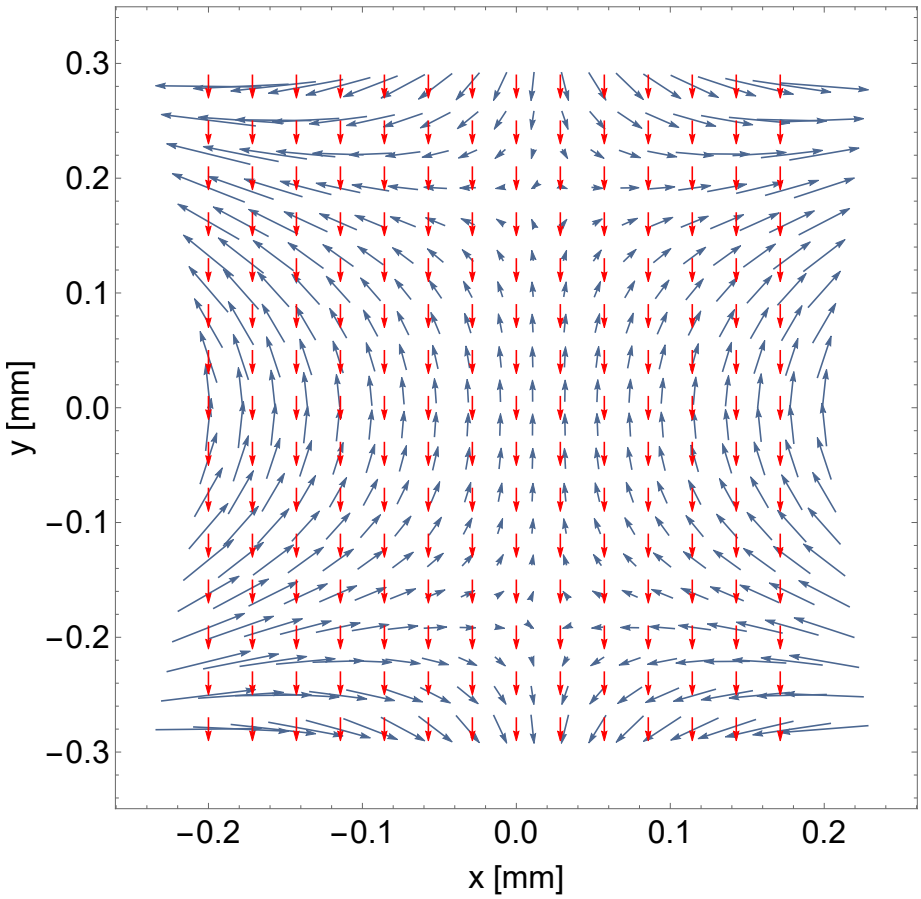

Figure 8.16: Vector plot showing the field from a defective lens (blue) and the background field that we add (red). By comparing these fields, it is easy to see that the correction field eliminates the two local minima along the y-axis, replacing them with a single minimum at the center of the lens.

progression shown in Figure 8.19. Not only are the double peaks gone; the focused image is a reasonably accurate reproduction of the original aperture. In fact, the remaining blur is on the scale of the MCP resolution limit: it would persist even if the lens were perfect. For the 113 cm case, we obtained the best performance by applying a nearly-vertical background field of approximately 7 G.

In order to plan the next steps in this project, we make a few final efforts to understand the source of the double peaks. The main question is whether they are caused by a background field or by lens defects. If it were only the former, one corrective field would work for any focal length. We find instead that we require a different background field at different focal lengths. At 113 cm, 7 G does the trick

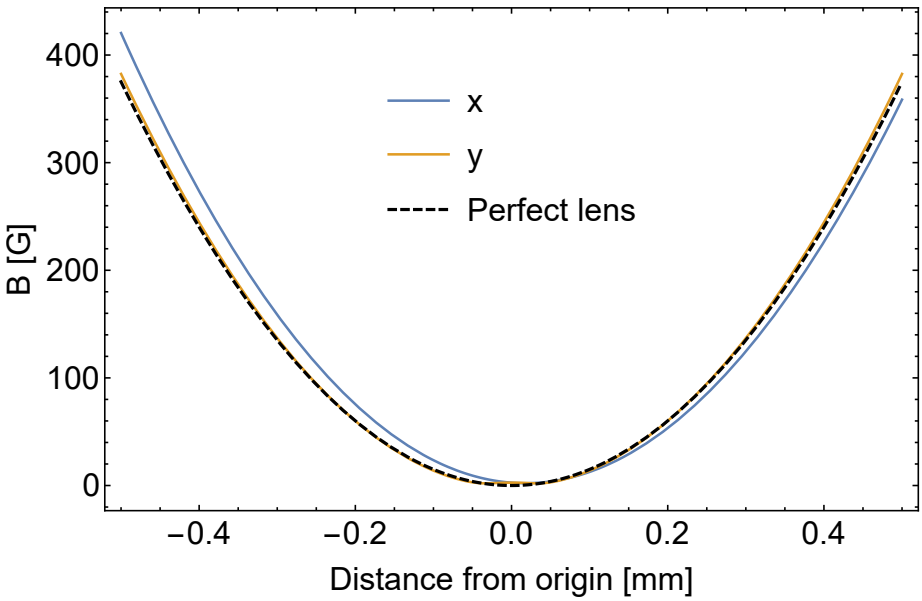

Figure 8.17: Line cuts of the corrected field.

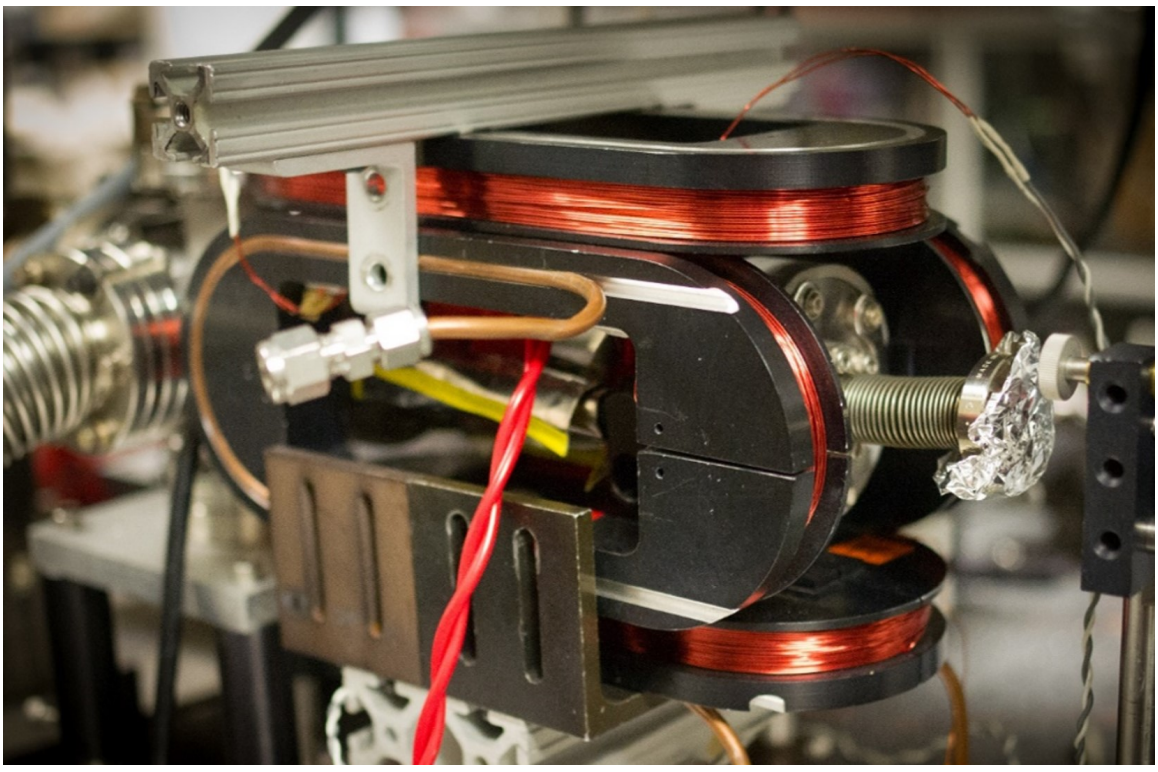

Figure 8.18: A rather inscrutable photograph of our lens surrounded by two sets of elongated Helmholtz coils for double peak correction.

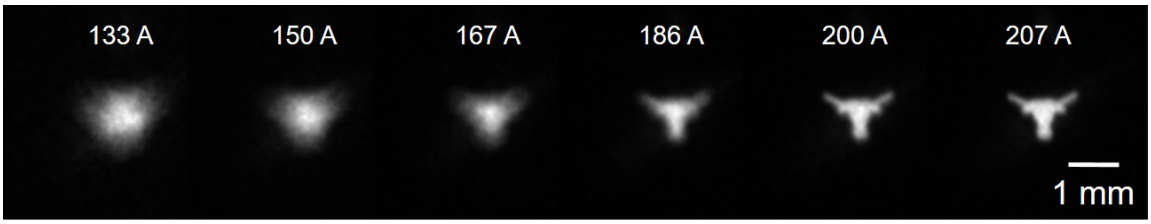

Figure 8.19: Longhorn focusing with the corrective field. The double peaks we saw in Figure 8.12 are mostly gone. The focused image is significantly sharper, with features on the scale of the detector resolution limit.

with a 25 μs pulse. At 87 cm, we need nearly twice that field. At 61 cm, we cannot correct the double peaks very well at all. We are able to remedy this by increasing the pulse time, which allows us to decrease the lens current. For $\tau = 33$ μs, a vertical background field of 18 G corrects the double peaks. From these observations, we conclude that lens defects play a role. If that were the end of the story, however, we would expect a rotation of the lens to yield precisely the same rotation of the double peaks. Instead, we see a nonlinear relationship between these rotation angles. Comparing with calculations, we conclude the the double peaks result at least in part from the interaction of the lens field with the background field in the lab. The next version of this lens, therefore, must incorporate both magnetic shielding and highly precise wire placement.

8.5 Shapes

Figure 8.20: Focusing sequence for the F-shaped aperture with the double peak correction field in place. Unlike in Figure 8.11, we present the image right-side up. Image distance is 113 cm.

Using the double peak correction described above, we begin producing significantly better images than before. The quantitative properties of the corrected lens are discussed in Section 1 of this Chapter. For a qualitative analysis, we look at the other shapes in the slide. Figure 8.20 shows the F coming into focus at 113 cm. Clearly, we can dispense with "effy" and call this image what it is: the letter F. The magnification factor is 0.81, as described quite extensively in Section 1. Figure 8.21 shows similar quality for the Batman logo. To make them as presentable as possible, these images are the results of 30 second integrations with the detection system. It is worth noting, however, that the shapes are directly observable—if a little small—on the phosphor screen with the naked eye.

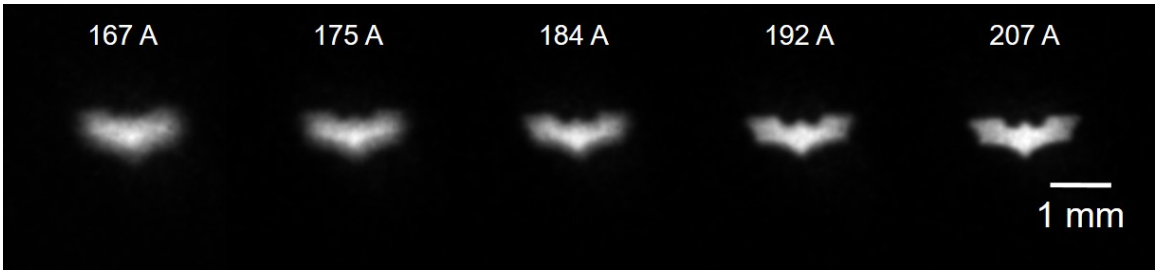

Figure 8.21: Focusing sequence for the bat at 113 cm with the field correction.

The useful beam size at the object plane is around 2 mm wide, which allows us to illuminate approximately one shape in the slide at a time. With the help of the linear translator, we can make a composite image of the entire slide. This is shown in Figure 8.22, along with a reproduction of the original slide photo for reference.

8.6 Simulations

It is encouraging to briefly compare these results with our mathematical simulations. An important difficulty in this comparison is accurately modeling the wire positions, which we have already labeled as uncertain. Making matters worse, the small taper (0.25°) in the Vespel frame means that the wire radius varies by 200 μm over the length of the lens. Moreover, the finite cross-sectional areas of the wires causes the physical case to differ slightly from that in our simple model. Specifically, we expect that the finite extent of the wires slightly reduces the field gradient compared to the infinitesimal case. Despite these uncertainties, we are able to model our system

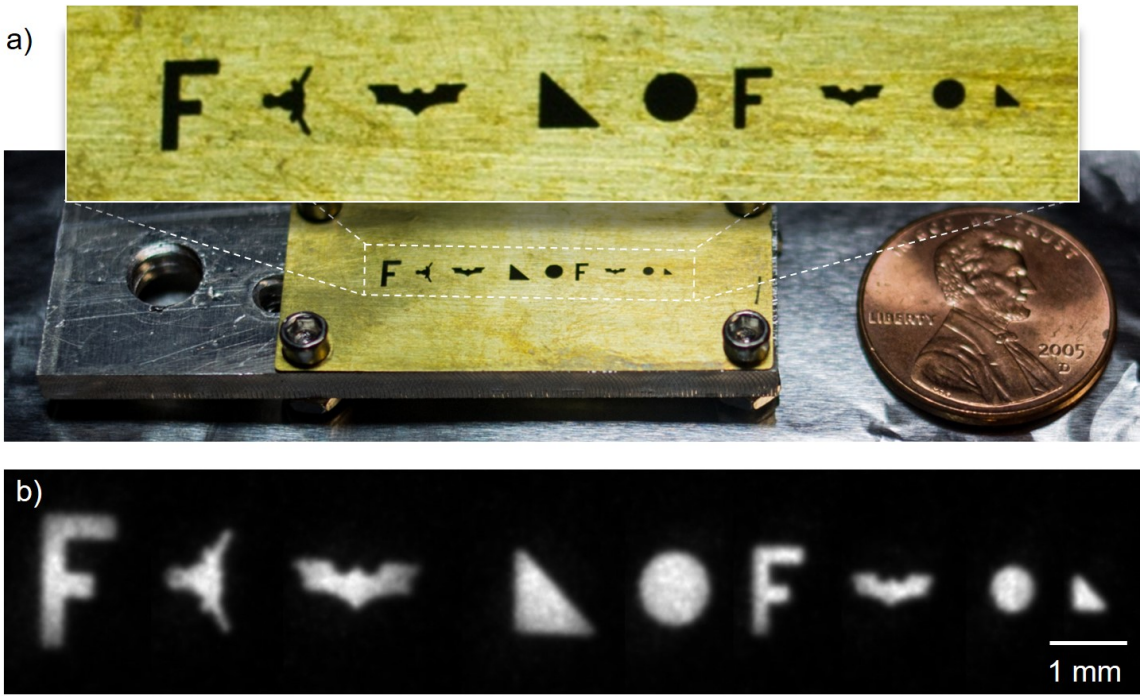

Figure 8.22: (a) Photograph of the slide, for easy reference. (b) Composite image of the slide, again at 113 cm. Though the sizes are matched in this case, the magnification factor is 0.81.

surprisingly well. Using metastable neon at the Doppler limit and a 230 μm aperture at $d_o = 135$ cm, we attempt to reproduce the observed slit focusing results. A hexapole pulsed at 214 A for 33 μs with wires at 2.33 mm results in a focused spot at 62 cm. Increasing the current to 227 A and decreasing the pulse time to 25 μs, we find $d_i =$ 87 cm (Figure 8.23). Finally, a current of 207 A pulsed for 25 μs with a wire radius of 2.4 mm yields a spot at 115 cm. It must be acknowledged that the uncertainty in wire radius provides us with a rather generous fitting parameter, so these simulations are of limited diagnostic value. Nevertheless, the fact that we can reproduce the observed results using entirely plausible numbers suggests that we have captured the important dynamics at work in this system.

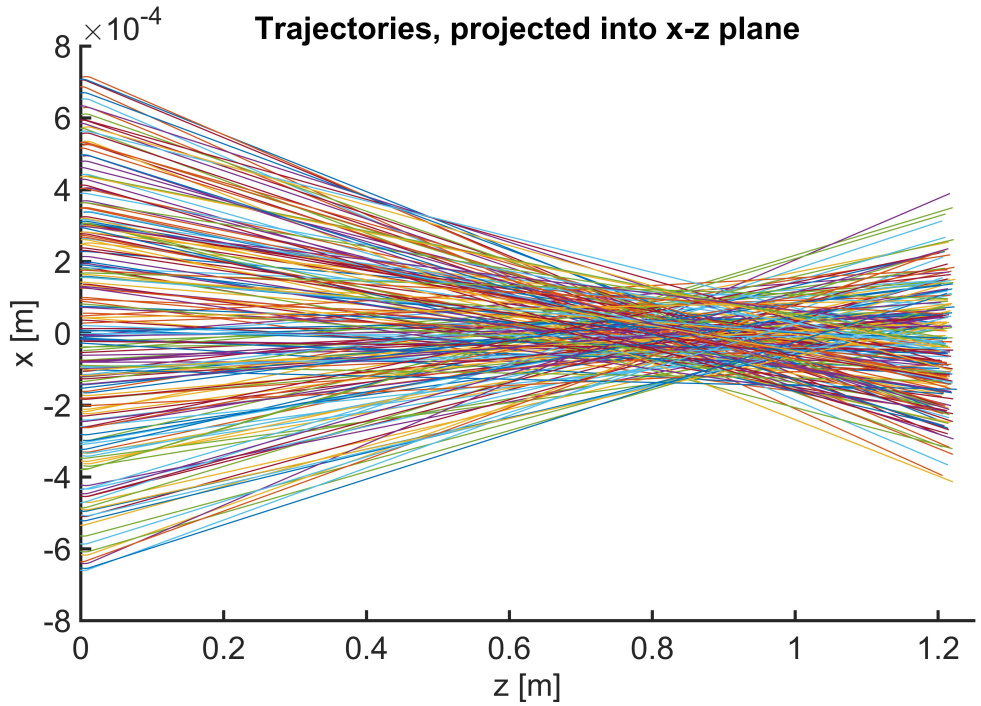

Figure 8.23: Sample trajectories for 200 atoms focusing to a spot at 87 cm. The simulated lens in this case is pulsed at 227 A for 25 μs. The wire radius is 2.33 mm. The resulting spot (assuming a 230 μm object-plane aperture) is on the order of 200 μm.

Chapter Nine: Conclusion

Neutral atom beams feature prominently in applications ranging from fundamental research to industrial manufacturing. A major factor limiting their performance in these roles is beam control. Basic atom-optical elements like mirrors and lenses remain surprisingly unrefined compared to their counterparts in photon-, electron-, and ion-beam management. Neutral atom lenses in particular have remained downright primitive compared to the elaborate aberration-corrected focusing systems devised for other particles. Advances in these tools are long overdue and will lead to a wealth of new opportunities in fundamental atomic physics, nanotechnology, and materials science.

9.1 Summary of work

We have proposed a reinvention of the magnetic hexapole lens that includes chromatic aberration correction and a reduced susceptibility to fringe fields. According to our simulations, this pulsed, tapered, electromagnetic hexapole lens is capable of true imaging well into the nanoscale with magnification factors of 0.01 and lens speeds exceeding f/50.

In order to test the basic operating principle, we have built and tested a prototype lens. We have shown that our technological metrics, such as pulse time and lens current, are easily met using present-day technology. Indeed, most of the electronic equipment we used in this project was already on shelves in the lab. Despite some rather major manufacturing defects, our prototype has outperformed the next-best hexapole lenses by nearly an order of magnitude in resolution. Furthermore, the observed minimum feature size—on the order of 150 μm—is very similar to the detection limit of our MCP. This leaves room for the possibility that our actual resolution is even better than what we have been able to observe. We have performed a range of quantitative tests to characterize the behavior of this lens in the context of ray-optics, and we have found it to be admirably free from distortion and inconsistency.

9.2 Limitations and sources of error

A few problems continue to limit the performance of our prototype. The largest of these is the combination of background fields and wire-radius defects that leads to the double peak phenomenon discussed in Chapter 8. While using the Helmholtz coils to correct this works surprisingly well, we are confident that the only real solution involves building a new lens and implementing large-scale magnetic shielding. Another aspect of this work that could improve is the quality of the optical cooling. We presently observe a brightness increase of 10-100x. In theory, another order of magnitude should be available before we reach the Doppler limit. Finally, the chopper that we use to shorten our beam will need to be replaced with something more graceful. While we do not particularly mind our teeth vibrating when we run the chopper, we suspect that the mechanical disturbance causing this to happen might also impede nanoscale imaging.

Our detection equipment has served us well, but it will not do so for much longer. Though the BOS-18 MCP/Phosphor-screen detector is excellent for analyzing imaged features on the scale of 100 μm - 1 cm, for smaller beams it becomes fairly useless. We have tried on several occasions to implement knife-edge detection, but so far these attempts have produced nonsensical results. Furthermore, fluctuations in average beam intensity over a range of timescales makes the scanned knife edge characterization an uncertain, time-consuming measurement compared to the phosphor screen detection. Both of these problems are perfectly tractable, and the time is approaching to properly address them.

9.3 Future goals

The most pressing directive at this stage in the project is to design and build a second-generation lens. Ideally, this version of the hexapole will incorporate two degrees of freedom for each of the 6 wires. Adjusting the radius of each wire will allow in-situ, empirical correction of the lens defects that we observe in the current prototype. Another useful—though less critical—degree of freedom to add is wire angle, since this would allow us to optimize the taper angle for any focal length. One way to accomplish both of these goals simultaneously would be to use rigid, conductive rods as the hexapole wires, attaching each rod to the surrounding frame

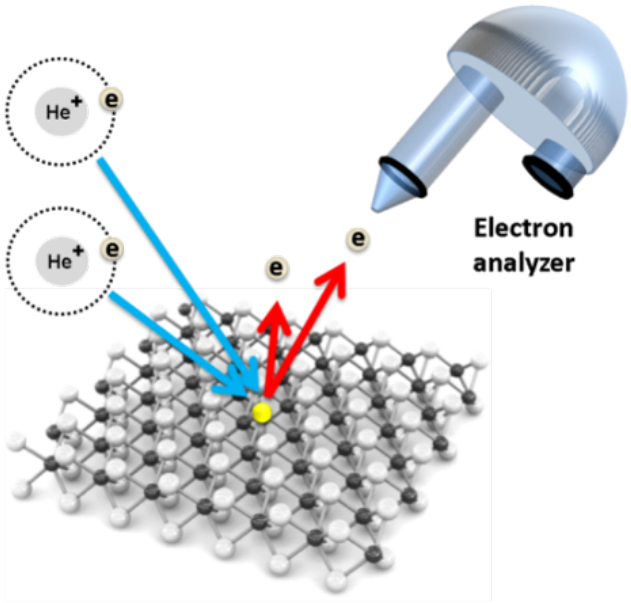

Figure 9.1: A diagram of a metastable atom microscope. Atoms focused by a lens collide with a sample, releasing electrons as they relax to the ground state. The energy spectrum of the electrons released in this manner contains information about the surface states of the sample. Combining our excellent spatial resolution with a high-quality spectrum analyzer would result in a surface microscope of unprecedented sensitivity.

with a high-precision linear translator. Adjusting one translator at a time would vary the wire angle; adjusting both in concert would shift the wire position. Though this apparatus would have more moving parts than the current lens frame, in many ways it would represent a simpler machining task. A related goal in the second-generation hexapole will be minimizing background fields. This means paying more attention to stray fields in the vacuum chamber's support structure, more carefully routing the wire segments connecting consecutive hexapole elements, and possibly surrounding the entire structure with a magnetic shield.

While building the new lens, we will devote a portion of our resources to implementing better beam brightening techniques. While the phase space densities required for 10 nm focusing are not prohibitive by any means, we need to realize better brightness improvements from our various cooling stages. Because another group in the Raizen lab has recently constructed an adiabatic coilgun, we are also

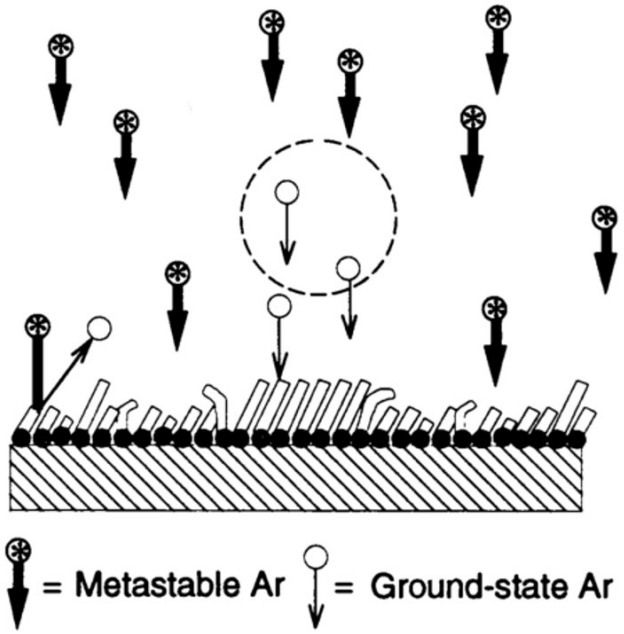

Figure 9.2: Diagram of metastable atoms damaging a "resist" formed by a self-assembled monolayer [42]. Using a transmission mask in conjunction with our lens would allow us to project nanoscale patterns onto a sample treated with this monolayer resist. Chemical etching would then be used, just as in photolithography, to produce high-resolution surface patterns for semiconductor chip manufacturing.

considering using a moving trap to further improve the intensity and temperature of our beam before it reaches the object plane.

Two long-term goals await the second-generation device. In parallel with the focusing project, we are developing the electron spectroscopy tools we will need to build a metastable atom microscope. This is depicted in Figure 9.1, and hinges on the idea that the electrons ejected from metastable relaxation events carry important information about the surface with which the metastable collided. The spectroscopic principles for analyzing these electrons are well established, but so far no one has managed to combine them with a highly focused metastable beam [45, 47]. Once the new lens is up and running, we will merge the lens with the spectroscopy project to create a surface microscope.

A second application for the updated lens will be nanoscale fabrication. Using the true imaging capability of the lens, we will use transmission masks to either directly deposit neutral atoms or to expose self-assembled monolayers for lithography. The latter technique is depicted for Ar^* in Figure 9.2. Both of these approaches have been demonstrated in numerous systems already [71, 42, 72, 21, 12, 73, 27, 23], though not with a lens as effective as ours. These techniques would be competitive with current state-of-the-art photolithography processes, potentially at much lower cost and complexity.

Bibliography

[1] W. Gerlach and O. Stern, "Das magnetische moment des silberatoms," *Zeitschrift für Physik*, vol. 9, no. 1, pp. 353–355, 1922. 1, 2, 36

[2] G. Breit and I. I. Rabi, "On the interpretation of present values of nuclear moments," *Physical Review*, vol. 46, no. 3, pp. 230–231, 1934. 1

[3] Y. Shagam and E. Narevicius, "Sub-Kelvin collision temperatures in merged neutral beams by correlation in phase-space," *Journal of Physical Chemistry C*, vol. 117, no. 43, pp. 22454–22461, 2013. 1, 55

[4] K. Davis, M. Mewes, M. Andrews, N. Druten, D. Durfee, D. Kurn, and W. Ketterle, "Bose-Einstein condensation in a gas of sodium atoms," *Physical Review letters*, vol. 75, no. 22, pp. 3969–3973, 1995. 1

[5] E. Narevicius and M. G. Raizen, "Toward cold chemistry with magnetically decelerated supersonic beams.," *Chemical reviews*, vol. 112, no. 9, pp. 4879–89, 2012. 1, 36

[6] M. Barr, A. Fahy, J. Martens, A. P. Jardine, D. J. Ward, J. Ellis, W. Allison, and P. C. Dastoor, "Unlocking new contrast in a scanning helium microscope," *Nature Communications*, vol. 7, p. 10189, 2016. 1

[7] M. Koch, S. Rehbein, G. Schmahl, T. Reisinger, G. Bracco, W. E. Ernst, and B. Holst, "Imaging with neutral atoms: a new matter-wave microscope," *Journal of microscopy*, vol. 229, no. 1, pp. 1–5, 2008. 1

[8] R. Castillo-Garza, J. Gardner, S. Zisman, and M. G. Raizen, "Nanoscale imaging of neutral atoms with a pulsed magnetic lens," *ACS Nano*, vol. 7, no. 5, pp. 4378–4383, 2013. 1

[9] D. Meschede and H. Metcalf, "Atomic nanofabrication: atomic deposition and lithography by laser and magnetic forces," *Journal of Physics D: Applied Physics*, vol. 36, no. 3, pp. R17–R38, 2003. 1, 7, 36

[10] R. Chaustowski, V. Leung, and K. Baldwin, "Magnetic hexapole lens focusing of a metastable helium atomic beam for UV-free lithography," *Applied Physics B*, vol. 86, no. 3, pp. 491–496, 2006. 1, 7, 36

[11] G. Timp, R. Behringer, D. Tennant, J. Cunningham, M. Prentiss, and K. Berggren, "Using light as a lens for submicron, neutral-atom lithography," *Physical Review Letters*, vol. 69, no. 11, pp. 1636–1639, 1992. 1, 5, 7, 36

[12] M. Baker, A. J. Palmer, W. R. MacGillivray, and R. T. Sang, "Lithographic pattern formation via metastable state rare gas atomic beams," *Nanotechnology*, vol. 15, no. 9, pp. 1356–1362, 2004. 1, 125

[13] F. Lison, H.-J. Adams, D. Haubrich, M. Kreis, S. Nowak, and D. Meschede, "Nanoscale atomic lithography with a cesium atomic beam," *Applied Physics B*, vol. 65, no. 3, pp. 419–421, 1997. 1, 5

[14] A. A. Tseng, "Recent developments in nanofabrication using ion projection lithography.," *Small*, vol. 1, no. 6, pp. 594–608, 2005. 1

[15] L. Bonolis, "Research profile: Otto Stern," *Webpage: www.mediatheque.lindau-nobel.org / research-profile / laureate-stern*, Accessed: October, 2016. 2, 30

[16] L. Dunoyer, "Sur la réalisation d'un rayonnement matériel d'origine purement thermique. Cinétique expérimentale," *Radium*, vol. 8, no. 4, pp. 142–146, 1911. 1, 11

[17] F. Knauer and O. Stern, " Uber die reflexion von molekularstrahlen," *Zeitschrift für Physik*, vol. 53, no. 11, pp. 779–791, 1929. 2

[18] I. Estermann and O. Stern, "Beugung von molekularstrahlen," *Zeitschrift für Physik*, vol. 61, no. 1, pp. 95–125, 1930. 2

[19] H. Friedburg and W. Paul, "Reflexion eines atomstrahles am rande eines magnetfeldes," *Naturwissenschaften*, vol. 37, no. 1, p. 20, 1950. 2

[20] H. Friedburg, "Optische abbildung mit neutralen atomen," *Zeitschrift für Physik*, vol. 130, no. 4, pp. 493–512, 1951. 2, 6

[21] V. I. Balykin and P. N. Melentiev, "Nanolithography with atom optics," *Nanotechnologies in Russia*, vol. 4, no. 7-8, pp. 425–447, 2009. 3, 97, 125

[22] V. I. Balykin, P. A. Borisov, V. S. Letokhov, P. N. Melentiev, S. N. Rudnev, A. P. Cherkun, A. P. Akimenko, P. Y. Apel, and V. A. Skuratov, "Atom pinhole camera with nanometer resolution," *JETP Letters*, vol. 84, no. 8, pp. 466–469, 2006. 3, 4

[23] P. N. Melentiev, a. V. Zablotskiy, D. a. Lapshin, E. P. Sheshin, a. S. Baturin, and V. I. Balykin, "Nanolithography based on an atom pinhole camera," *Nanotechnology*, vol. 20, no. 23, p. 235301, 2009. 3, 4, 97, 125

[24] O. Carnal and J. Mlynek, "Youngs double-slit experiment with atoms: a simple atom interferometer," *Physical Review Letters*, vol. 66, no. 21, pp. 2689–2692, 1991. 4

[25] T. Reisinger, S. Eder, M. M. Greve, H. I. Smith, and B. Holst, "Free-standing silicon-nitride zoneplates for neutral-helium microscopy," *Microelectronic Engineering*, vol. 87, no. 5-8, pp. 1011–1014, 2010. 4, 5

[26] S. D. Eder, T. Reisinger, M. M. Greve, G. Bracco, and B. Holst, "Focusing of a neutral helium beam below one micron," *New Journal of Physics*, vol. 14, 2012. 4

[27] W. R. Anderson, C. C. Bradley, J. J. McClelland, and R. J. Celotta, "Minimizing feature width in atom optically fabricated chromium nanostructures," *Physical Review A*, vol. 59, no. 3, pp. 2476–2485, 1999. 5, 6, 125

[28] T. Sleator, T. Pfau, V. Balykin, and J. Mlynek, "Imaging and focusing of an atomic beam with a large period standing light wave," *Applied Physics B Photophysics and Laser Chemistry*, vol. 54, no. 5, pp. 375–379, 1992. 5, 6

[29] V. I. Balykin and V. S. Letokhov, "The possibility of deep laser focusing of an atomic beam into the Å-region," *Optics Communications*, vol. 64, no. 2, pp. 151–156, 1987. 5, 6

[30] J. J. McClelland and M. R. Scheinfein, "Laser focusing of atoms: a particle-optics approach," *Journal of the Optical Society of America B*, vol. 8, no. 9, p. 1974, 1991. 6

[31] W. G. Kaenders, F. Lison, A. Richter, R. Wynands, and D. Meschede, "Imaging with an atomic beam," 1995. 7, 25

[32] M. Mützel, M. Müller, D. Haubrich, U. Rasbach, D. Meschede, C. O'Dwyer, G. Gay, B. V. De Lesegno, J. Weiner, K. Ludolph, G. Georgiev, and E. Oesterschulze, "The atom pencil: serial writing in the sub-micrometre domain," *Applied Physics B: Lasers and Optics*, vol. 80, no. 8, pp. 941–944, 2005. 6

[33] W. Kaenders, F. Lison, I. Müller, a. Richter, R. Wynands, and D. Meschede, "Refractive components for magnetic atom optics.," *Physical review. A*, vol. 54, no. 6, pp. 5067–5075, 1996. 6, 36

[34] H. R. Noh and F. Shimizu, "Imaging of an atomic beam with electrostatic lenses," *Physical Review A*, vol. 61, no. 4, p. 41601, 2000. 6

[35] H. Pauly, *Atom, Molecule, and Cluster Beams I - Basic Theory, Production and Detection of Thermal Energy Beams*. Springer, 2000. 11, 12, 16

[36] M. Kratzenstein, "Untersuchungen über die wolke bei molekularstrahlversuchen," *Zeitschrift für Physik*, vol. 93, no. 5, pp. 279–291, 1935. 12

[37] A. Kantrowitz and J. Grey, "A high intensity source for the molecular beam. Part I. Theoretical," *Review of Scientific Instruments*, vol. 22, no. 5, p. 328, 1951. 12

[38] H. J. Metcalf and P. van der Straten, "Laser cooling and trapping of neutral atoms," in *The Optics Encyclopedia*, Wiley-VCH Verlag GmbH & Co. KGaA, 2007. 17, 64

[39] H. J. Metcalf and P. van der Straten, *Laser Cooling and Trapping*. Graduate Texts in Contemporary Physics, Springer New York, 2001. 17, 19, 20, 64, 80

[40] W. Ketterle and D. E. Pritchard, "Atom cooling by time-dependent potentials," *Physical Review A*, vol. 46, no. 7, pp. 4051–4054, 1992. 18

[41] H. Metcalf, "Entropy exchange in laser cooling," *Physical Review A*, vol. 77, no. 6, p. 61401, 2008. 27

[42] K. K. Berggren, A. Bard, J. L. Wilbur, J. D. Gillaspy, a. G. Helg, J. J. McClelland, S. L. Rolston, W. D. Phillips, M. Prentiss, and G. M. Whitesides, "Microlithography by using neutral metastable atoms and self-assembled monolayers.," *Science*, vol. 269, no. 5228, pp. 1255–1257, 1995. 36, 124, 125

[43] R. Gupta, J. J. McClelland, Z. J. Jabbour, and R. J. Celotta, "Nanofabrication of a two-dimensional array using laser-focused atomic deposition," *Applied Physics Letters*, vol. 67, no. 10, p. 1378, 1995. 36

[44] H. L. Bethlem and G. Meijer, "Production and application of translationally cold molecules," *International Reviews in Physical Chemistry*, vol. 22, no. 1, pp. 73–128, 2003. 36

[45] Y. Harada, S. Masuda, and H. Ozaki, "Electron spectroscopy using metastable atoms as probes for solid surfaces.," *Chemical reviews*, vol. 97, no. 6, pp. 1897–1952, 1997. 36, 124

[46] F. Shimizu, "Specular reflection of very slow metastable neon atoms from a solid surface," *Physical Review Letters*, vol. 86, no. 6, pp. 987–990, 2001. 36

[47] H. Morgner, "The quantitative characterization of liquid and solid surfaces with metastable helium atoms," *AIP Conference Proceedings*, vol. 500, no. 2000, pp. 687–698, 2000. 36, 124

[48] T. J. McCarthy, M. T. Timko, and D. R. Herschbach, "Manipulation of slow molecular beams by static external fields," *The Journal of chemical physics*, vol. 125, no. 13, p. 133501, 2006. 36

[49] T. M. Roach, H. Abele, M. G. Boshier, H. L. Grossman, K. P. Zetie, and E. A. Hinds, "Realization of a magnetic mirror for cold atoms," *Physical Review Letters*, vol. 75, no. 4, pp. 629–632, 1995. 36

[50] J. T. Cremer, D. L. Williams, M. J. Fuller, C. K. Gary, M. a. Piestrup, R. H. Pantell, J. Feinstein, R. G. Flocchini, M. Boussoufi, H. P. Egbert, M. D. Kloh, and R. B. Walker, "Periodic magnetic field as a polarized and focusing thermal neutron spectrometer and monochromator," *Review of Scientific Instruments*, vol. 81, no. 1, p. 013902, 2010. 36, 42

[51] A. I. Sidorov, R. J. McLean, W. J. Rowlands, D. C. Lau, J. E. Murphy, M. Walkiewicz, G. I. Opat, and P. Hannaford, "Specular reflection of cold caesium atoms from a magnetostatic mirror," *Quantum and Semiclassical Optics: Journal of the European Optical Society Part B*, vol. 8, no. 3, pp. 713–725, 1996. 36

[52] K. S. Johnson, "Localization of metastable atom beams with optical standing waves: nanolithography at the Heisenberg limit," *Science*, vol. 280, no. 5369, pp. 1583–1586, 1998. 36

[53] D. Lau, A. I. Sidorov, G. Opat, R. McLean, W. Rowlands, and P. Hannaford, "Reflection of cold atoms from an array of current-carrying wires," *The European Physical Journal D - Atomic, Molecular and Optical Physics*, vol. 5, no. 2, pp. 193–199, 1999. 36

[54] M. Metsälä, J. J. Gilijamse, S. Hoekstra, S. Y. T. van de Meerakker, and G. Meijer, "Reflection of OH molecules from magnetic mirrors," *New Journal of Physics*, vol. 10, no. 5, p. 053018, 2008. 36

[55] E. Narevicius, A. Libson, C. G. Parthey, I. Chavez, J. Narevicius, U. Even, and M. G. Raizen, "Stopping supersonic beams with a series of pulsed electromagnetic coils: an atomic coilgun," *Physical Review Letters*, vol. 100, no. 9, p. 093003, 2008. 36, 69

[56] S. K. Kim, W. Lee, and D. R. Herschbach, "Cluster beam chemistry: hydration of nucleic acid bases; ionization potentials of hydrated adenine and thymine," *The Journal of Physical Chemistry*, vol. 100, no. 19, pp. 7933–7937, 1996. 36

[57] T. S. Zwier, "The spectroscopy of solvation in hydrogen-bonded aromatic clusters," *Annual Review of Physical Chemistry*, vol. 47, no. 1, pp. 205–241, 1996. 36

[58] R. E. Smalley, L. Wharton, and D. H. Levy, "Molecular optical spectroscopy with supersonic beams and jets," *Accounts of Chemical Research*, vol. 10, no. 4, pp. 139–145, 1977. 36

[59] K. Halbach, "Design of permanent multipole magnets with oriented rare earth cobalt material," *Nuclear Instruments and Methods*, vol. 169, no. 1, pp. 1–10, 1980. 36

[60] E. Narevicius, A. Libson, M. F. Riedel, C. G. Parthey, I. Chavez, U. Even, and M. G. Raizen, "Coherent slowing of a supersonic beam with an atomic paddle," *Physical Review Letters*, vol. 98, no. 10, pp. 1–4, 2007. 37

[61] D. Peach, "An examination of the effects of optical aberrations, obstruction and seeing on real planetary images," *Webpage: www.damianpeach.com / simulation.htm*, Accessed: October, 2016. 49

[62] M. G. Raizen, D. Budker, S. M. Rochester, J. Narevicius, and E. Narevicius, "Magneto-optical cooling of atoms," *Opt. Lett.*, vol. 39, no. 15, pp. 4502–4505, 2014. 66

[63] J. Sacher and T. Triumph, *How to Swear Around the World*. Chronicle Books LLC, 2012. 67

[64] U. Even, "The Even-Lavie valve as a source for high intensity supersonic beam," *EPJ Techniques and Instrumentation*, vol. 2, no. 1, p. 17, 2015. 68

[65] M. Hillenkamp, S. Keinan, and U. Even, "Condensation limited cooling in supersonic expansions," *Journal of Chemical Physics*, vol. 118, no. 19, pp. 8699–8705, 2003. 68

[66] U. Even and N. Lavie, "Even-Lavie valve," *Webpage: sites.google.com / site / evenlavievalve*, Accessed: October, 2016. 69

[67] E. D. Black, "An introduction to Pound-Drever-Hall laser frequency stabilization," *American Journal of Physics*, vol. 69, no. 1, p. 79, 2001. 74

[68] G. C. Bjorklund, M. D. Levenson, W. Lenth, and C. Ortiz, "Frequency modulation spectroscopy," *Applied Physics B*, vol. 32, no. 3, pp. 145–152, 1983. 74

[69] C. E. Wieman and L. Hollberg, "Using diode lasers for atomic physics," *Review of Scientific Instruments*, vol. 62, no. 1, pp. 1–20, 1991. 74

[70] E. A. Donley, T. P. Heavner, F. Levi, M. O. Tataw, and S. R. Jefferts, "Double-pass acousto-optic modulator system," *Review of Scientific Instruments*, vol. 76, no. 6, pp. 3–8, 2005. 77

[71] A. Bard, "Self-assembled monolayers exposed by metastable argon and metastable helium for neutral atom lithography and atomic beam imaging," *Journal of Vacuum Science & Technology B: Microelectronics and Nanometer Structures*, vol. 15, no. 5, p. 1805, 1997. 125

[72] W. Lu, K. G. H. Baldwin, M. D. Hoogerland, S. J. Buckman, T. J. Senden, T. E. Sheridan, and R. W. Boswell, "Sharp edged silicon structures generated using atom lithography with metastable helium atoms," pp. 3846–3849, 1998. 125

[73] J. J. McClelland, R. E. Scholten, E. C. Palm, and R. J. Celotta, "Laser-focused atomic deposition.," *Science*, vol. 262, no. 5135, pp. 877–80, 1993. 125